Formability Studies of Austenitic Stainless Steel 316 at Elevated Temperatures

THESIS

submitted in partial fulfillment
of the requirements for the degree of

DOCTOR OF PHILOSOPHY

by

SYED MUJAHED HUSSAINI
ID. No – 2009PHXF451H

under the supervision of
Prof. Amit Kumar Gupta

BIRLA INSTITUTE OF TECHNOLOGY AND SCIENCE, PILANI,
HYDERABAD CAMPUS
2014

BIRLA INSTITUTE OF TECHNOLOGY AND SCIENCE, PILANI
HYDERABAD CAMPUS

CERTIFICATE

This is to certify that the thesis entitled "**Formability Studies of Austenitic Stainless Steel 316 at Elevated Temperatures**" and submitted by **Syed Mujahed Hussaini** ID.No **2009PHXF451H** for award of Ph.D. of the Institute embodies original work done by him under my supervision.

Signature of the Supervisor

Name in capital letters: **Dr. AMIT KUMAR GUPTA**

Designation: **Associate Professor**
Mechanical Engineering Department
BITS-Pilani, Hyderabad Campus

Date:

ACKNOWLEDGEMENTS

It gives me great pleasure to record my deep sense of gratitude to **Dr. Amit Kumar Gupta**, Associate Professor, Department of Mechanical Engineering, BITS-Pilani, Hyderabad Campus for his unceasing guidance, cooperation, encouragement and keen interest during my research work. I am indeed fortunate to work under his supervision.

This thesis is the outcome of the kind co-operation, good-will, and technical and moral support extended by **Dr. Swadesh Kumar Singh**, Professor in Mechanical Engineering Department, GRIET, Hyderabad. My grateful thanks go beyond the pages of this thesis.

I thank my DAC members, **Prof. S.P. Regalla** and **Prof. M. Srinivas**, for their profuse continual support. I am grateful to them for their suggestions in bringing this thesis into final form.

I am highly indebted to the **DAE, Govt. of India** for their project grant 2009/36/45-BRNS/1751, which helped in procuring the test facilities and raw material to conduct this research.

I also take this opportunity to thank **Prof. B.N. Jain**, Vice – Chancellor, BITS-Pilani and **Prof. V.S. Rao**, Director, BITS-Pilani, Hyderabad Campus for providing a research environment to enhance my research interest and commitment. I am also privileged to work with the faculty and staff of BITS-Pilani, Hyderabad Campus.

I wish to enlist my deep sense of gratitude to **Prof. Y. V. D. Rao**, Head, Mechanical Engineering Department, BITS-Pilani, Hyderabad Campus for providing me full support to carry out this research work. I am extremely grateful to the all the faculty and staff of Mechanical Engineering Department. I owe special thanks to Workshop staff for providing me the unstinted cooperation and help whenever required.

In addition, I heartily thank **Dr. Bhaskar Majumdar**, Scientist-F, DMRL, for helping me in doing the fracture study. I am grateful to **Mr. Nitin Kotkunde** for creating a friendly research team and giving valuable suggestions at times, **Mr. Jayahari** for his help in experimentations and **Mr. K Sajun Prasad** for his support in numerical simulations. I also thank to **Mr. R. Pillai** and **Mr. Raghunandan** for patiently helping me in proof reading my thesis.

To a conscientious scholar, research is a challenging and stupendous task. I would not have been able to achieve my goal without benign attitude and care of my parents. My special thanks are due to my family members and friends for continuously encouraging me over these years.

(Syed Mujahed Hussaini)

ABSTRACT

Sheet metal forming involves forming of flat thin sheet metal blanks into desired shape and size, under the applied forces by punch and die assembly. Sheet metal forming processes are widely used for producing a large number of simple to complex shape components in automotive, aerospace, nuclear, and defense applications. In recent times, there has been a growing demand for sheet metal forming of high strength materials like stainless steels, titanium alloys, etc., which have a poor drawability at room temperature due to having high mean flow stress values. One of the ways to overcome this limitation is warm forming, in which the material is usually formed at an elevated temperature, (0.3 – 0.5) times of melting temperature. Warm forming helps in decreasing the load requirement for plastic deformation, in attaining uniform thickness distribution in the drawn component and in increasing the material formability significantly.

The focus of this research work is to study the forming behavior of Austenitic Stainless Steel (ASS) 316 at elevated temperatures through deep drawing experimentation. First, the material has been characterized using tensile tests at elevated temperatures and different mechanical properties such as Young's modulus, yield stress, strain hardening exponent, etc. have been evaluated. In addition, with the help of observations about serrations in true stress vs. true strain curves and the presence of negative strain rate sensitivity, the presence of Dynamic Strain Aging (DSA) phenomenon has been identified. In ASS 316, the DSA phenomenon occurred in a temperature range of 400°C – 600°C and at a strain rate of less than 10^{-2} s^{-1}.

In order to understand the formability behavior of ASS 316 at elevated temperatures, deep drawing experiments have been conducted on a hydraulic press test setup from room temperature to 400°C. The drawability has been measured in terms of the Limiting Draw Ratio (LDR) and the thickness distribution of the drawn cups. It has been found that the LDR increases with increase in temperature up to 300ºC, but it decreases with further increase in temperature to 400°C due to the DSA effect. Within the experimental limitations, it has been considered that warm forming of ASS 316 at 300ºC gives the highest LDR (2.47) with a uniform thickness distribution in the drawn cups. In order to support these findings, Finite Element (FE) simulation model of deep drawing process has been developed in LS – Dyna. Actual conditions have been simulated and the FE simulation results have been found to be in good agreement with the experimental findings.

Further, Forming Limit Diagram (FLD) has been developed for ASS 316 at 300˚C theoretically as well as experimentally. Theoretical FLD has been developed using MK theory with Hill's and Barlat's yield criteria and the experimental FLD has been constructed by performing hemispherical dome punch tests. Theoretical FLD with Barlat's yield criterion has been found to be in good agreement with the experimental FLD. The results of this formability study on ASS 316 at elevated temperatures can be used for process design and development to meet production demands.

CONTENTS

LIST OF TABLES

LIST OF FIGURES

LIST OF ABREVIATIONS

ANN	Artificial Neural Network
ASS	Austenitic Stainless Steel
ASTM	American Society for Testing and Materials
BHP	Blank Holding Pressure
DR	Drawing Ratio
DSA	Dynamic Strain Aging
FEM	Finite Element Methods
FLC	Forming Limit Curve
FLD	Forming Limit Diagram
LDR	Limiting Drawing Ratio
MSE	Mean Square Error
MTS	Mechanical Threshold Stress
PID	Proportional Integral Derivative
PLC	Portevin LeChatelier
SEM	Scanning Electron Microscope
SRS	Strain Rate Sensitivity
UTM	Universal Testing machine

LIST OF SYMBOLS

b	Burgers vector
C_v	Vacancy concentration
D	Diffusion coefficient
D_0	Diffusion frequency factor
E	Elastic modulus
K	Strength coefficient
k_b	Boltzmann's constant
L	Instantaneous length
L_o	Initial length
m	Strain rate sensitivity index
n	Strain hardening exponent
Q_m	Activation energy
R	Lankford coefficient
T	Temperature in °K
t	Time
$\bar{v}$	Average velocity
ε	Strain
$\acute{\varepsilon}$	Strain rate
ε_p	Plastic strain
σ	Stress
ρ	Density
μ	Shear modulus

CHAPTER 1:

Introduction

Metal forming is a process of making metal parts and objects through mechanical deformation. In this, the material is deformed to the required shape without adding or removing of material and its mass remains unchanged. The objective of this research is to determine the effectiveness of warm forming for increasing the formability of high strength alloys, in particular Austenitic Stainless Steel (ASS) 316. Warm forming is generally used to deform a sheet metal into required shapes at an elevated temperature, which is less than one half of the material's melting temperature [1-3].

1.1 Sheet Metal Forming

Sheet metal forming is a process of plastically deforming the sheet metal blanks into three-dimensional shapes by the application of forces without much change in sheet thickness. There is no significant change in surface area to volume ratio. It involves the conversion of flat, thin sheet metal blanks into parts of desired shape. The process is carried out on the plane of the sheet by tensile forces with high ratio of surface area to thickness. In this the residual stresses in the material will cause the sheet to spring back slightly [4]. Friction between the tool and metal interfaces and temperature of the blank are the important factors, which control the forming [5]. Sheet metal forming processes like deep drawing, stretching, bending etc. are widely used to produce a large number of simple to complex components in automotive, aircraft, household, and nuclear

applications. Some of these components are shown in Figure 1.1. These parts are manufactured using one or more of the sheet metal forming processes.

(a) (b)

(c) (d)

Figure 1.1: Parts made by sheet metal forming (a) aircraft nozzle (b) domestic gas cylinder, (c) nuclear cladding tube, (d) wheel rim

1.2 Deep Drawing

Deep drawing is one of the most important sheet metal forming processes. In this, thin sheets are formed into desired shapes by forcing punch into a die cavity. The process is considered "deep" drawing when the depth of the drawn part exceeds its diameter. In this, as the punch moves downward, the sheet metal blank is radially drawn into the forming die by the mechanical action of the punch. The working principle of deep drawing is shown in Figure 1.2. The tendency of the flange to fold upward is restricted by the blank holder. It is loaded by a holding force, which prevents wrinkling and controls the material flow into the die cavity [6]. While being drawn out of the blank holder and die interface, material gets subjected to compressive and tensile forces. The flange region experiences a radial tensile stress and a compressive hoop stress due to the material retention property. These compressive hoop stresses result in flange wrinkles. In this majority of the deformation occurs in the flange of the cup. Figure 1.3 shows the different types of stresses developed in the material in deep drawing operation [7].

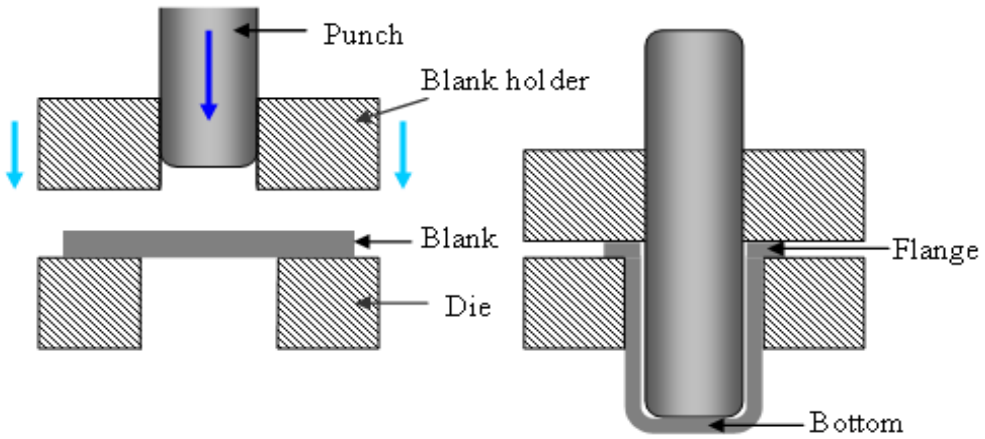

Figure 1.2: Deep drawing of cylindrical cups

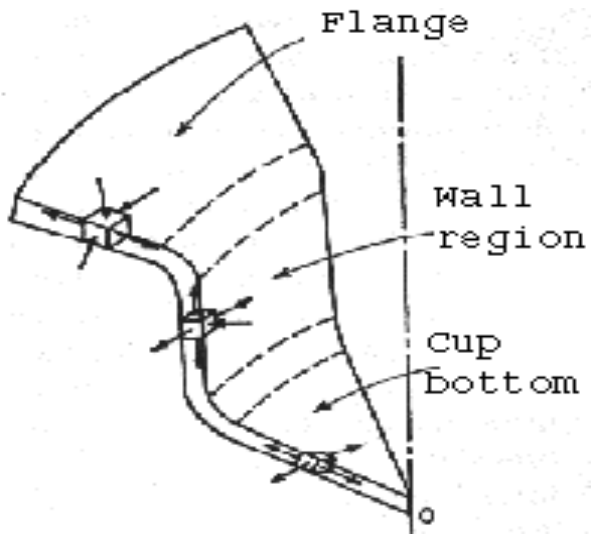

Figure 1.3: Stresses and deformation in the deep drawing cup sections

The developed stresses influence the thickness variation in the drawn cup. The primary deformation occurs in the flange by radial tension and circumferential compression, which leads to the thickness increase in the flange portion. The second deformation zone is in the cup wall by uniaxial stretching (plane strain), which causes thinning of the metal in the wall. There is also bending of the sheet around the die and punch corner, which makes the sheet further thin. Third deformation zone is in the cup bottom, which is subjected to biaxial tension. Due to these stress distributions, thickness of the drawn cup is not same in various zones in the cup. The thickness at bottom is more uniform due to the uniform strain in bi-axial directions.

The total drawing force consists of the ideal forming load, an additional component to compensate for friction in the contacting areas of the flange region, and bending forces in ironing as shown in Figure 1.4 [7]. The forming load is transferred from the punch to the

drawn part wall into the deformation region. In the drawn part, which is in contact with the punch, the hoop strain is zero, whereby the plane strain condition is reached. In reality, mostly the plane strain condition is achieved only approximately. Due to tensile forces acting on the part wall, thinning is prominent which results in an uneven part wall thickness. It can be observed that the part wall thickness is lowest at the point where the part wall loses contact with the punch, i.e., at the punch radius. The thinnest part thickness determines the maximum stress that can be transferred to the deformation zone. If the total drawing force exceeds a limit, failure occurs at punch corner region. As the blank size increases, there is an increase in the total force and if the total force exceeds beyond a certain value, fracture occurs in the cup wall. This puts a limit on the blank size drawn into the cup.

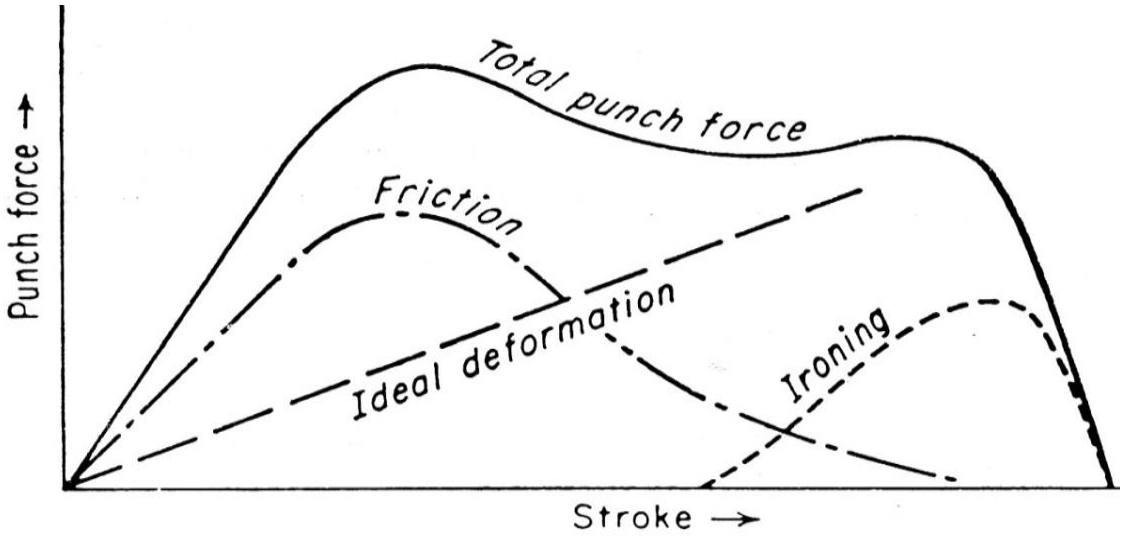

Figure 1.4: Punch force vs. punch stroke diagram for deep drawing [7]

Due to material volume constancy, the flange thickens changes and results in blank holder contact at the outer boundary rather than on the entire surface. The maximum forces that can be safely transferred from the punch to the blank sets a limit on the maximum blank size. The Drawing Ratio (DR) in a deep drawing process is calculated as the ratio of blank diameter to the cup diameter. The maximum draw ratio that can be obtained under perfect deep drawing conditions without fracture in a single stroke is called Limiting Drawing Ratio (LDR). The LDR is considered a good measure of drawability of a material. For achieving a very high draw ratio, redrawing and annealing between draws is preferred.

Deep drawing is affected by many factors like material properties, tool selection, lubrication etc. Because of these factors some defects may occur during the process. The common defects which occur during deep drawing are wrinkling, earring, and fracture. Wrinkles are the rough surface on the walls of the cup, which is caused by compressive hoop stresses. The phenomenon of unequal heights in the walls of the totally drawn part is known as earring. The main reason for earring is planar anisotropy. Practically it is impossible to eliminate earring in deep drawing because metal blanks are mostly anisotropic. Fracture is tensile instability caused by strain localization [8].

1.3 Formability in Deep Drawing

Formability is defined as the ability of a sheet material to be formed into a specific shape without fracture or excessive thinning. A

general parameter that indicates the formability and ductility of the material is the fracture strain which is determined by a uniaxial tensile test. The strain identified by this test is defined by elongation with respect to a reference length. It is important to note that deformation is homogeneous up to uniform elongation and subsequently strain localizes at fracture. Fracture strain is nevertheless a rough indicator of the formability of the material [9].

Formability of sheet metal plays an important role in the success of the sheet metal operations. This can be more specifically discussed in terms of drawability in deep drawing. When a sheet material is plastically deformed, the deformation in the surface is much more pronounced than the thickness, which is measured in terms of the Lankford coefficient (R). Lankford coefficient is defined as the ratio between width strain to thickness strain in the uniaxial tensile test. Materials with very good drawability have R more than unity.

Drawability is a measure of the ability of a material to be drawn in, as in forming a cup from a flat metal blank. During deep drawing, the metal blank undergoes different strains in different directions. Drawability is assessed by the strain distribution during deformation and it is predicted in terms of Forming Limit Diagram (FLD), which presents the different deformation paths of the material. The diagram shows the correlation between the first principal strain ε_1, which is major in the plane of the sheet metal, and second principal strain ε_2,

which is minor in the plane of the sheet metal. It provides a graphical description of sheet material failure by mapping a Forming Limit Curve (FLC). FLC represents a limiting curve in FLD, up to which the material can be formed without fracture in the specimen [10, 11].

Figure 1.5 shows a typical FLD as defined by Keeler and Goodwin [12]. Here, upper curve is FLC and the lower curve is a safety curve (SC). Any point, which falls above FLC, indicates failure and, which falls below SC, shows safe while drawing of the blank. In between the two is warning to fracture, but still safe. Anything concentrated in the extreme left shows the forming limits becoming very large. FLD is widely used for presenting complete information on formability. Materials which have the ability to distribute strains more uniformly are below the FLC and expected to have higher formability [12, 13].

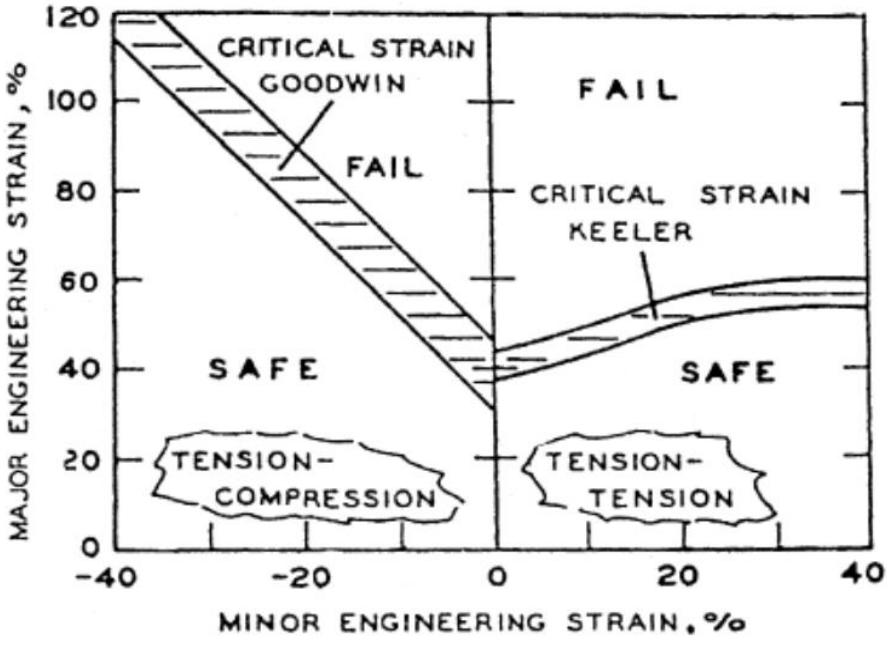

Figure 1.5: Forming limit diagrams as defined by Keeler and Goodwin [12]

Higher friction between the die and the sheet increases the punch force required for drawing and puts a limit on the LDR. Very high limiting draw ratio cannot be obtained due to excessive thinning and fracture in the cup wall associated with large draw ratios. For most of the high strength sheet materials, LDR of more than 2.2 is extremely difficult to achieve in conventional deep drawing [14].

Enhancement of formability leads to higher maximum possible deformation that can be given in a single step and hence parts of larger depth or complex geometry can be formed. It reduces the number of production steps and thus increases productivity. Beyond a certain extent, enhancement in formability is not possible because of the inherent limitations of conventional sheet metal forming processes. Therefore, there have been many attempts to improve formability and product quality in general, by improvement in the properties of sheet metal or by optimization of tool design and process conditions [15, 16]. Warm deep drawing is one of the important technique researchers have explored in recent past for increasing formability of sheet metals.

1.4 Warm Deep Drawing

In warm deep drawing, sheet metal is heated to elevated temperatures, but below the recrystallization temperature. At elevated temperatures, materials can be formed into complex shapes without much difficulty. Although applications of deep drawing processes at

elevated temperatures have not yet been used effectively, but it is going to be a very important manufacturing application in future. Drawing at elevated temperatures results in the decrease of the flow stress. It relieves residual stresses and increases the formability of the materials, hence deformations become easier. It allows a deeper drawing and more stretching to form into the final products. There have been many attempts to improve LDR and product quality by varying temperature of the work blank [17]. A close control of temperature is needed to achieve uniform thickness along the cup wall with higher LDR. Deformation of high strength materials like stainless steels needs higher forces. These materials can be processed easily by warm forming.

1.5 Austenitic Stainless Steel 316

Stainless Steels are those ferrous alloys that contain a minimum of 12% chromium for corrosion resistance. It has vast industrial applications due to its high corrosion resistance, high temperature strength and other mechanical characteristics even at elevated temperatures. Special grades of stainless steels have been developed to have greater corrosion resistance at a broad range of different temperatures. Several important sub-categories of stainless steels have been developed such as austenitic, martensitic, ferritic, duplex, etc.

Austenitic grades are most common iron-chromium-nickel steels, and widely known as the 300 series. The austenitic stainless

steels, because of their high chromium and nickel content, are the most corrosion resistant steel in the stainless steel group, which can even withstand boiling sea water [18]. The austenitic structure is very tough and ductile even at lower temperatures and also does not lose its strength at elevated temperatures. Because of its properties, particularly ASS 316 is used in nuclear industry for both structural and radiation containment [19].

It is well known that at a sufficiently high temperature in alloys and solid solutions, aging processes occur due to the interaction of solute atoms with dislocations or, in other words, pinning of dislocations by solute atoms and in this way, increasing the necessary stress for the dislocation movement. As a consequence of aging, an increase in the strength and hardness of the material are usually observed. The processes of aging occur at higher temperatures, because the diffusion of the elements responsible for aging is aided by raising the temperature.

When the aging process occurs in alloys containing solute atoms, which can rapidly and strongly segregate to dislocations and get locked dynamically during straining, the phenomenon is commonly referred as Dynamic Strain Aging (DSA). The maximum effect of DSA corresponds to such conditions, where the solute atoms can follow by diffusion and change the dislocation structure. Most obvious manifestation of DSA is serrated yielding. In solid solutions, diffusion of solute atoms to mobile dislocations are temporarily

arrested at obstacles, as a consequence, the solute concentration experiences change locally by the dislocations. This depends on the time of arrest and the solute diffusion coefficient. Serrated flow or in other words, instabilities in plastic strain are caused by an instantaneous increase in plastic strain [20, 21]. At elevated temperatures, ASS 316 undergoes the phenomenon of DSA, which increases its strength.

1.6 Scope of the Study

ASS 316 has good formability in deep drawing, but it needs higher forces and high capacity presses to deform the metal sheet into the required shape. Under warm conditions, the forces can be reduced and low capacity presses can be used for deformation. The scope of this research study is mainly focused on the formability of ASS 316 at elevated temperatures in deep drawing setup. It also concerns about the effect of DSA on the formability of ASS 316 in deep drawing, particularly on LDR and thickness distribution of the drawn cups. This study also involves finite element simulation model development and analysis of deep drawing operations in ASS 316 at elevated temperatures using LS-Dyna. Further, FLDs are theoretically constructed using Marciniak Kuczynski analysis and experimentally validated using Nakazima test.

1.7 Research Methodology

In this study, tensile tests are conducted at different temperatures from room temperature to 700ºC in the interval of 50ºC at constant strain rates. Mechanical properties of the material have been determined from the test data. DSA phenomenon has been investigated by construction of true stress vs. true strain graphs and the DSA range of temperatures and strain rates have been identified. Nature of fracture of the tensile specimens has been investigated at different temperatures, below the DSA region and in the DSA region to know the material behavior.

The Lankford coefficient of the material is measured in three directions 0º, 45º, and 90 º to the rolling direction of the sheet. Based on this, normal anisotropy and planar anisotropy of the metallic sheet have been calculated

The most common indexes of formability for deep drawing are the LDR and the thickness of the cup. Formability of the sheets is investigated by measuring the LDR and thickness distribution of the drawn cups at various temperatures. Deep drawing process has been modeled in LS-Dyna as per the experimental conditions. The actual conditions of the material were simulated and the response of the model under forming load was analyzed. The parameters of the cups were measured, which are drawn at the temperatures of DSA and non-DSA regions. Deep drawing experimental setup has been developed and the deep drawing experiments have been conducted to validate the results of finite element analysis.

Theoretical FLC for ASS 316 at 300˚C is predicted by Marciniak Kuczynski analysis by using Hill's and Barlat's yield criteria. Experimental FLC has been constructed with different width specimens as per the ASTM E2218 standards test procedure. Theoretical FLC has been validated with the experimental FLC.

1.8 Organization of the Thesis

This research thesis is organized in seven chapters as follows:

Chapter – 1: This chapter gives the introduction about deep drawing process, formability, the importance of ASS and its industrial applications. Significance of warm deep drawing has been highlighted and the DSA phenomenon in the material is described in brief.

Chapter – 2: This chapter covers the survey of literature on the materials behavior under warm farming at different temperatures. Also, a review of the literature on DSA and its influence on properties of the materials has been presented. The research gaps in the literature have been highlighted and the objectives of this research have been specified.

Chapter 3: This chapter emphasizes the characterization of ASS 316 by tensile tests at different temperatures and different strain rates as per ASTM standards. Different properties have been evaluated from the test data and the temperature range for DSA phenomena has been identified. Fracture study on the tensile test specimens has been carried out in order to study the material behavior at elevated temperatures. In addition, the anisotropic characteristics of the material have been evaluated.

Chapter 4: This chapter elaborates on the deep drawing experimentation using hydraulic press test setup. It focuses on the measurements of LDR and the thickness distribution of the drawn cups at different temperatures in order to understand the formability behavior of ASS 316 at elevated temperatures. The effects of process parameters such as blank holding pressure and punch speed, on the formability of sheet have also been studied.

Chapter 5: This chapter focuses on FE analysis of deep drawing process at elevated temperatures. Finite element model is developed in LS –Dyna for preliminary investigations of formability. Actual conditions are simulated and the responses of the model during deep drawing at different temperatures have been analyzed. FE simulation results have been validated with the help of experimental findings.

Chapter 6: This chapter mainly focuses on the development of FLD of ASS 316 at 300˚C. Theoretical FLD has been developed using MK theory with Hill's and Barlat's yield criteria. Experimental FLD has been constructed by performing hemispherical dome tests as per ASTM standards on different width specimens. Theoretical FLD with Barlat's yield criterion has been found to be in good agreement with the experimental FLD.

Chapter 7: This chapter summarizes the key findings of this thesis and presents the conclusions and the scope of future work.

CHAPTER 2:

Literature Review

In this chapter, a review of literature has been done for enhancing the formability in warm conditions. The warm forming of material at different conditions, the occurrence of DSA in the material and its effects on the formability of stainless steel have been studied. Various researchers' work on the occurrence of DSA in austenitic stainless steels has been reviewed. Gaps in the existing research have been described and the research objectives have been identified.

2.1 Warm Forming

Warm forming is a promising processing route that has been considered to improve the formability of metals and alloys [22]. The aim of warm sheet metal forming processes is to improve plastic flow of material, as well as to decrease the spring back effect. Cold forming ($T < 0.3\ T_m$) takes advantage of strain hardening to increase the strength of a material at the penalty of higher forming forces, while hot forming ($T > 0.5\ T_m$) lowers the yield stress and allows simultaneous recrystallization, which controls the grain size refinement and mechanical behavior of material [23]. To avoid high temperatures and forces, warm forming ($0.3\ T_m < T < 0.5\ T_m$) is used as the intermediate process, which allows recovery but not recrystallization. The aim of warm forming is to capitalize on the advantages of both hot and cold forming. The forming temperature affects the behavior of the material during deformation, properties and accuracy of finished parts [24].

In comparison to hot forming processes, warm forming requires higher forces because of the greater material flow stress, thus making increased demand on the forming tools and equipment. From the other perspective, greater part accuracy in terms of dimensions, shape and surface finish can be achieved. The optimal temperature for a particular warm forming operation and formed material always results in a compromise. Its lower limit is determined by force which can be produced by the forming setup and by the formability of the material [25]. The upper limit is usually determined by the amount of oxidation which can be tolerated.

The plastic deformation of metals takes place by one of the wo processes, slip and twinning, out of which slip is the most common. Slip occurs due to the movement of dislocations and thus the mobility of the dislocations plays a key role in the ease of deformation. As the dislocations move through the lattice, an applied stress is required to overcome the lattice friction. Thermal energy aids the dislocations to overcome these stresses. In BCC metals, Peierls-Nabarro stresses are the main obstacle and the temperature has week effect, but in FCC metals, like aluminum and ASS, the temperature has strong effect [26]. At room temperature deformation takes place by slip on the basal planes and by twinning on other planes, but at elevated temperature slip occurs in the most of the planes and twinning becomes less important. At elevated temperatures, plastic deformation occurs much easier.

Warm forming has been studied in the 1970s and 1980s by Shehata et al. [27] and Wilson et al. [28]. They showed that warm forming improves the formability of Aluminium alloys because the strain hardening of these alloys decreases at elevated temperatures. Schmoeckel et al. [29] studied the drawability of ferrous materials at the elevated temperatures. Li and Gosh [30] have shown that warm forming can considerably improve the formability of aluminum alloy sheet. More recently, van den Boogaard et al. [31] and McKinley et al. [32] studied non-isothermal cylindrical cup deep drawing at different gradients of temperature and observed that the formability of Al–Mg alloy sheet can be improved by increasing the temperature in selected regions of the sheet.

In warm forming, the challenge for process design is to investigate the complex interaction between mechanical and thermal effects on formability. Tyng Bin Huanga et al. [33] studied non-isothermal deep drawing of magnesium alloys experimentally and validated it by FE analysis. The study showed that the forming temperature, lubricant and sheet thickness have significant effect on the limiting drawing ratio and found the optimum process parameters. Kim et al. [34] performed coupled thermo-mechanical FE analysis for forming of aluminum rectangular cups at elevated temperatures. They selected thickness variation as a failure criterion and they obtained part depth values at various die-punch temperature combinations and blank holder pressures. The results suggested that higher forming temperature results in higher limiting strain. Also, an increasing

temperature gradient between the die and punch led to increased formability of the material.

Abedrabbo et al. [35] worked on the warm forming of two automotive aluminum alloys, AA5182-O and AA5754-O and developed a temperature-dependent anisotropic material model for finite element analysis and its formability simulation. They successfully implemented this model in the fully coupled thermo-mechanical FE analysis of the warm forming of aluminum products. FE analysis with the developed thermo-mechanical constitutive model accurately predicted both the deformation behavior and the failure location in the blank and compared favorably to the experimental results for both materials. They showed the importance of using both thermal analysis and an accurate anisotropic temperature- dependent material model in a fully coupled mode in order to model the warm forming process accurately.

Metal sheets show anisotropic behavior in the plastic regime and temperature dependency on the strain rate sensitivity at elevated temperatures. The change of anisotropy during the forming process is assumed to be negligible. With this assumption, the concepts of anisotropic yield functions and isotropic hardening are used. This approach has some limitations, Tugcu et al. [36] have shown that the aspects of the plane-stress assumption, which do not come into consideration in isotropic analyses, can play an important role on the

accuracy of the results and axes enters the computation directly due to the presence of material anisotropy.

Many studies have considered the characterization of the anisotropic behavior of sheet metal. Paquet et al. [37] have proposed a method for developing microstructure based elasto-viscoplastic models for cast aluminum alloys. Desmorat and Marull [38] introduced a non-quadratic plasticity criterion based on Kelvin decomposition of the elasticity tensor [39] for anisotropic materials. Segurado et al. [40] have implemented an anisotropic model in an implicit finite element analysis. Fourmeau et al. [41] studied the effect of plastic anisotropy on the mechanical behavior of a rolled aluminum plate under quasi-static loading conditions. They found that the anisotropic yield function provides an adequate description of the significant anisotropic behavior of a high-strength aluminum alloy [42]. Yoon et al. showed that earing is the combination of the contributions from *R*-value and yield stress directionalities [43]. They presented a new analytical approach that predicts the earing profile and verified the results for three different aluminum alloys. Recently, warm forming simulation of elasto-plastic hardening materials with anisotropy has been studied, using temperature and strain rate dependent hardening rules.

In summary, the researchers have concentrated on warm forming of mainly those anisotropic sheet materials which have the low melting temperature such as Al, Mg, etc. Not much research has

been done to study warm forming of high strength and high melting temperature materials like ASS, Titanium alloys, etc.

2.2 DSA Behavior

At elevated temperatures, alloys like steels exhibit DSA phenomena. These phenomena are characterized by the serrations in true stress vs. true strain curve and also by negative strain rate sensitivity in plastic deformation zone [44]. Serrated yielding was first observed by LeChatelier in 1909 while studying the properties of mild steel at elevated temperatures. Portevin and LeChatelier investigated the same behavior in an aluminum alloy (3.5% Cu - 0.5% Mg - 0.5% Mn). Serrated flow was subsequently referred to as the Portevin LeChatelier effect. The temperature range within which the serrated yielding occurs is known as the DSA or PLC region. Lower than this temperature range, the diffusivity is too low for the solute atoms to segregate to the dislocations and lock them during deformation. Above this range, the diffusivity of the solute atoms is fast enough to keep up with the moving dislocations without causing a drag force or impeding the motion. Both are said to move in phase under the influence of their interaction energy. Physical manifestations of DSA is identified by serrated plastic flow, negative strain rate sensitivity and the variation of ultimate tensile strength, strain hardening with temperature. Strain localization and increased strain hardening rate are observed during inhomogeneous plastic flow, which affect the

mechanical performance of the materials in terms of ductility and time to fracture at constant strain deformation.

The strain rate increase leads to the increase in dislocation velocity and the decrease in time that the dislocation spends to arrest at obstacles. The diffusivity of the solute atoms must therefore be greater in order to catch up with the fast moving dislocations and to sustain DSA. The diffusion coefficient increases exponentially with temperature and thus an increase in temperature results in an increase in diffusivity of the solute atoms. The effect of strain rate on the location of the DSA region is clearly illustrated in low carbon steel [45]. At lower temperatures, the solute atoms are immobile with respect to the moving dislocations and do not impede their motion. On the other extreme, at high temperatures, the mobility of the solute atoms is such that they can follow the dislocations without any drag or disruption. At intermediate temperatures the solute atoms interact with the moving dislocations and affect the flow properties. This region is known as the DSA region.

The plastic flow becomes unstable in the DSA temperature range. In general, two types of instabilities are associated with strain aging: Luders front and the PLC effect. The Luders front, in a tensile specimen, is delineation between plastically deformed and un-deformed material. It appears at one end of the specimen and propagates with typical constant velocity towards the other end, if the cross head velocity of the test machine is kept constant [45]. The

nominal stress-strain curve appears smooth during the propagation. However, the localization is preceded by yield point behavior. After reaching a peak, the flow stress quickly drops to a lower value. The PLC effect, on the other hand, is seen either as a sequence of shear bands appearing sequentially with sometimes regular spacing, or as a set of propagating bands with a source at one end of the specimen. The resulting nominal stress-strain curve is serrated, i.e., the stress and plastic strain oscillate. During the oscillations, the average stress may remain constant or increase, either steadily or in steps corresponding to the crossing of the specimen length by the bands, indicating a continuous strain hardening.

2.3 Physical Parameters of DSA

Cottrell and Bilby [47] proposed that strain aging effects are due to the segregation of interstitial solutes to form atmospheres around dislocations, which require an increased force to break away from these atmospheres to become mobile. There is, however, no clear consensus on the details of the mechanism of DSA, although the Cottrell model became the basis for much of the study of strain aging. Three different approaches have been used in modeling DSA: the "solute dragging model", "arrest model" and "pair reorientation model" (also known as “Snoek locking” or “Schoeck Seeger locking” mechanism).

In Cottrell's solute dragging model, an impurity atmosphere is formed during dislocation movement. Cottrell postulated that this mechanism can operate even at temperatures that are too low for bulk solute diffusion. The diffusion can be assisted by excess of vacancies generated during plastic deformation and the average velocity of dislocations decreases with plastic straining due to increase of dislocation density [48]. According to Cottrell model, unstable plastic flow will initiate when

$$\dot{\varepsilon} = \frac{4bD_0\rho_m C_v}{l} exp(-\frac{Q_m}{k_B T}) \quad (2.1)$$

where $\dot{\varepsilon}$ is the strain rate, C_v is the vacancy concentration, D_0 is the diffusion frequency factor, l is the effective radius of the solute atoms atmosphere, b is a Burgers vector, ρ_m is the density of mobile dislocations, Q_m is the effective activation energy for solute migration, T is temperature in $°K$ and K_B is the Boltzmann's constant. Increase in vacancy concentration and in dislocation density with strain can be expressed by following relation:

$$C_v = K\varepsilon^m \; and \;\; \rho_m = N\varepsilon^\beta \quad (2.2)$$

where K, m, N and β are materials constants

Then critical strain (ε_c) to initiate DSA can be expressed, by rearranging the equation as:

$$\varepsilon_c^{m+\beta} = \frac{l\dot{\varepsilon}exp(Q_m/K_B T)}{4bKNDo} \quad (2.3)$$

Although this theory is able to qualitatively predict the temperature and strain rate dependence of the onset of serrated yielding, it has been shown that the critical strain (ε_c) for the start of serrated yielding as calculated from this theory is in error by several orders of magnitude. Moreover, the solute drag model does not predict the effect of solute concentration on ε_c or on DSA in general [49].

In the arrest model developed by McCormick, it is considered that the motion of a dislocation on its slip plane is a discontinuous process. The dislocation faces obstacles in its motion, which have to be surmounted, possibly with the help of thermal activation. A dislocation segment has to wait for a certain average time t_w until the obstacle is overcome, and after surpassing the obstacles it jumps at a high velocity to the next obstacles. Diffusion of solute atoms to the dislocations may occur during the waiting time. As a consequence of DSA, the relation between stress, strain and strain rate are affected. At constant strain rate, the needed stress to keep the dislocations moving will increase. As the waiting time is directly related to strain rate, the dependence of stress on strain rate will also influence the DSA. This treatment is based on the idea that the moving dislocations are not pinned depending on solute concentration in dislocation core which depends on the waiting time and the solute diffusion coefficient. This concept is developed to give the dependence of stress on strain rate, strain, and temperature in the presence of DSA and to formulate a criterion for the start of the Portevin LeChatelier effect. The time at which the dislocation moves from obstacle to obstacle is assumed

negligibly short in comparison to the waiting time of the dislocation in front of an obstacle. Thus, the average velocity of dislocation motion may be expressed as

$$\bar{v} = \frac{L}{t_w} \quad (2.4)$$

where L is the average distance between arresting obstacles and t_w is the waiting time. The strain rate at which the material can deform due to dislocation motion is proportional to the average velocity of mobile dislocations multiplied by dislocation density. In DSA the solid solutions are described as diffusion of solute atoms to mobile dislocations, temporarily arrested at obstacles. The time to lock a dislocation by diffusion of solute atoms to dislocation core, for elastic solute dislocation interactions and for short aging times, was estimated by Friedel [50] as:

$$t_a = \left(\frac{C_1}{\alpha C_0}\right)^{3/2} \frac{K_B T b^2}{3 D U_m} \quad (2.5)$$

where t_a is aging time, C_1 is the solute concentration at the dislocation core which is required to lock it, C_0 is the solute concentration of the alloy, α is constant, D is the solute diffusion coefficient, U_m is the binding energy of solute atom to dislocation. At the critical strain when DSA is occurred it is assumed that $t_w \approx t_a$. Combination of equations

$$\dot{\varepsilon} = \left(\frac{\alpha C_0}{C_1}\right) \frac{3 L \rho U_m C_v D_0 exp\left(\frac{Q_m}{K_B T}\right)}{K_B T b} \quad (2.6)$$

This can be expressed using terms of the critical strain as

$$\varepsilon_c^{\dot{m}+\beta} = \left(\frac{C_1}{\alpha C_0}\right)^{3/2}\left(\frac{\dot{\varepsilon} KTb exp\left(\frac{Q_m}{K_B T}\right)}{3LNKU_m D_0}\right) \quad (2.7)$$

As a consequence the solute concentration experienced locally by the dislocations depends on the arrest time and the solute diffusion coefficient. Based on the ideas suggested by Penning [51] the dependence of flow stress on the strain rate, the onset of serrated yielding, temperature dependence of the flow stress, effect of DSA on work hardening and strain rate sensitivity were analyzed in detail by van den Beukel [52]. The theory of flow localization due to dynamic strain aging was developed further and validated with the experimental results obtained on FeC and AuCu alloys by McCormick [53]. In the pair reorientation model, introduced by Rose and Glover [54] dislocation movement is postulated to be impeded by the interaction between the dislocations and vacancy solute atom pairs. In this model, long range solute diffusion is not required. All these models predict the drops in flow stress under conditions of DSA on the basis either of dislocations breaking away from the pinning atoms or of new dislocations being formed.

2.4 DSA in Austenitic Stainless Steels

Experimental aspects of DSA have been extensively studied in the different grades of austenitic stainless steels. In austenitic stainless steels DSA was reported in a wide range of temperatures depending on the strain rate. The DSA was observed from 300^{o}C up to 700^{o}C in 304 stainless steels [55]. All types of serrated flow and their

mixed modes were reported. Values of activation energy for the serrated flow vary depending on chemical composition, test conditions and on the approach by which the activation energy was calculated [56].

In austenitic stainless steels of type 303, 304, and 330, appearance of serrated flow in the temperature range of about 260 – 460^{o}C represents DSA. In all the studied alloys, the activation energies were related to vacancy migration, which controls the carbon vacancy pair reorientation mechanism of aging, originally suggested to explain DSA. De Almeida et al. [57] have argued that the values of activation energy are close to those for self-diffusion of C or N in pure Ni or γ-Fe, but in multicomponent alloys where Cr is present as an alloying element the activation energy of carbon self-diffusion should be higher. The section of serrated flow in the temperature range of 460 – 600^{o}C was related to C or N self-diffusion only. In 310 austenitic stainless steel, negative SRS was reported for temperature range 300 – 600^{o}C at strain rates of 5×10^{-1} – 5×10^{-5} s^{-1} [58]. The plateau in YS dependency on temperature and increase of UTS with temperature were reported at the strain rate of 5×10^{-5} s^{-1} at temperatures of 300 – 500^{o}C. The activation energies for dislocation segment to overcome obstacles were calculated from the yield stress results obtained at strain rate of $5\times10^{-5}s^{-1}$ and temperature range of 260 – 650^{o}C.

The DSA in nitrogen alloyed austenitic stainless steel was studied by Kim et al. [59]. The mechanical properties of steels with

different nitrogen contents of 0.01, 0.04, 0.10 and 0.15 wt. % were compared by means of tensile tests at temperatures from room temperature up to 750°C and strain rates of 1×10^{-2} – 2×10^{-4} s^{-1}. It was shown that nitrogen alloying increases yield and tensile strength of the steel without reduction in ductility. It has been found that nitrogen alloying shifts the temperature range of serrated flow observation to higher temperatures. The reported temperature ranges of serrated flow at strain rate of 2×10^{-3} s^{-1} were 400 – 600°C for steel with 0.04 % of N and 500-700°C in the case of steel with 0.1% N.

2.5 Effects of DSA on the Material Behavior

DSA phenomena affect various properties of the material, including the forming behavior of sheet metal. It causes an increase in the rate of dislocation multiplication and delay in recovery of dislocation structure, and promotes an increased propensity towards uniform distribution of dislocations in many metals and alloys. Kashyap et al. [60] showed the uniform dislocation distribution in the early stage of deformation at high strains having dense and thick cell walls composed of dislocation tangles in austenitic stainless steel in the DSA temperature regime. This makes the material harder and higher forces are needed to deform.

Morris [61] pointed out that the tendency to produce an array of dislocation increases with an increase in the intensity of DSA. These investigations indicate reduced dynamic recovery in the DSA regime arising from the diffusion of solutes, which affects the rate of dynamic

recovery by pinning of dislocations and thereby preventing screw dislocations to cross slip due to their reduced mobility. This makes the material to become stronger and increase the resistance to fracture.

Crack growth behavior in modified 9Cr–1Mo steel has been studied by Babu et al. [62] and found that it has improved in the DSA regime. Sarkar et al. [63] investigated that ratcheting behaviour of ASS 316 LN has been anomalous in DSA temperature range. Fracture toughness has been studied by Srinivas et al. [64] and found out that toughness is increased in Armco iron in the DSA regime

Although the research on the effects of DSA on material behavior has been going on from last 5-6 decades, providing a vast amount of literature, there has not been any significant study on the effect of DSA in warm forming of ASS.

2.6 Research Gaps in Existing Literature

ASS 316 is the standard molybdenum-bearing grade, one of the most importance materials in the austenitic stainless steels. It has excellent forming and welding characteristics. This material has to be processed through various thermo-mechanical treatments before it is fabricated into final component.

In relation to the existing literature on the formability studies in ASS 316 at elevated temperatures, the research gaps can be summarized as follows:

To date, there is not enough information in literature concerning sheet metal warm forming processes and temperature influence on mechanical properties of ASS. Frechard et al. [23] studied the mechanical behavior of nitrogen-alloyed austenitic stainless steel hardened by warm rolling. Takuda et al. [25] presented the FE analysis of the formability of ASS 304 sheet in warm deep drawing. The experimental and the numerical results show the positive effect of the heating on the drawability. The LDR increases to 2.7 in the warm deep drawing at 150 °C from 2.0 at room temperature. Limited amount of such information in the case of ASS 316 sheets is one of the reasons for the investigation presented in this thesis.

Further, there have been some studies on the identification, characterization and influence of DSA phenomenon in ASS 316 [59, 63], but these are either related to the low cycle fatigue and crack propagation or to the deformation behavior during ratcheting. As far as the author's knowledge, none of the studies in existing literature presents the effect of DSA phenomenon on the warm forming behavior in deep drawing of ASS 316.

Similarly, there has not been any study on FE simulation of warm forming in ASS 316 sheet materials and also on the

development of FLD at elevated temperatures either theoretically or experimentally.

These research gaps form the basis of investigations in this thesis.

2.7 Objectives of the Study

The objectives of this research study are as follows, which address the above research gaps one by one.

1. Characterization of ASS 316 at elevated temperatures along with identification of DSA regime by tensile tests
2. Study of forming behavior in ASS 316 at elevated temperatures by deep drawing experiments
3. FE simulation of forming behavior in ASS 316 at elevated temperatures by deep drawing simulations using LS-Dyna
4. Development of FLD for ASS 316 theoretically by MK analysis and its experimental validation

These objectives are sequentially addressed in this thesis in the following chapters. Chapter 3 focuses on characterization of ASS 316 and identification of DSA regime in it. Chapter 4 presents the formability study of ASS 316 at elevated temperatures by deep drawing experiments followed by its FE simulation using LS-Dyna in Chapter 5. Finally, Chapter 6 covers the development of FLD theoretically and experimentally.

CHAPTER 3:

Material Characterization and Investigation of DSA

This chapter is focused on material characterization by finding material properties through tensile tests at various elevated temperatures till 700^0 C. Tensile test specimens have been prepared from ASS 316 sheets as per subscale ASTM standards (ASTM E-8/21). Tests have been conducted at various elevated temperatures and different strain rates. Tensile properties of the material at these temperatures have been evaluated. Based on the serrations in true stress – true strain graphs, DSA region have been investigated. The fracture behavior of the specimens within DSA and non-DSA has been studied. Lankford coefficients have also been measured to predict the anisotropy of sheet metal

3.1 Blank Material

In this study, 1.0 mm thick sheet of ASS 316 has been used. ASS 316 is molybdenum-bearing austenitic stainless steel which is more resistant to pitting and crevice corrosion than the conventional chromium-nickel austenitic stainless steels. This alloy also offers higher creep, stress-to-rupture and tensile strength at elevated temperatures. This alloy contains 2 to 3% molybdenum, which enhances the corrosion resistance in acidic environments. Resistance to pitting and crevice corrosion in the presence of chloride or other halide ions is enhanced by higher chromium (Cr) and molybdenum (Mo) content [65]. It is primarily in austenitic phase and small quantities of ferrite may be present. Due to the presence of these phases it has excellent toughness besides high strength. These

combinations of properties provide the excellent fabricability and formability to the material [66].

Chemical composition of the as-received ASS 316 sheets has been found using the spark emission spectrometer. Spark source in the spectrometer has a relatively high precision, accurate, and suitable source for the routine analysis of metals. This is a method that use the intensity of light emitted from a flame or spark, at a particular wavelength to determine the quantity of an element in a sample. The wavelength of the atomic spectral line gives the identity of the element, while the intensity of the emitted light is proportional to the number of atoms of the element. A sample of a material is brought into the flame or directly inserted into the flame by use of a small loop of wire. The heat from the flame evaporates the solvent and breaks chemical bonds to create free atoms. The thermal energy also excites the atoms into excited electronic states that subsequently emit light when they return to the ground electronic state. Each element emits light at a characteristic wavelength, which is dispersed by a grating or prism and detected in the spectrometer [67].

Standard test method for optical emission vacuum spectrometric analysis of carbon and alloy steel is ASTM E 415. This test method covers the simultaneous determination of 20 alloying and residual elements in carbon and alloy steels in certain concentration ranges. Chemical composition of as-received ASS 316 sheets is listed

in Table 3.1. This spectrometric analysis has been carried out at Jyothi Spectro Labs, Hyderabad.

Table 3.1: Chemical composition of as-received ASS 316 sheets

Element	Fe	Cr	Ni	Mo	Si	Mn	Cu	Co	C
Composition (Wt. %)	67.69	6.6	0.8	2.42	1.28	0.38	0.21	0.21	0.018

3.2 Tensile Testing

Tensile test specimens were prepared according to sub-size of the ASTM E8standard. The specimen is flat sheet type with the gauge length of 30 mm, width of 6.4 mm and thickness of 1 mm as shown in Figure 3.1. These specimens have been cut from 1mm thick sheet by wire-cut Electron Discharge Machine (EDM). This is an electro thermal process of metal cutting, in which electrode is used to cut through metal by the use of heat from electrical sparks. It is applicable to parts which are electrically conductive. Instead of cutting the material, EDM melts or vaporizes it, leaving little debris and providing a very accurate size and shape. Wire-cut EDM uses a metallic wire as an electrode to cut a programmed contour in the work piece. It discharges the electrified current, which acts as the cathode and is guided alongside the desired cutting path. There is never any mechanical contact between the electrode and work piece. The wire is usually made of brass or stratified copper, and is between 0.1 to 0.3 mm diameters. A dielectric fluid submerges the wire and work piece,

filtering and directing the sparks. The thin wire allows precision cuts, along the cutting path, which have a positional accuracy of +/- 0.005 mm.

Tensile tests have been performed according to the standards ASTM E8/E21 (Standard Test Method for Elevated Temperature Tension Tests of Metallic Materials) in air environment. Tensile tests have been conducted on a universal testing machine, as shown in Figure 3.2. It is an electronic screw driven machine with precision screw, column construction and completely computer controlled. It has variable speed drive. Tensile tests have been carried out at different constant strain rates. The rate at which strain is applied to the specimen has an important influence on the flow stress of the material.

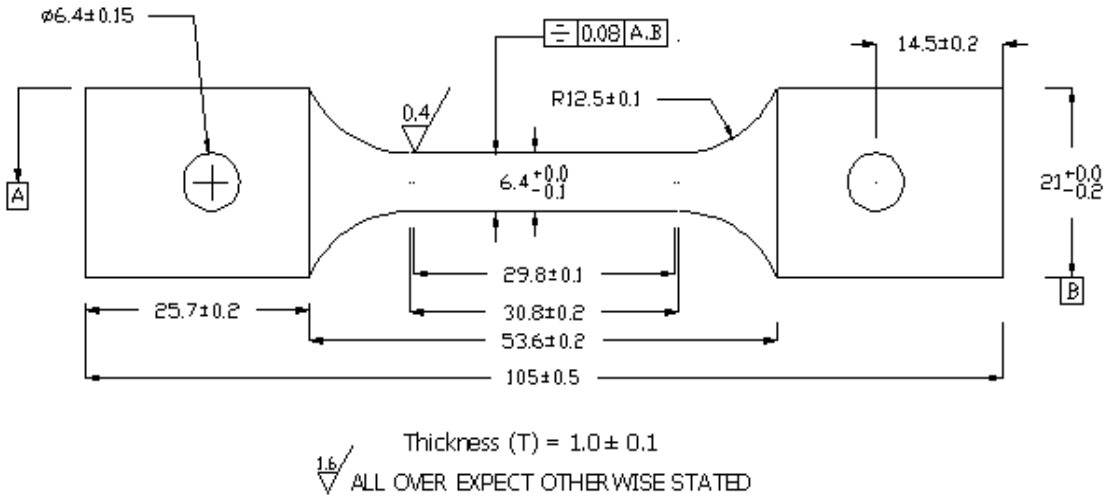

Figure 3.1: Tensile test sub-sized specimen as per ASTM E8

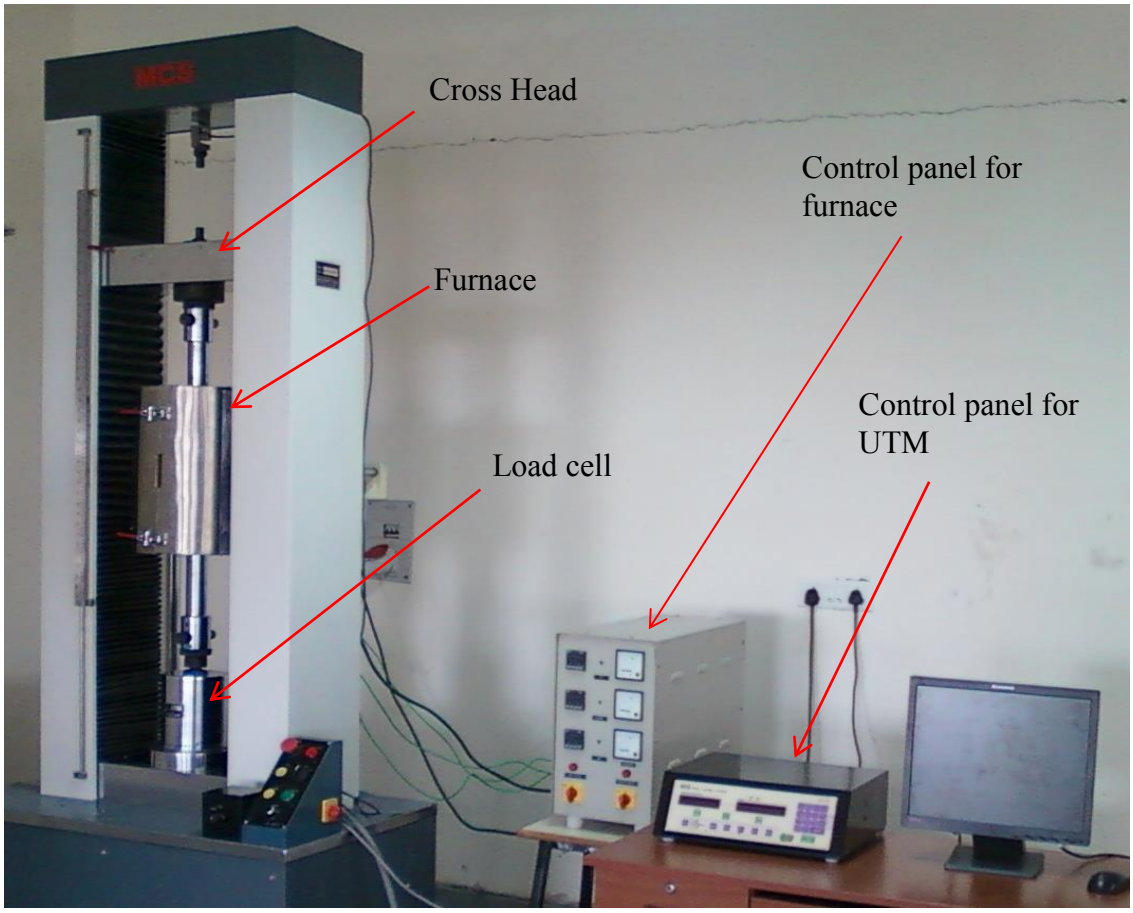

Figure 3.2: Universal testing machine

Strain rate can be defined as the rate of change in strain (deformation) of the material with respect to time. This can be given in Equation 3.1 and expressed in units of per second (s^{-1}). At lower plastic strain, flow stress is more influenced by strain rate than the strength of the material. High strain rate causes yield point to appear during early stage of tensile test.

$$\dot{\varepsilon} = d\varepsilon / dt \tag{3.1}$$

UTM is equipped with a pinned grip arrangement to fix the flat tensile test specimen. The crosshead speed is given by Equation 3.2. The strain rate is expressed in terms of linear strain as given in Equation 3.3. The true strain rate is given by Equation 3.4, which

indicates that in constant crosshead speed true strain rate decrease as the specimen length continuously increases due to tensile force acting on it. To maintain constant true strain rate, cross head speed must increase proportionately to the length of the specimen. The speed is continually controlled by a closed loop control proportional-integral-derivative (PID). The instantaneous crosshead speed is governed by Equation 3.5, where t is the time interval.

$$V = dl\ /dt \tag{3.2}$$

$$\dot{e} = \frac{de}{dt} = \frac{d(L-L_0)/L_0}{dt} = \frac{1}{L_0}\frac{dl}{dt} = \frac{v}{L_0} \tag{3.3}$$

$$\dot{\varepsilon} = \frac{d\varepsilon}{dt} = \frac{d(L-L_0)/L}{dt} = \frac{1}{L}\frac{dl}{dt} = \frac{v}{L_i} \tag{3.4}$$

$$V = \dot{\varepsilon} L_0\ exp\ (\dot{\varepsilon} t) \tag{3.5}$$

PID controller has a generic control loop feedback mechanism. This is widely used in industrial control systems. A PID controller calculates an "error" value, in equal time intervals, as the difference between a measured process and a desired set point. The controller attempts to minimize the error by adjusting the process control inputs. Here, PID measures the true strain rate of the specimen at the time interval of 10 micro seconds and calculates the deviation in strain rate (error) with the set strain rate. The crosshead speed keeps adjusting proportional to the elongated length of the specimen so that the strain rate maintains the set value.

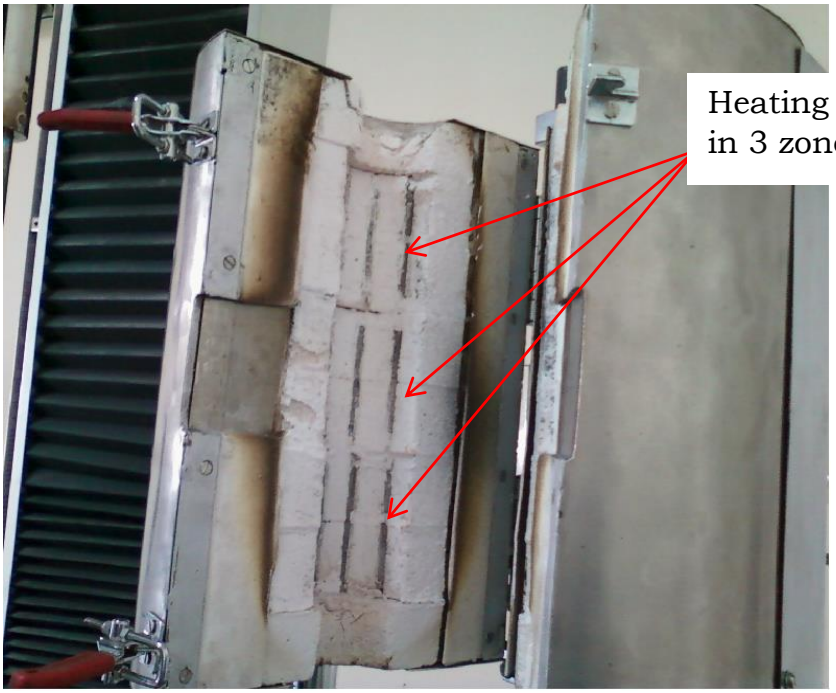

Figure 3.3: Split furnace with 3-zone heating attached to UTM

For conducting the test at higher temperatures, UTM is attached with a special type 3-zone split furnace as shown in Figure 3.3. It has uniform distribution of heating coils, which are arranged in three zones to achieve temperature up to 1000°C with ± 1°C accuracy. Temperature measurement and control has been done by thermocouples.

Uniaxial tensile tests have been performed at temperatures between 50°C to 700°C in the interval of 50° C and at strain rates of $1x10^{-1}$, $1x10^{-2}$, $1x10^{-3}$ and $1x10^{-4}$ per sec. From these test data, the true stress – true strain curves have been plotted. The effect of strain rate and temperature on the tensile properties have been evaluated and compared. The typical stress-strain curves at a constant strain rate of $1x10^{-2}$ s^{-1} and for different temperatures are shown in Figure

3.4. Constant temperature of 100°C and at different strain rate, true stress – true strain curves are shown in Figure 3.5. From these curves, it can be observed that the mechanical properties are dependent on the test temperature and strain rate.

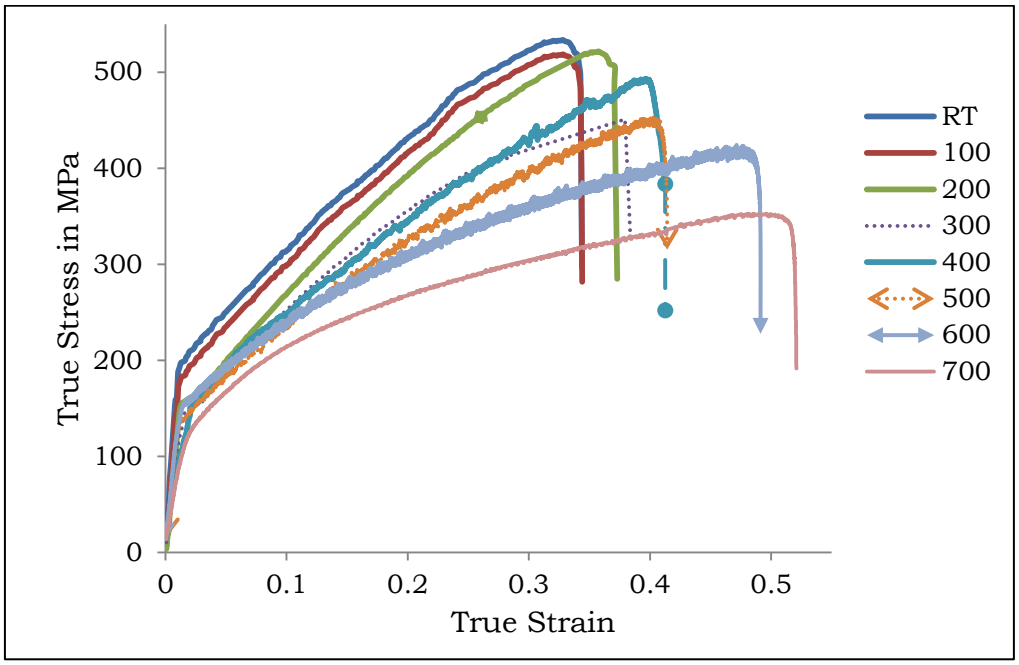

Figure 3.4: True stress vs. true strain at different temperatures and constant strain rate of 1x10-2 s-1

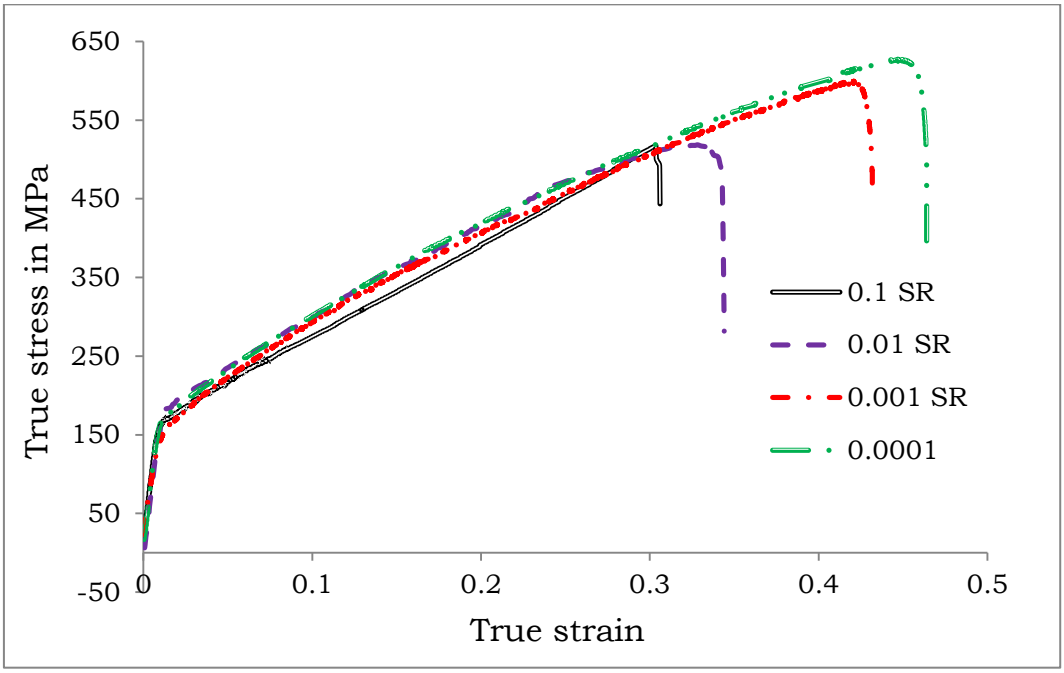

Figure 3.5: True stress vs. true strain at different strain rates at 100°C

From Figures 3.4 and 3.5, it can be observed that the strength of the material gets more affected by the temperature than the strain rate. Strength of ASS 316 decreases with the increase in the temperature due to the reduction in flow stress. This decrease is slow at lower temperatures, but drastically falls at higher temperatures. This is because in ASS 316 diffusion rate is higher at these temperatures and flow stress is decreased more at higher temperatures. In the interval of 400 to 600°C, serrations have been observed in true stress-true strain curves at lower strain rates due to impurity segregation in the slip planes. It is observed that the strain rate doesn't have much effect on the flow stress of the material, but it delays the fracture point of the specimen. It is because the strain rate has no influence on the diffusion rate, but it slows down the dislocation motion which results in delay of the fracture point and thus leads to more elongation. This leads to increase in the fracture strain and also in the ultimate tensile strength. For a sample, the mechanical properties of the material obtained by uniaxial tensile tests at a strain rate of $1x10^{-2}$ per second and different temperatures are given in Table 3.2.

Table 3.2: Mechanical properties of ASS 316 at different temperatures and at a strain rate of $1x10^{-2}$/sec.

Temperature	Young's modulus (in GPa)	Yield strength (in MPa)	Strain hardening index (n)	Hardening co-efficient (K) (in MPa)
Room Temp	205	182.34	0.3419	1106
100 °C	196.4	178. 63	0.3341	987.9
150 °C	194.3	175.63	0.3281	984.9
200 °C	182.4	172. 63	0.3271	935.8
250 °C	175.5	170.65	0.3186	908.6
300 °C	149.5	169.3	0.3102	872.5
350 °C	146.7	156.9	0.312	859.6
400 °C	145.2	153.7	0.3673	968.7
450 °C	143.6	152.2	0.3663	972.5
500 °C	142.2	150.7	0.3703	988.7
550 °C	141.3	142.6	0.368	949.6
600 °C	138.2	141.8	0.352	849.3
650 °C	134.6	138.6	0.321	824.6
700 °C	132.2	121.8	0.302	789.3

Two trends have been observed in Figure 3.4; firstly the slope of each curve is different at each temperature and decreases with an increase in the temperature. This is because of the decrease in strain hardening of the material at elevated temperatures. The other trend is that the increase in tensile stress is more at lower temperatures than

that at higher temperatures. This is expected as the creep deformation makes a larger contribution to the strength reduction at high temperature and low strain rate. Elongation of the materials does not always increase with increase in temperature or decrease in strain rate. Highest ductility is usually obtained at a certain temperature and strain rate. A possible explanation for this phenomenon is that the peak value of elongation at high temperature results from the interaction between work hardening and dynamic recovery.

Serrations in the stress–strain curve have been observed at lower strain rates and at a certain temperature range. True stress vs. true strain graphs have been plotted for the test data at low strain rate of $1x10^{-4}$per second as shown in Figure 3.6. Serrations in the stress–strain curves are clearly visible in the temperature range of 400°C to 600°C. Outside this range, serrations are absent in the whole range of the strain rates. Table 3.3 provides a summary of the results of these observations regarding the presence of serrations in true stress vs. true strain curves.

Table 3.3: Presence of serrations in true stress vs. true strain curves ('Y' represents presence; while 'N' represents absence)

Strain Rate (/sec)	Temperature (°C)													
	50	100	150	200	250	300	350	400	450	500	550	600	650	700
$1x10^{-1}$	N	N	N	N	N	N	N	N	**Y**	**Y**	**Y**	**Y**	N	N
$1x10^{-2}$	N	N	N	N	N	N	N	**Y**	**Y**	**Y**	**Y**	**Y**	N	N
$1x10^{-3}$	N	N	N	N	N	N	N	**Y**	**Y**	**Y**	**Y**	**Y**	N	N
$1x10^{-4}$	N	N	N	N	N	N	N	**Y**	**Y**	**Y**	**Y**	**Y**	N	N

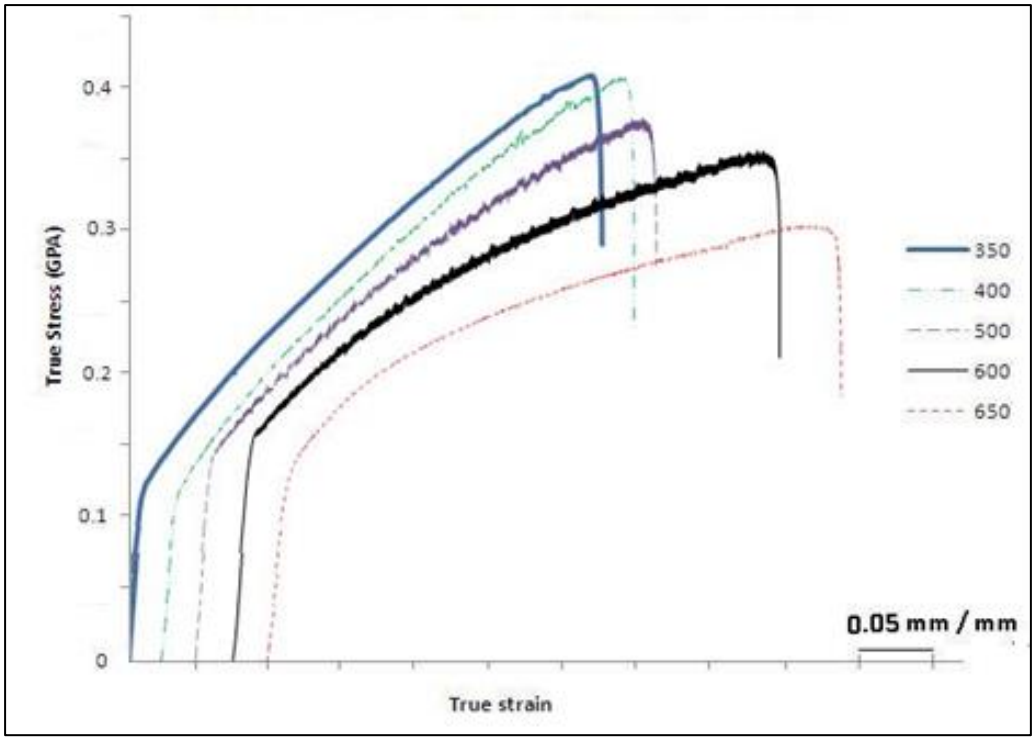

Figure 3.6: Flow stress curve at constant strain rate of 10-4 sec-1

The strain rate sensitivity (SRS) index is considered one of the parameters that can characterize DSA phenomena. The flow stress equation that describes plastic behavior is usually written by power law as presented in Equation 3.6, where σ is the flow stress, K is a material constant, $\dot{\varepsilon}$ is the strain rate and m is the SRS index of the flow stress [68]. The most convenient method for determining m is the uniaxial tensile test at a constant temperature and at different strain rates. Power law can be simplified by considering strain as constant and the modified formula is given in Equation 3.7, where C is a constant.

$$\sigma = K\varepsilon^{n}\dot{\varepsilon}^{m} \tag{3.6}$$

$$\sigma = C\ \dot{\varepsilon}^{m} \tag{3.7}$$

The *m* value is usually measured from the log – log plot of the flow stress vs. strain rate. Figure 3.7 presents the log-log plot between true stress and strain rate within the DSA range at a true strain of 0.2. The *m* values have been calculated from the slopes of these curves. SRS index has been tabulated in the temperature range of 350°C to 650°C in Table 3.4. It can be seen that *m* has a negative value in the temperature range of 400°C to 600° C. Negative strain-rate sensitivity along with the appearance of serrations in the true stress– true strain curves confirms the presence of DSA phenomena. With these observations it can be concluded that in ASS 316, DSA occurs within a temperature range of 400°C to 600°C at almost all strain rates. It has also been observed that the strain rate sensitivity decreases with the increase in temperature in the DSA regime. Similar results have been reported in low carbon steel in [69] and subsequently analyzed in detail by McCormick [70]. This is resulting from diffused solute atoms, temporarily arrested dislocations at obstacles in the slip path. This serrated flow is originated due to the pinning of dislocations by solute atoms of *Cr* in ASS 316, which attribute to the occurrence of DSA phenomena.

Table 3.4: SRS index (*m*) at various temperatures in DSA regime

Temp	350	400	450	500	550	600	650
SRS index	0.0153	-0.0059	-0.008	-0.0101	-0.0123	-0.0195	0.0174

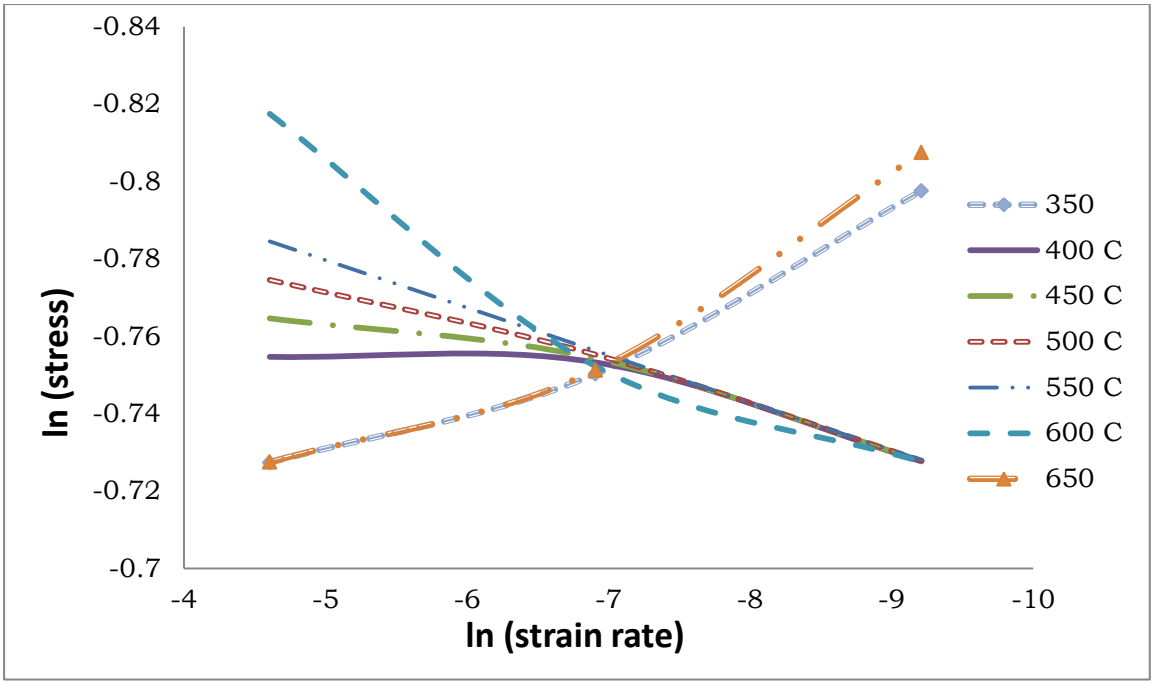

Figure 3.7: Log-log plot of true stress vs. strain rate at 0.2 true strain

Mobile solute atoms tend to cluster at dislocations, driven by their primarily elastic interaction with the strain field generated by the defects. Clustering leads to an enhancement of the apparent lattice resistance to dislocation motion. In the current physical picture of DSA, it is considered that, if the solute has sufficient mobility, clustering may occur during the relatively short time. Mobile dislocations are arrested at obstacles such as forest dislocations, precipitates and grain boundaries. Clustering is assumed to occur either by lattice diffusion, from the lattice to the arrested mobile dislocation, or by diffusion, from the solute cluster on the forest dislocation, along the core of the mobile dislocation. These microscopic mechanisms lead to negative strain rate sensitivity [71].

It was observed that diffusion must be assisted by vacancies in order to occur at reasonable rates at room temperature. However, it is now accepted that vacancies do not play a central role in DSA. They certainly favor the effect by enhancing the diffusion, but the DSA mechanism must be independent of their presence and concentration. Not affected by the vacancies, diffusion appears to be slow in this material system, at lower temperature. In turn, this implies that clustering of mobile dislocations during their arrest time at obstacles, by diffusion, is too slow for the mechanism to explain the macroscopic phenomenon [72].

At higher strain rates, when the average arrest time is short, the clusters are too small to produce an effective enhancement of the strength and the DSA effect is not observed. Clustering contributes to the intrinsically unsteady motion of dislocations during which a higher resolved shear stress is needed to break free the defect from the cloud, while a relatively low stress is required to keep it moving after this event. This process leads to negative strain rate sensitivity and strain localization. The temperature is important since it controls solute mobility and clustering rate.

In the graph, serrations have been observed even at 350 and 650°C, but these are near to fracture point. Serrations start immediately after yielding in DSA. The serration observed at fracture point is due to the conditions of fracture. Before fracture, necking starts at the internal layers of material and it propagates to entire

cross section, which leads to fracture. It has been observed that the fracture topography differs in non-DSA and DSA regimes. To understand the nature of fracture in tensile test specimens in DSA and non-DSA regimes, the fracture study has been presented in the next section.

3.3 Fracture Study

Scanning electron microscope (SEM) is used to study the fracture. SEM is a scientific instrument that uses a beam of energetic electrons to examine objects on a very fine scale. It tracks local material abnormalities that act as crack initiators. The observed micro-voids can be generated from non-metallic inclusions. Voids on the surface may be initiated the inclusions or nucleated at precipitated carbide. The SEM has a large depth of field, which allows a large amount of the sample to be in focus at one time and produces an image up to 10,000X magnification. The combination of higher magnification, larger depth of field, greater resolution, compositional and crystallographic information makes the SEM as one of the most widely used instruments in the lab for fracture study [73].

The surface of a specimen is brought into the focus of electron beams. The signals control the brightness of a screen tube such that an image of the surface of the sample can appear. Any fracture of a body starts with the formation and propagation of cracks in sub-microscopic, microscopic, and eventually macroscopic dimensions. The structure of the fracture surface varies depending on the

composition and microstructure of the material as well as on other conditions applied during the process of breaking, such as temperature and strain rate. Thus, an analysis of the fracture surface can provide essential information on the cause of fracture. Ductile fracture occurs in formable metals that go through significant plastic deformation. The brittle fracture occurs without significant plastic deformation. This type of fracture appears generally in BCC or HCP metals. The crack starts through or along the grain boundaries. The propagation of the crack is fast and the fracture is characterized as a cleavage fracture.

SEM photographs of the fractured surface of tensile specimens at 300°C and 550°C are shown in Figure3.8 at different magnifications. There is a significant difference in the fracture surface topology. Fracture usually occurs under single load or tearing in ductile material. This is shown by depressions in the microstructure, called as dimples, which occur from micro-void emergence in places of high local plastic deformation. The observed micro-voids can be generated from non-metallic inclusions. For example, voids on the surface may be initiated by carbide inclusions or nucleated at precipitates. At 300°C, the large dimples are seen, which may be due to non-metallic inclusions. Under increased strain, micro voids grow, coalescence until rupture occurs, and leads to formation of dimples. Dimple size and shape depend on the type of loading and extent of micro-void emergence. When a material is put under uniaxial tensile loading, equi-axed dimples appear which have complete rims. Under a

shear loading the dimples are elongated, the rims of the dimples are not complete and the dimples are in the same direction as the loading. Oval dimples occur when a large void intersects a smaller subsurface void and exhibit complete rims [74].

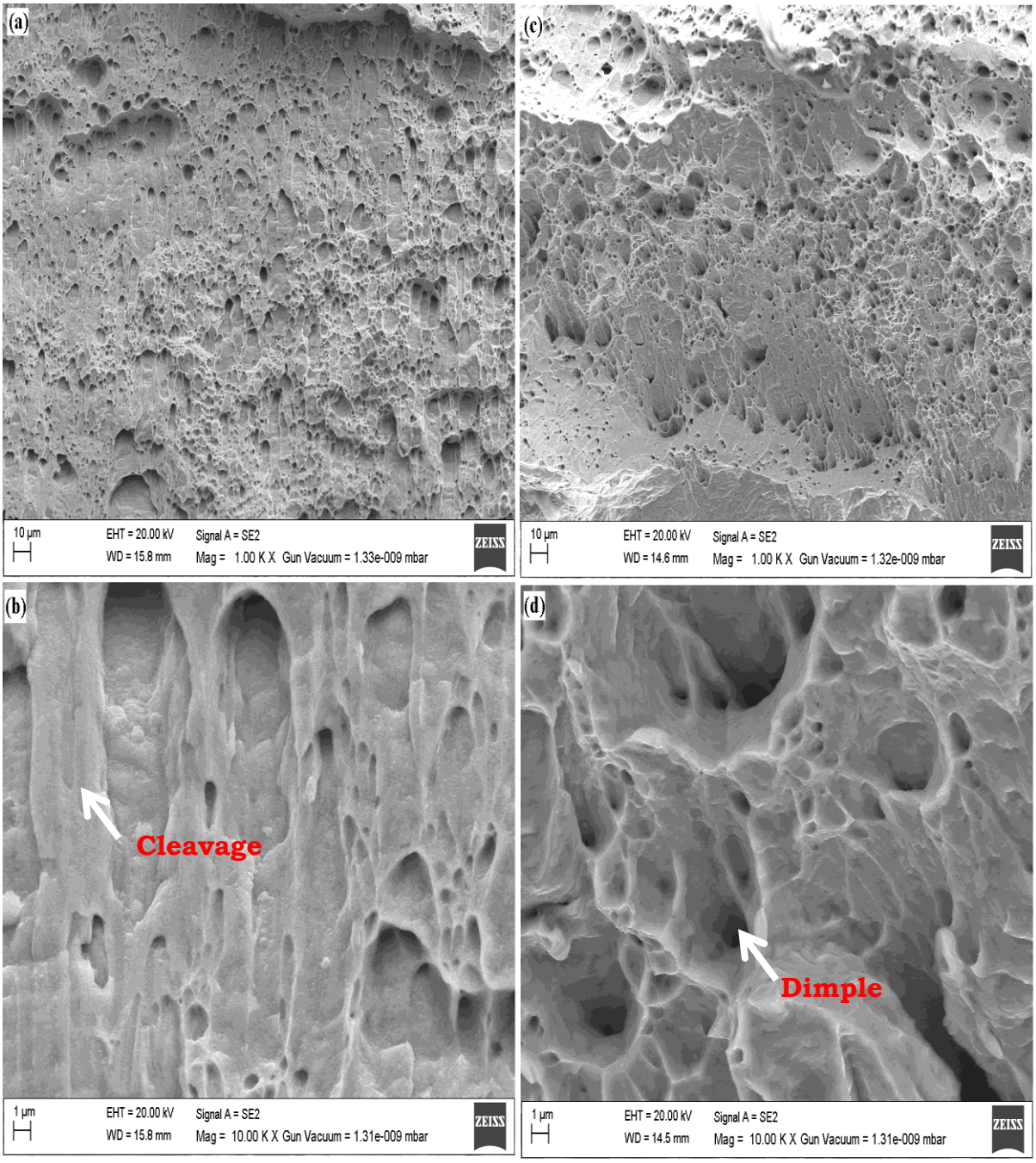

Figure 3.8: SEM photographs of the fracture surface in the specimens at 300°C and 550°C (a) 1000 X at 550° C (b) 10, 000 X at 550° C (c) 1000 X at 300°C (d) 10, 000 X at 300°C

Fracture surface at 550°C consisted of small dimples and flat areas looking like semi-cleavage. The flat area of fracture occurs without significant plastic deformation. These also look like quasi-cleavages. Cleavage results from high stress along three axes with a high rate of deformation. Characteristics of cleavage are cleavage steps, feather markings, herringbone structure, tongues and micro-twins and quasi-cleavage. A cleavage step is a step on a cleavage facet joining two parallel cleavage fractures. Feather markings are very fine, fan like markings on a cleavage fracture. Quasi cleavage is a fracture mode resembling cleavage because of its planar facets, but where the fracture facets are not specific well-defined planes.

This difference of fracture surface is in agreement with variation of the nature of fracture of these conditions. In the non-DSA region at 300°C fracture occurred through significant plastic deformation resulting in large dimples which confirms the nature of fracture to be ductile. Whereas in DSA region at the 550°C, fractured surface had small dimples and quasi-cleavages, which shows that fracture is less ductile. This indicates that in the DSA region, the ductility of the material decreases.

Few of SEM photographs of non-DSA are shown in Figure: 3.9 at lower magnifications. It shows that fracture is full of dimples and can be considered as a ductile fracture. Figure 3.10 shows the fractured surface of specimen in DSA region, which have few dimples, but large areas of flat surface, i.e., cleavages. With this, it can be

concluded that in DSA region material is less ductile and fracture type is mixed mode fracture.

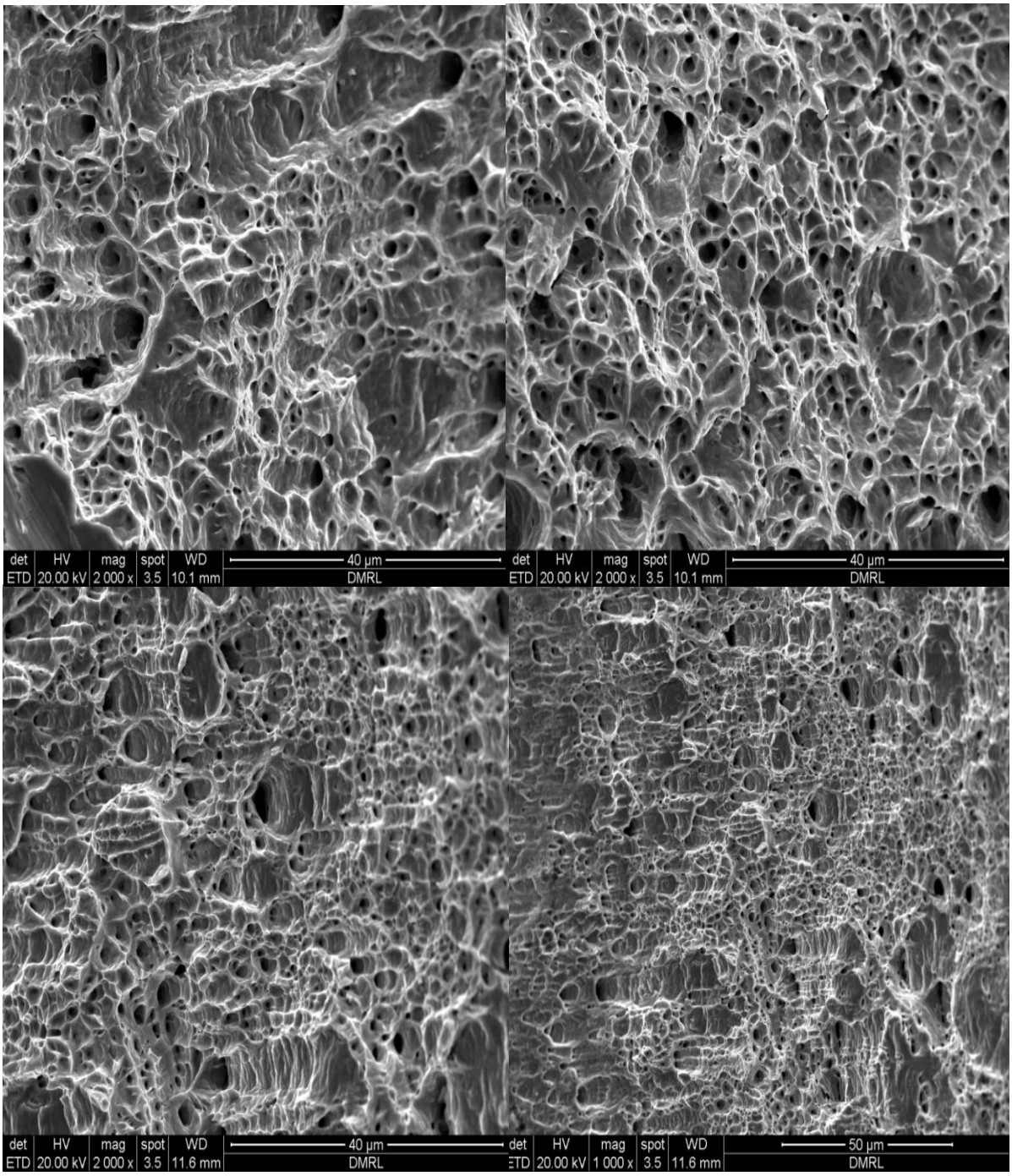

Figure 3.9: SEM photographs of the fractured surface in non-DSA region

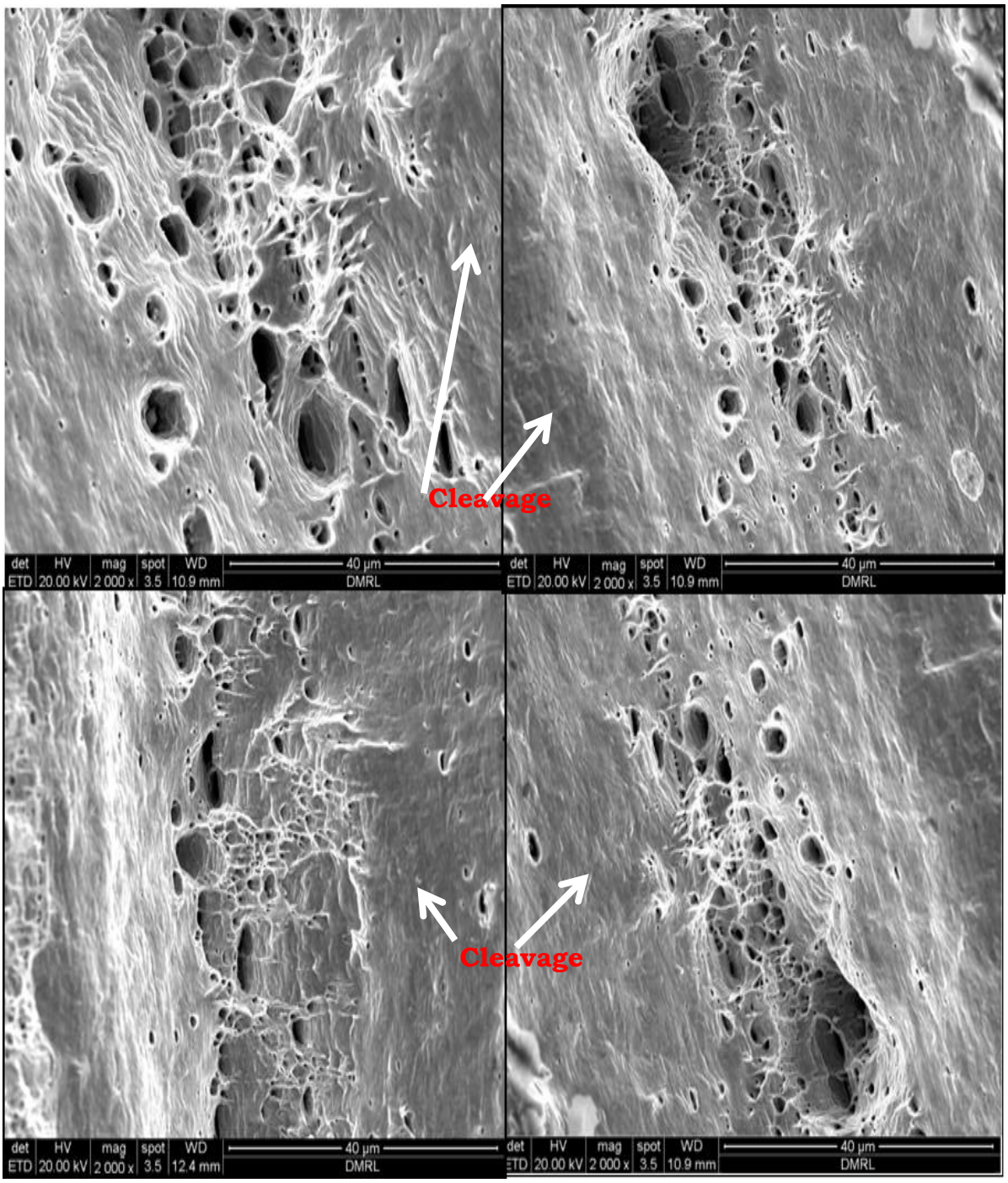

Figure 3.10: SEM photographs of the fractured surface in DSA region

3.4 Evaluation of Anisotropy

Anisotropy is defined as the directionality of properties and it is associated with the variance of atomic or ionic spacing within crystallographic directions. Single crystals cause variations in properties in different crystallographic directions. The extent and magnitude of anisotropic effects in the crystalline materials are the functions of the symmetry of the crystal structure [75]. Since common engineering materials are polycrystalline, the crystallographic orientations of the individual grains are totally random, if complete re-crystallization has taken place. Although all grains have certain anisotropy, the overall structure behaves isotropic, since the anisotropy effect is averaged out. However, if the materials are deformed for instance with no complete recovery, the crystal grains are oriented in deformation specific directions, making the material anisotropic. During deformations, the crystal lattices rotate and they affect the plastic properties [76].

In the sheet metals, crystal lattices are oriented in specific direction during rolling of the sheets, which make them more anisotropic. In sheet material, plastic anisotropy is measured with the *R*-value, which is Lankford coefficient and it measures the tendency of the sheet to become thin under deformation. The Lankford coefficient is an indicator of the plastic anisotropy of a rolled sheet metal which is critical in deep drawing [77]. The anisotropy is characterized into normal and planar anisotropy. Normal anisotropy influences the

maximum drawability of sheet, whereas planar anisotropy leads to earring [78].

Lankford coefficient represents the directional differences in a rolled sheet material. To evaluate plastic anisotropy behavior, the Lankford coefficient is evaluated through uniaxial tensile tests. The ratio between the strains is calculated through the conservation of volume and the measured data.

$$R = \frac{\varepsilon_w}{\varepsilon_t} = \frac{\varepsilon_w}{-(\varepsilon_w + \varepsilon_l)} \tag{3.8}$$

where ε_w is the strain in width, ε_l is the longitudinal strain and ε_t is the thickness strain in a uniaxial tension test. This is normally carried out with samples cut from the sheet at 0, 45 and 90 degrees to the rolling direction as shown in Figure 3.11. Since the *R*-values vary for different directions, an average value can be used as normal anisotropy (R_n), and is measured as:

$$R_n = (R_0 + 2R_{45} + R_{90})/4 \tag{3.9}$$

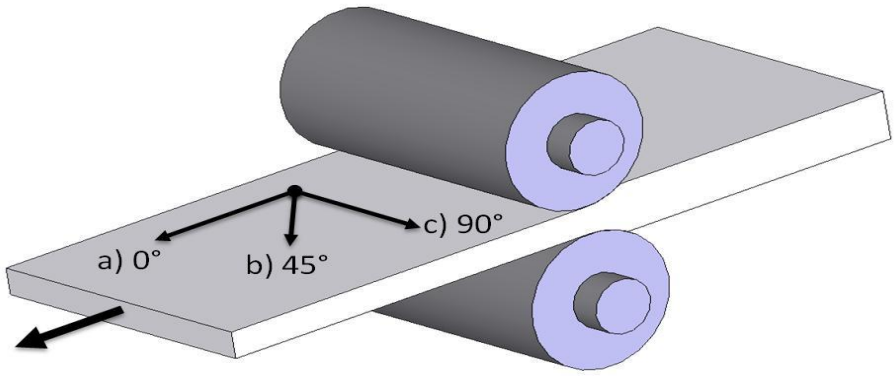

Figure 3.11: Directionality in the rolled sheet

A material with a higher R_n value, experience less thinning during the deep drawing operation than a material having a smaller R_n value, provided that their flow characteristics are identical. Materials having greater *R*-values are more suitable for deep drawing. Their deformation resistance also increases with the increase in R-values [79]. The materials having a normal anisotropy value larger than unity experience that the width strain is greater than the thickness strain under the tensile force. This is due to having a greater strength in the thickness direction and offering a resistance to thinning. It leads to deeper parts to be drawn and allows in shallow, smoothly contoured parts (like automobile panels). Higher value of R_n may reduce the chance of wrinkling or ripples in the part. So, for a deep drawing operation, a suitable material must have an *R*-value relatively larger [80].

Generally, the *R*-value of cold rolled steel sheet used for deep-drawing shows the heavy orientation, and such deep-drawability is characterized by normal anisotropy. However, in the actual press-working, the deep-drawability of steel sheets cannot be determined only by the value of R_n , but also by the planar anisotropy. A measure of the variation of normal anisotropy with the angle to the rolling direction is given by the quantity ΔR, known as planar anisotropy.

$$\Delta R = (R_0 - 2R_{45} + R_{90})/2 \tag{3.10}$$

In this anisotropic parameter, *R*-value is evaluated through uniaxial tensile tests. For this gauge length was divided into 5 equal segments along the length by a fine scriber. Width and length of these segments were measured before tensile testing. These divisions are made in order to increase the accuracy of measurement. A tensile test experiment has been conducted up to plastic strain and stopped before the specimen fracture. Normally, the specimen should be elongated upto 0.2 strain and then stopped. After removing the specimens from the pinned grippers, their final length and width at all 5 segments have been measured. Width strain (ε_w) and length strain (ε_l) were measured and substituted in Equation 3.8 to find '*R*'. These experiments were repeated in 0°, 45° and 90° direction of rolling to get Lankford coefficients in these directions. Using these *R* values, normal and planar anisotropy have been calculated and presented in Table 3.5 for ASS 316.

There is not much effect of temperature on Lankford coefficient. Normal anisotropy (R_n) is not affected much by an increase in temperature. Above 400°C, where DSA has been observed, these parameters are uncertain and there is not any direct effect of temperature. Planar anisotropy (ΔR) has been found less in this temperature range. At 400°C and above, ΔR is observed to have sudden increase, which negatively effects on formability and drawability. Further investigations of these behaviors were carried out by experimentation and simulation of deep drawing.

Table 3.5: Lankford coefficient for ASS 316 at different temp

Temperature	R_0	R_{45}	R_{90}	R_n	ΔR
Room Temp	0.8178	1.204	1.811	1.259175	0.4398
100 °C	1.108	1.376	1.89	1.4375	0.492
150 °C	1.228	1.076	1.68	1.438	0.492
200 °C	1.159	1.219	1.58	1.29425	0.602
250 °C	1.022	1.29	1.68	1.3205	0.244
300 °C	0.916	1.214	1.824	1.292	0.6256
350 °C	1.19	1.214	1.544	1.2904	0.6128
400 °C	0.8022	1.09	1.873	1.2138	0.9904
450 °C	1.08022	1.194	1.987	1.36388	1.35904
500 °C	0.809	1.013	1.663	1.1244	0.8912
550 °C	1.09	1.13	1.663	1.25315	0.9852
600 °C	0.817	1.614	1.678	1.43075	1.466
650 °C	1.07	0.941	1.678	1.1577	1.7304
700 °C	1.099	1.313	1.7	1.35625	0.346

From this chapter it has been observed that the mechanical properties are strongly dependent on the test temperature and strain rate. As the temperature increases strength decreases slightly at lower temperatures, but drastically decreases at higher temperatures. Strain rate has less effect on the flow stress of the material, but it delays the fracture point. As the strain rate decreases, material elongates to

higher strain and increases the ultimate tensile strength. In the interval of 400 to 600°C, serrations have been observed and also SRS index is found to have negative values. These indicate the presence of DSA region in the temperature range of 400 to 600°C in ASS 316.

Sheet metal under investigation is anisotropic and is not much affected by temperature. Above 400°C, where DSA has been observed, these parameters are uncertain and there is not any direct effect of temperature. At 400°C and above, ΔR has been found to have sudden increase, which negatively affects the formability and drawability. There is a significant difference in the fracture surface in non-DSA and DSA regimes. In the non-DSA region, fracture is occurred by significant plastic deformation, which shows that the fracture is ductile; whereas in the DSA region, fractures are less ductile. DSA phenomena negatively affect the formability of the material. A common method for assessing formability is to determine the limiting draw ratio (LDR) and thickness distribution. The next chapter covers the deep drawing experiments along with the measurement of LDR and thickness of the drawn cups.

CHAPTER 4:

Experimental Study of Deep Drawing

This chapter is focused on the deep drawing experimentation. Experimental setup has been developed to carry out deep drawing experiments on ASS 316 at different elevated temperatures. After performing the deep drawing experiments, LDR and thickness distribution of the drawn cup have been measured for understanding the formability of ASS 316. The effect of different process parameters on the sheet formability has also been studied.

4.1 Experimental Setup of Deep Drawing

In deep drawing, the blank material draws into the die by the action of the punch and flows into a three dimensional shape. Deep-drawing takes place without damaging the material structure, therefore it is very much suitable for producing many different shapes. This process offers an enormous saving potential compared to other manufacturing processes.

The deep drawing process begins with metal blanks where typically single blanks are used in order to facilitate the creation of parts or products with deeper shapes. Sometimes, these metal blanks are placed on a reel to enable the metal to form efficiently. At each step in the deep drawing process, the metal blank is shaped through the pressure applied by a punch. Deep drawing is especially beneficial when producing high volumes, since the unit cost decreases considerably as unit count increases. Once the tooling and die have been created, the process can continue with very little downtime.

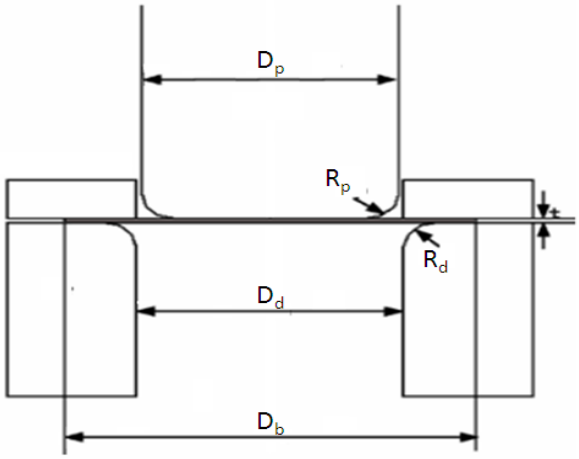

Figure 4.1: Deep drawing parameters

Deep drawing tool construction costs are lower in comparison to similar manufacturing processes even in smaller volumes. Using the simplicity of the axis-symmetric deep drawing, one can describe the basic parameters in deep drawing. The basic geometry and material parameters in a simple cup drawing operation are shown in Figure 4.1 [81].

Punch size (D_p), punch corner radius (R_p), die opening (D_d), die corner radius (R_d) and blank size (D_b) are the important physical parameters which affects the deep drawing process. The clearance between die opening and punch is another important parameter. Its value is important as the punch enters the die cavity, depending on the blank thickness at the die cavity. Small clearance may lead to ironing, which is simply the intentional thinning of the blank at the die cavity. Normally, to avoid ironing, the clearance must be larger than the blank thickness (t). Usually, the clearance is 20% larger than the initial blank thickness. The other parameters which affect the

deep drawing operations are blank holder force, punch speed, lubrication, properties of blank material.

In a typical deep drawing process, a circular blank of radius R_0 and thickness t_0 is drawn by a flat-bottomed punch through a die opening of radius r_1 with a constant blank-holding force. Under plane-strain conditions, the thickness in the flange region of the drawn cup is variable [82]. Normal anisotropy and planar anisotropy are assumed to be radially symmetrical in the sheet metal.

The amount of drawing performed on a blank can be quantified in terms of the drawing ratio, *DR,* which is calculated as D_b/D_p . Depending on the geometry, forces, metal flow, and material properties, there is a limit to the amount of drawing that can be performed on a blank in a single operation. Drawing ratios can help to determine the maximum amount of drawing possible.

The force used to accomplish a deep drawing operation must be adequate enough to provide necessary forces for the material deformation and flow during the process, and also to overcome friction. Magnitude of force must not be too high or applied incorrectly; otherwise it leads to tearing of the sheet metal. The punch and the blank holder exert separate forces and the force analysis has to be done for both.

For deep drawing experiments, the blanks from ASS 316 have been made into the circular shape of different diameters in the increment of 2 mm from 60 mm onwards using shearing, machining

and grinding. Multiple blanks were held on the lathe machine between the head and tail stocks with suitable supports. After fixing the blanks on the lathe machine, blanks were machined with care by giving the small depth of cut (0.05 mm). Burrs and chips were removed by smooth grinding at the edges.

4.2 Deep Drawing at Room Temperature

The experimental setup required for conducting deep drawing consists of die, punch, blank holder, a power source (Hydraulic power source) to apply punch force and blank holding force, instrumentation to measure load and displacement of the punch (load cell and displacement encoder), and data acquisition system. The experimental setup is shown in Figure 4.2. A hydraulic press is used which is specially designed to conduct deep drawing experiments at different temperatures with the given specifications. Four pillars are used for the support of hydraulic cylinders and for the smooth movement of blank holding plate. Alignment of the die, punch, pistons and cylinders of the hydraulic system has been properly ensured. Inconel die and punch have been manufactured on CNC lathes and tested for geometrical features such as cylindricity, ovality, taper, etc. The outer surface of the punch and inner surface of the die are finished by buffing process. Lubricants are used to reduce friction between the working material and the tools, which also aids in removing the part from the punch. Lubricant films on both sides of the work piece help in getting a fine surface.

The specifications of the experimental setup are given as follows:

Capacity of the press	:	20 tons
Electrical motor HP	:	5 HP
No of main cylinders	:	1 no
Blank holder ram bore diameter		40 mm
Blank holder ram rod diameter		25 mm
Blank Holder ram stroke	:	300 mm
No of blank holder cylinders	:	2 no's
Pressing speed	:	30~ 500 mm/min
Max operating pressure	:	140 Kg/cm^2

Figure 4.2: Deep drawing experimental test setup

Die, blank holder and punch in a typical deep drawing operation are designed in such a way that excessive stress concentration does not appear in any part of the drawn cup. Around 2% of the yield stress is applied on the blank holder to avoid wrinkling of the sheet as the compressive hoop stresses develop in the flange region of the cup. Also, if the blank holding pressure is more, there will be a fracture in the sheet just in the beginning of the drawing. In the deep drawing, usually the clearance between punch and die is kept around 1.2 times of the sheet thickness. If clearance is small, it leads to ironing and if clearance is large, then it results in improper geometry of the drawn cup, therefore sufficient clearance is very necessary for properly drawing the desired cup. Figure 4.3 shows the punch, die, and blank holder setup; while their dimensions are shown in Figure 4.4.

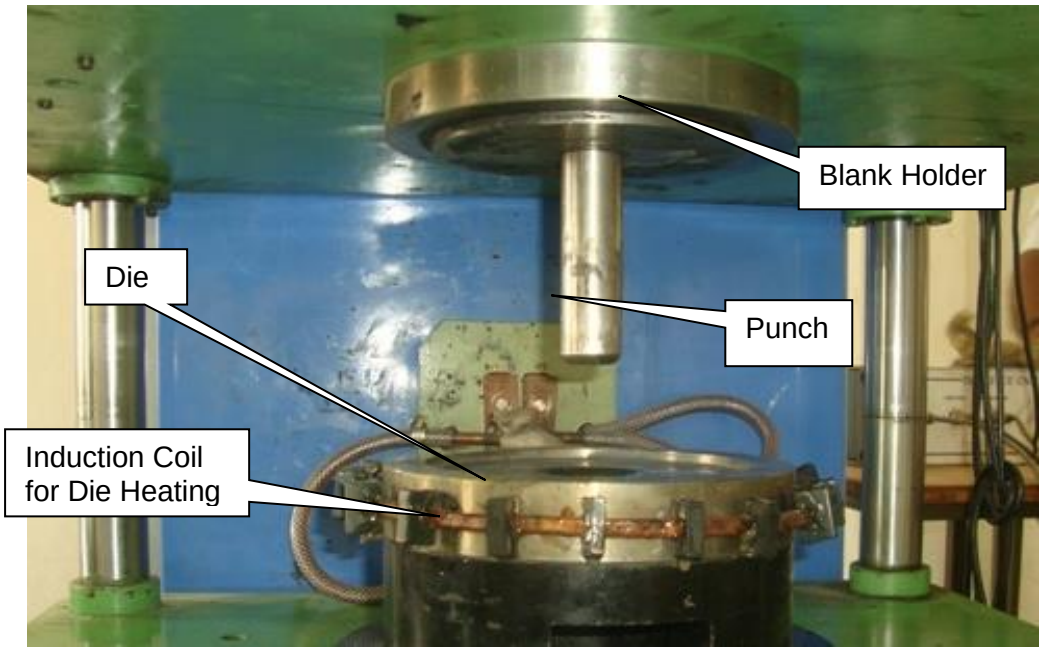

Figure 4.3: Punch, die and blank holder setup

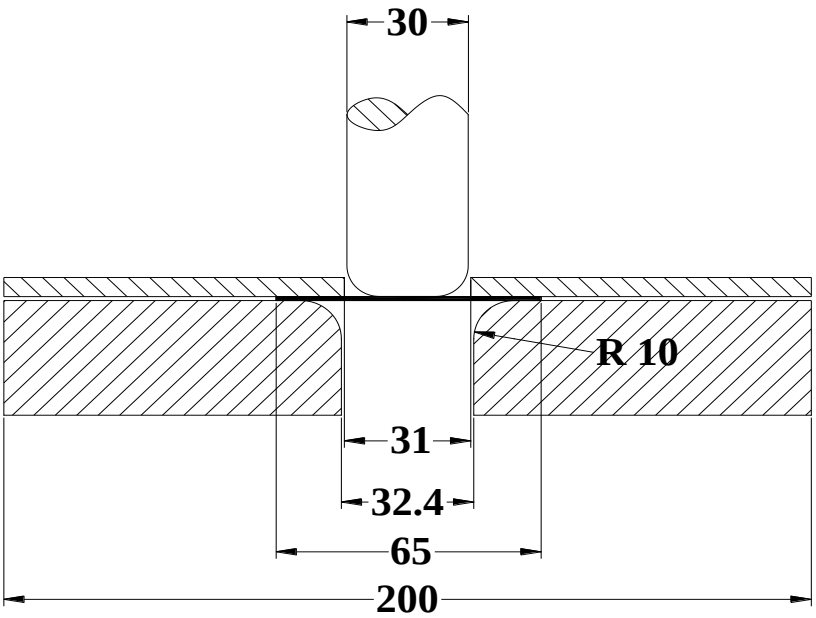

Figure 4.4: Tooling geometry and dimensions of deep drawing

One major factor in deep drawing is the die corner radius and punch corner radius. Sharp corners on the punch and die cause it to cut the sheet. A radius of curvature on the edge is necessary to change the force distribution and cause the metal to flow over the curvature into the die cavity. Considering this, the radius of curvature to the punch corner is kept 4 to 5 times of the sheet thickness; while the radius of curvature to the die corner is given as 8 to 10 times of the sheet thickness. Though the thickness of the initial blank is constant, in the drawn cup there are variations in thickness in certain areas. In order to form the side walls of the cup, the material must flow from the blank's peripheral, over the die corner radius in the direction of the punch. Material in the cup wall undergoes tensile

stresses, which naturally causes it to become thin. This thinning is unavoidable. Maximum thinning occurs most likely on the side walls near the base of the punch. A correctly drawn cup may have up to 25% reduction in the thickness in this area.

Data acquisition system is provided to record the punch load and the punch displacement, which can be directly accessed from the computer for any data processing. The load cell transducer converts the applied force into the signal. The strain gauge measures the deformation because it changes the resistance of the wire. Finally the output of the transducer is converted to the force based on the established relationships. The load cell of the experimental setup with 20 ton capacity is shown in Figure 4.5.

Figure 4.5: Load cell of the data acquisition system

There are different types of pressure sensors. One is an absolute pressure sensor which measures absolute pressure using the vacuum as a reference point. Another is a gauge sensor which measures pressure with reference to the ambient atmospheric pressure. There are also differential pressure sensors which measure the pressure difference between two contacts. In this press, pressure transducer is used to measure absolute pressure of the blank holder. Figure 4.6 shows the pressure transducer in the experimental setup. Pressure transducer is a one way valve which adjusts the pressure on the blank holder as well as measures the blank holding pressure.

Figure 4.6: Pressure transducer to measure blank holding pressure

Figure 4.7: Encoder for punch movement data acquisition

The displacement encoder converts the linear movement of the punch into electrical signals, which is recorded in form of the digital data for the punch movement. Figure 4.7 shows the rotary encoder in the system, which is connected through a mechanism with the punch.

The output signals from the load cell and punch displacement encoder-are connected to interface the unit as shown in Figure 4.8. This in turn gets connected to a computer. The use of the comprehensive range of functions in the user-friendly software helps to record, monitor and analyze the experiment data. The software is equipped to transform the raw data instantly into desired graphs and tables and then easily export them.

Figure 4.8: Interface unit of data acquisition system

The deep drawing experiments have been performed on 1 mm thick sheet metal specimens of ASS 316. The die has been held stationary, while the punch and blank holder have been moved by the two hydraulic actuators. The maximum blank holding pressure has been kept to 20 bar and the punch velocity has been kept to 10 mm/min. The cups have been drawn from the different diameter blanks at room temperature. The primary purpose here is to assess the formability by determining the LDR and thickness distribution in the drawn cups. Figure 4.9 shows the various cups drawn at room temperature, where the size of the initial blank is indicated above the cup figure.

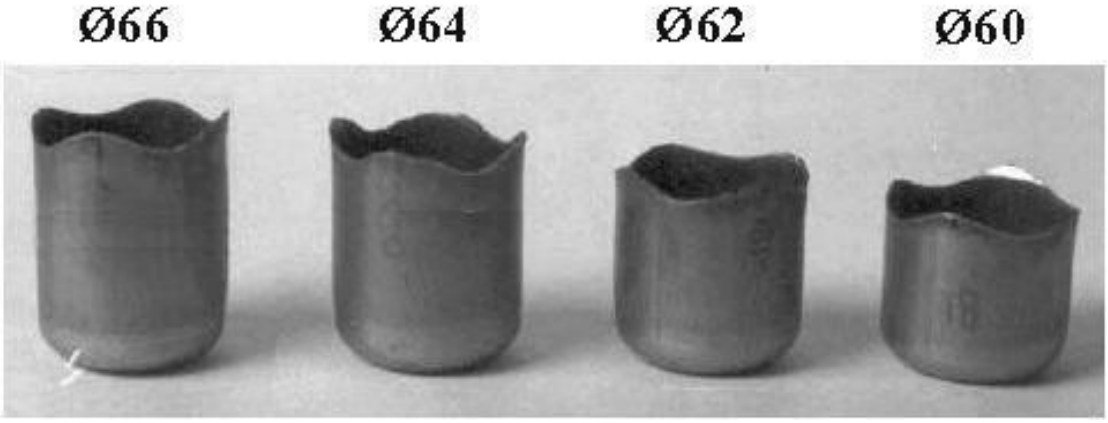

Figure 4.9: Experimentally drawn cups at room temperature from different sizes of the blanks

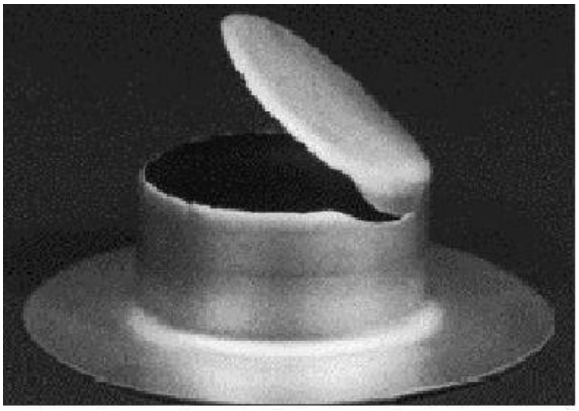

Figure 4.10: Fracture in experimentally drawn cup at room temperature from 68 mm diameter blank

At room temperature, maximum of 66 mm diameter blanks have been deep drawn properly without fracture. The next higher size blank with 68 mm diameter has been found to have fractured at punch corner as shown in Figure 4.10. Drawn cups were cut at the center and the thickness of the drawn cups has been measured at a distance of 1 mm from the center of the cup to the top of the wall. The thickness of the drawn cup has been found non-uniform from the

cup-center to the wall-top; it varied as the sheet has undergone bending and unbending at corners of the punch and die.

Thickness distribution of the cup along the cross section is shown in Figure 4.11. Thickness of the drawn cup changes at different locations. The portion near the center of the cup and beneath the punch has been deformed more, but almost uniformly under biaxial tensile forces. The thickness of the cup gradually increases as the distance from the center increases in the wall region. The punch radius being 15 mm, at the punch corner location, thickness of the cup has high reduction. Here, the sheet metal has undergone bending by wrapping around the punch corner, while the portion just beyond this location has undergone bending around the die corner. As the punch moves downward, unbending of the sheet takes place at the die walls. This bending and unbending caused higher deformation and straining in the sheet. Due to this high strain in cup wall, the sheet becomes thin at the punch corner. During deep drawing, the flange, the outer region of the blank tends to thicken, due to the compressive hoop stresses in the radial direction [83]. The cup thickness at the wall top has increased more than the initial blank thickness. With the increase in the blank diameter, the resistance to deformation in wall region increases and so a higher punch force is required to draw the cup. When the blank diameter is higher than LDR, this resistance force becomes very high and the cup wall can no longer withstand the applied load and so a fracture occurs at the punch corner.

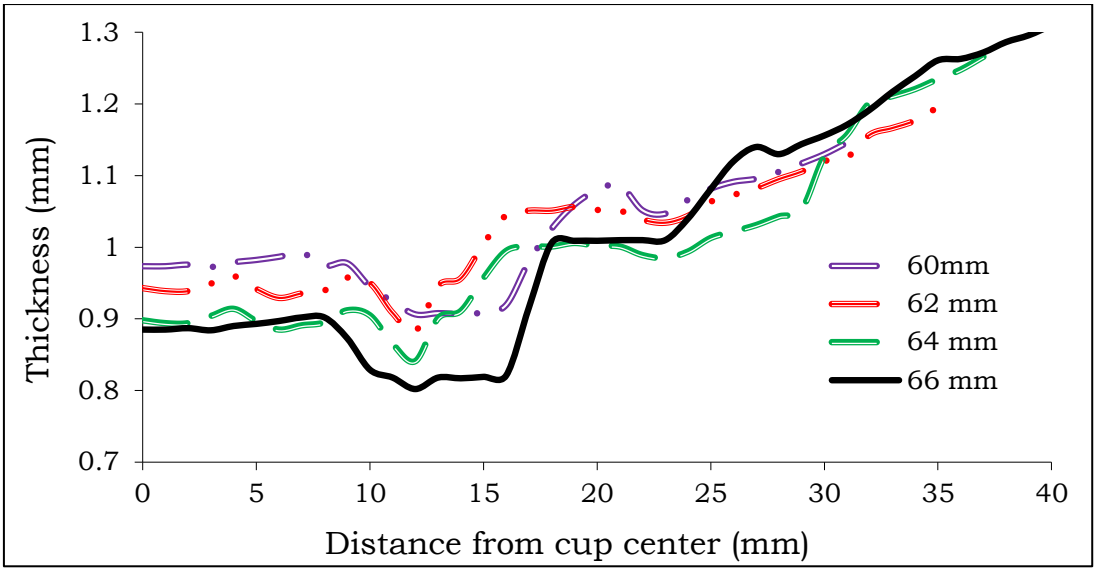

Figure 4.11: Thickness distribution of cups drawn at room temperature from different size of the blanks

At lower drawing ratio, the thickness reduction at punch corner location is less and as the drawing ratio increases this thickness reduction at punch corner increases. For example, for 60 mm blank the thickness at punch corner has reduced to 0.91 mm, while for 66 mm blank the thickness at punch corner has reduced to 0.83 mm. This is because a larger blank needs more force to draw and this force results in higher stresses and so higher deformation of the blank particularly at punch corner region. Figure 4.12 shows the force applied by the punch over the blank during deformation for the initial blanks of 64 mm and 66 mm diameters. The force needed to draw the 66 mm diameter blank is higher than the force for 64 mm blank. From these deep drawing experiments, it has been observed that at room temperature a maximum of 66 mm diameter blank can be safely deep drawn in to the cup of 30 mm diameter and thus getting the LDR of 2.2. Necking in the drawn cup has occurred near the punch corner.

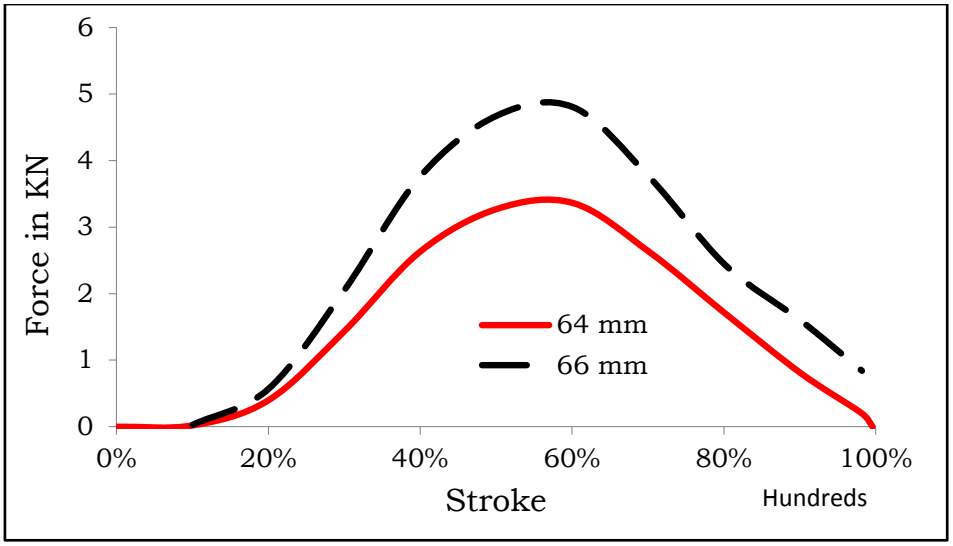

Figure 4.12: Punch force during experimental deep drawing at room temperature

4.3 Deep Drawing at Elevated Temperatures.

The experimental setup is also designed for deep drawing operations at elevated temperatures. The major purpose of this experimental setup is to determine the effectiveness of warm deep drawing over a range of temperatures. This is achieved by assessing the formability at different elevated temperatures

The schematic of the experimental setup for warm deep drawing is shown in Figure 4.13. Two sets of furnaces have been installed on a 20 ton hydraulic press – one is for heating the die and another for heating the blank. Die heating is required in order to avoid thermal shocks on the heated-up blank. Figure 4.14 shows the blank heating arrangement and Figure 4.15 shows the die heating arrangement with the induction coils surrounding the die. The temperatures are recorded by using a pyrometer, which is a non-contact type

temperature detecting instrument as shown in Figure 4.14. This works on the principle of capturing the wavelength of the radiation that is emitted by the material. A data acquisition system which is connected to the press obtains input parameters like punch travel, load and pressure by the press. These are fed to the computer where it directly plots outputs like a variation of load with displacement and force.

The die was heated and when it reached the required temperature, the lubricant was applied to the die so that the friction at the elevated temperature could be reduced. Molykote has been used as lubrication for reduction of friction between the die, blank and the punch assembly. It contains Molybdenum base material which is highly effective at elevated temperature. The blank was heated (as blank gets heated up quicker than the die, so the die is heated before the blank) and placed on the hot die. Then the punch was lowered and drawing operation was performed. The setup temperature was controlled and prevented from overheating by means of water circulation from the cooling tower.

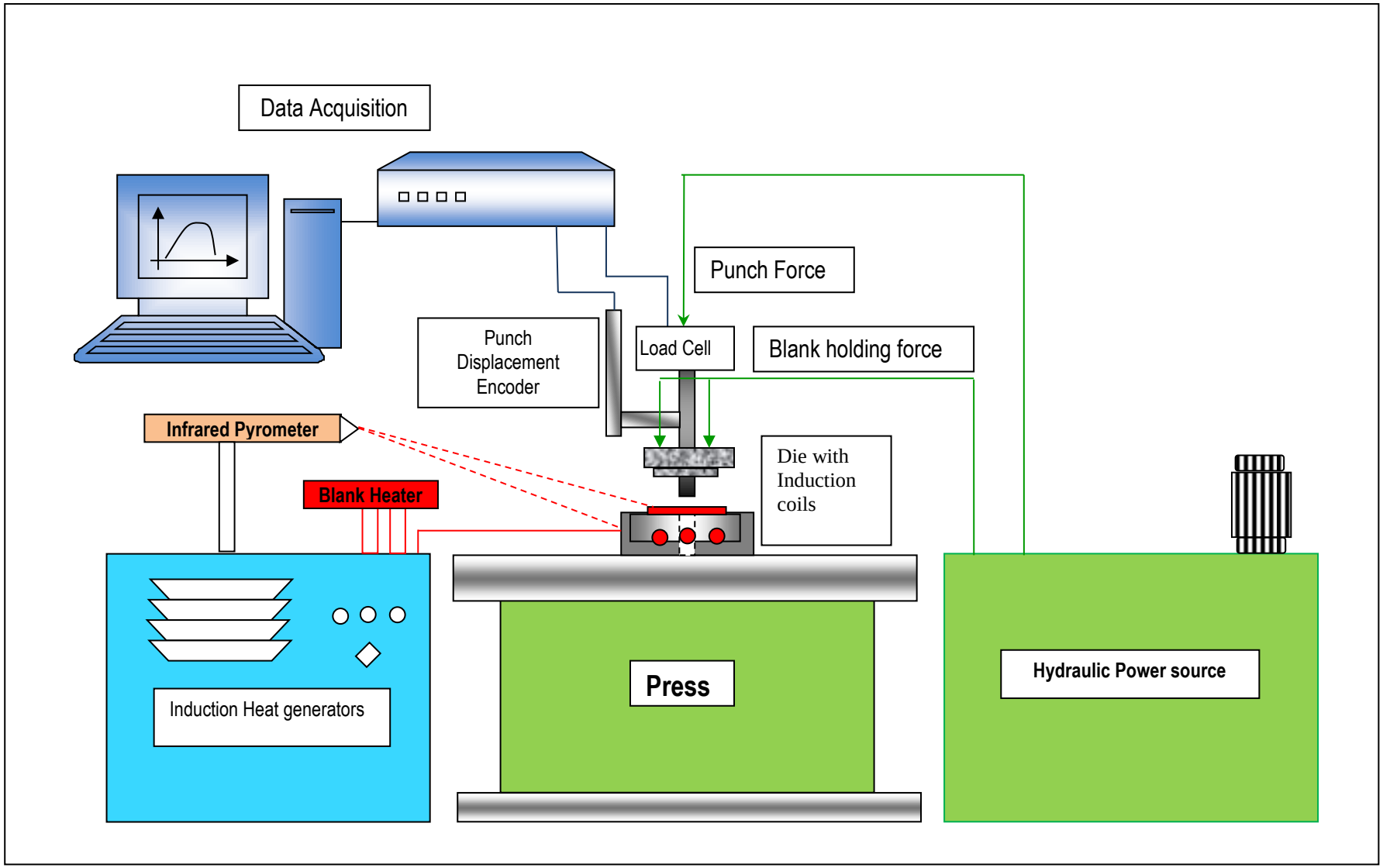

Figure 4.13: Schematic of the experimental setup for warm deep drawing

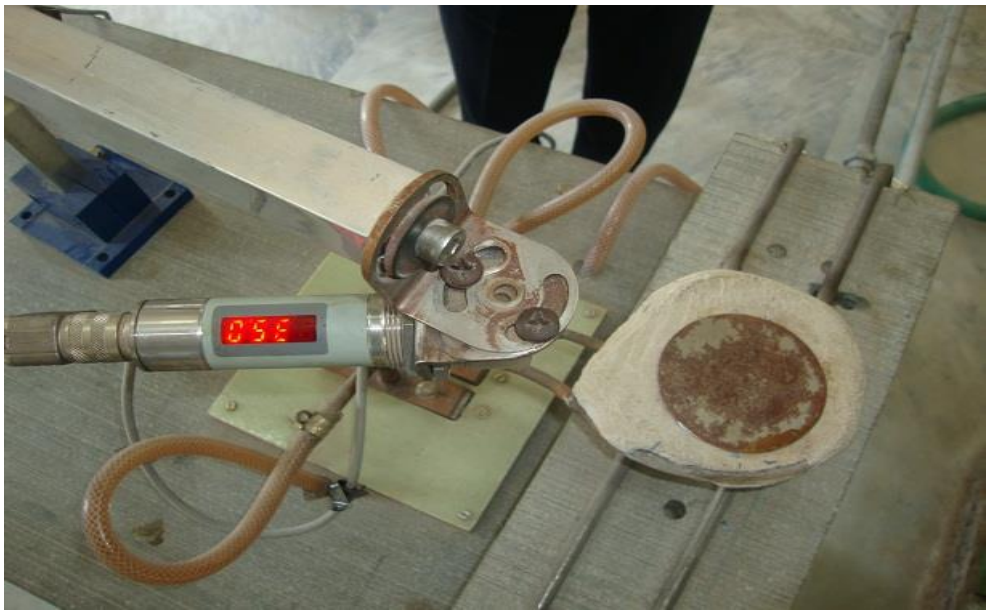

Figure 4.14: Blank heating arrangement with temperature measurement

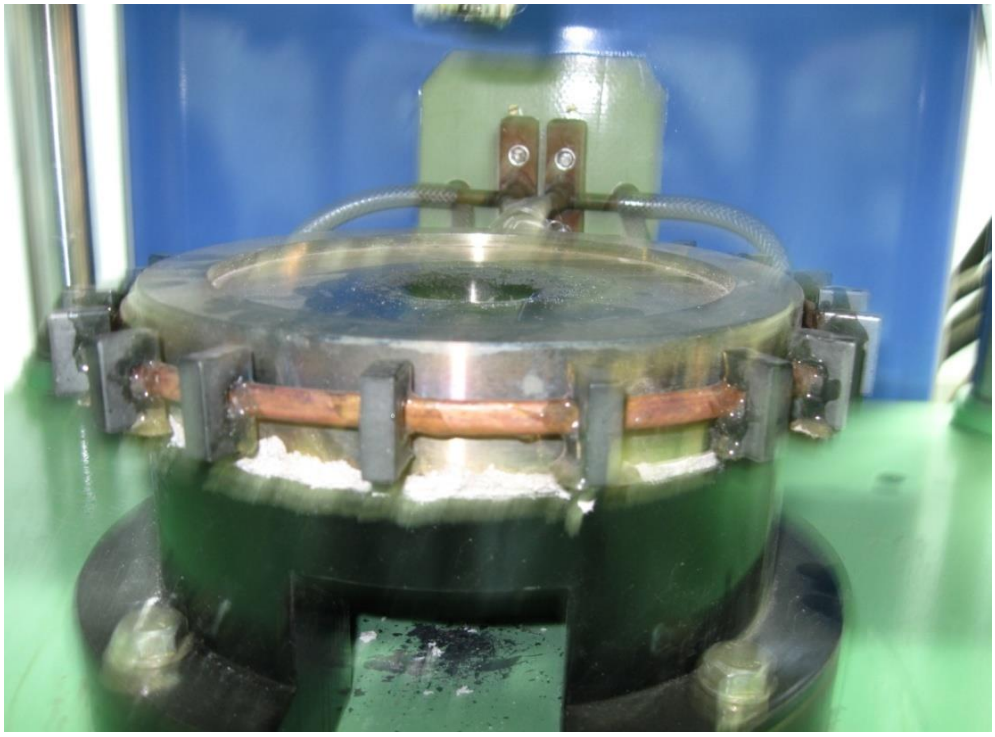

Figure 4.15: Die heating arrangement with induction coils around the die

Due to the furnace capacity, the experimental setup has the limitation on the temperature to which die can be heated up. It can reach to a maximum of 400°C. Therefore, the warm deep drawing experiments have been performed at 150°C, 300°C and 400°C on the circular blanks of 1 mm thickness and different diameters in the increment of 2 mm from 68 mm diameter onwards. Various cups have been drawn from blank sizes in this range at these elevated temperatures and LDR has been evaluated experimentally. For thickness measurement, the cup was cut at the center into two halves and the thickness was measured at an interval of 1 mm from the base center to the top of the wall, using a digital micrometer. The study of thickness distribution enables to analyze the safe blank thickness, at elevated temperature, that can be drawn without fracture.

4.3.1 Warm Deep Drawing at 150˚ C

Figure 4.16 shows the cups drawn from the different diameter blanks at 150°C. At this temperature, maximum of 70 mm diameter blank has been safely deep drawn and the next higher size blank has been found to have fractured at punch corner. At 150°C temperature, the LDR is evaluated as 2.33, which is better than the LDR of 2.2 at room temperature. The thickness of the cup has been measured at a distance of 1 mm from the center after cutting the drawn cup in the center. Thickness Distribution of the cup vs. the distance from the center is shown in Figure 4.17. Thickness reduction is found more in the higher size blanks. Figure 4.18 shows punch force vs. stroke diagram in deep drawing 68 mm and 70 mm blanks at 150˚C.

Figure 4.16: Experimentally drawn cups at 150°C from different size blanks

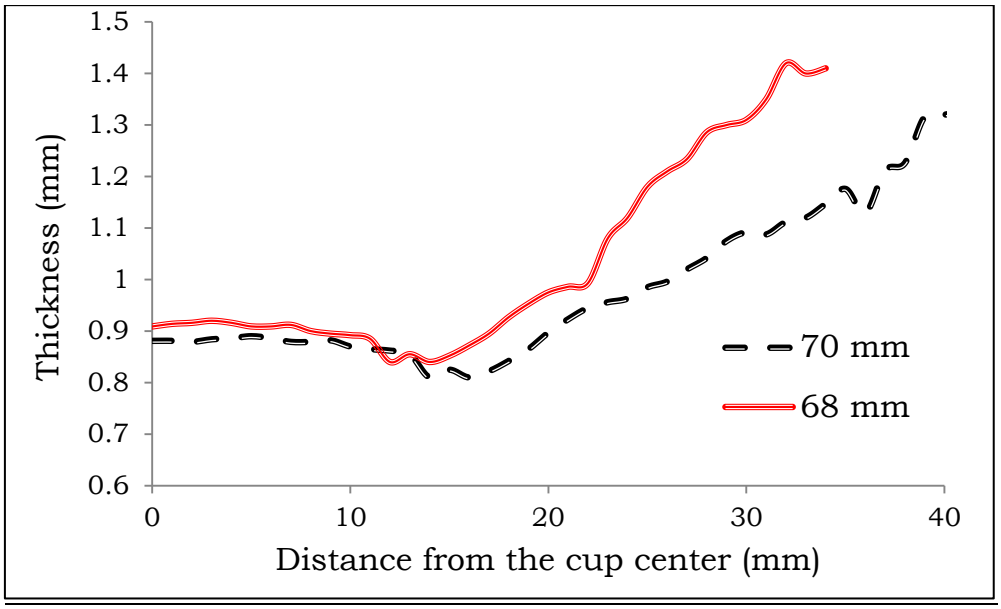

Figure 4.17: Thickness distribution in cups drawn at 150°C from different size blanks

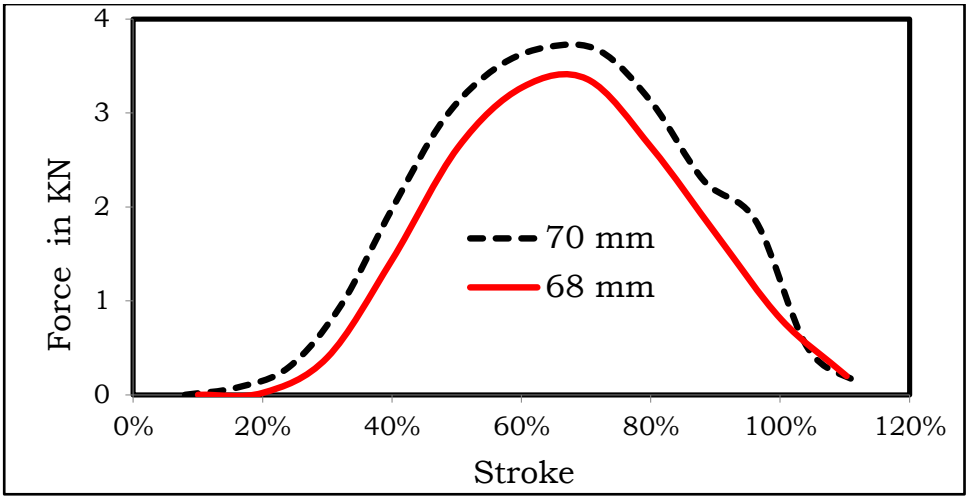

Figure 4.18: Punch force in deep drawing at 150°C for different size blanks

4.3.2 Warm Deep Drawing at 300˚ C

Figure 4.19 shows the different cups drawn from different diameter blanks at 300°C. Here, a maximum of 74 mm diameter blank has been safely deep drawn, resulting in an increased LDR of 2.47 at 300°C. Thickness distribution of cup along the radial line from the cup center is shown in Figure 4.20. Although the thickness reduction is more in the higher size diameter blank, but it is more uniform. Punch load to draw the cup gets increased with the increase in blank size even at this temperature as shown in Figure 4.21.

Figure 4.19: Experimentally drawn cups at 300°C from different size blanks

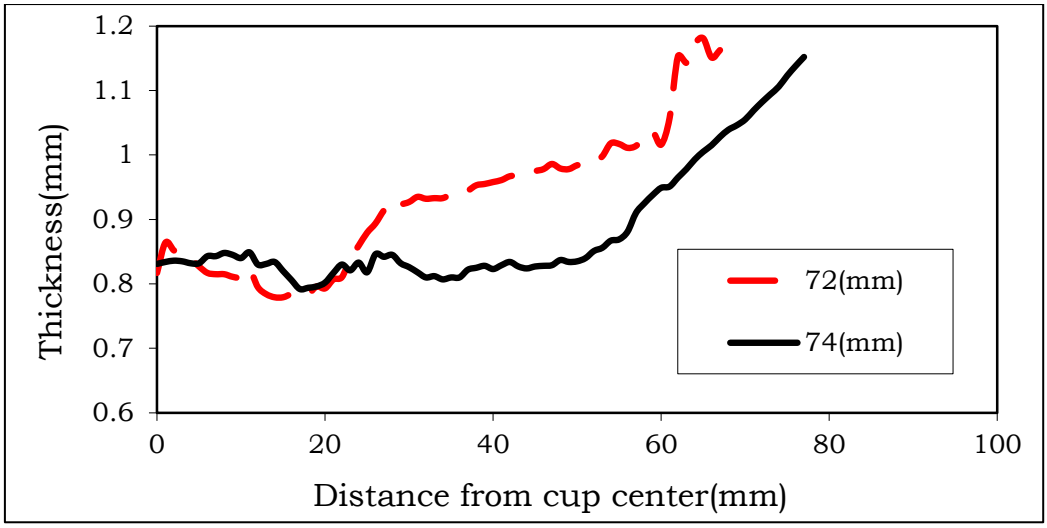

Figure 4.20: Thickness distribution of cups drawn at 300°C from different size of the blanks

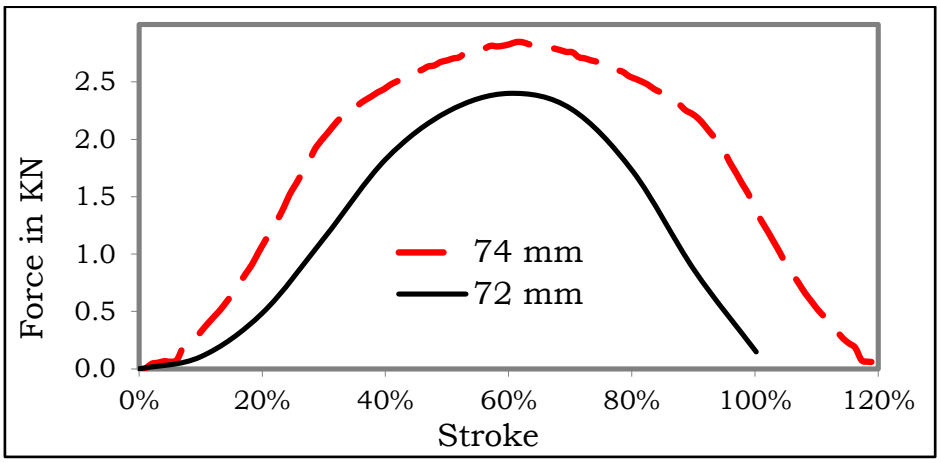

Figure 4.21: Punch force during deep drawing at 300°C from different size of the blanks

4.3.3 Warm Deep Drawing at 400˚ C

Figure 4.22 shows various cups drawn from the different diameter blanks at 400˚C. Here, 74 mm blank did not deep draw safely, rather it gets fractured. At this temperature, a maximum of 72 mm diameter blank can be properly deep drawn. This indicates that the material becomes more hard and brittle at 400˚C than compared to material at 300˚C, which might be due to the DSA phenomena occurring in the material. It had been investigated in

the previous chapter that at 400°C ASS 316 goes through DSA phenomena. In this region, LDR has been found to have decreased to 2.40.

Thickness distribution of the cup along the radial line from the cup center is shown in Figure 4.23. Here, two cups of same size blanks are shown. One curve is for the drawn cup from 72 mm blanks at 300°C of the non DSA region, another cup is 400°C in DSA region. In DSA region thickness reduction is similar to the non DSA temperature region, but thickness variation is more in DSA region. In non-DSA region thickness is more uniform and forms a good quality cup. The force required to draw the cup gets increased in DSA region as shown in Figure 4.24. This shows that in DSA region the formability of the material decreases.

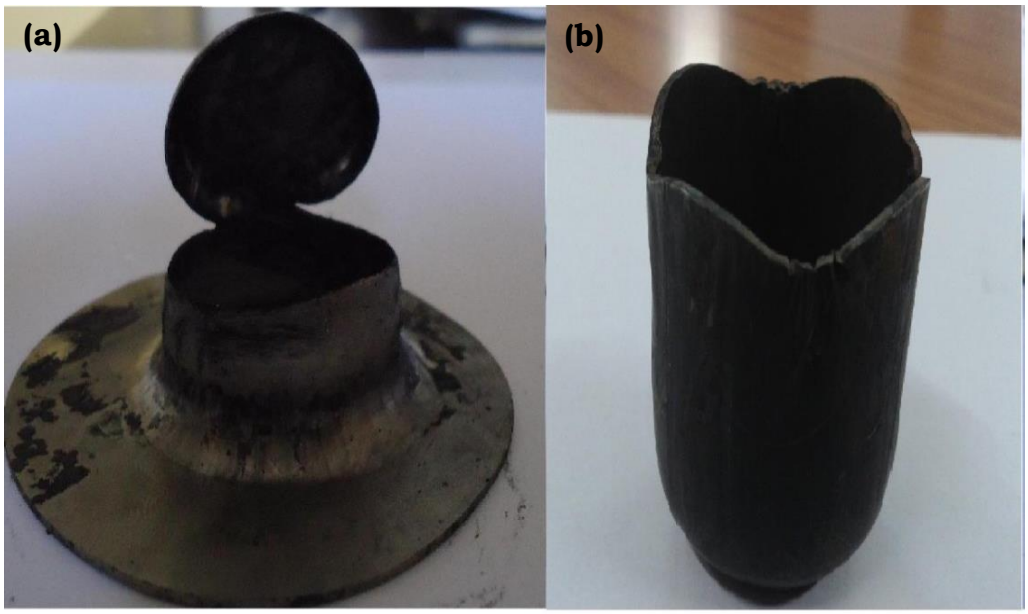

Figure 4.22: Experimentally drawn cups at 400°C in the DSA region from (a) 74 mm blank (b) 72 mm blank

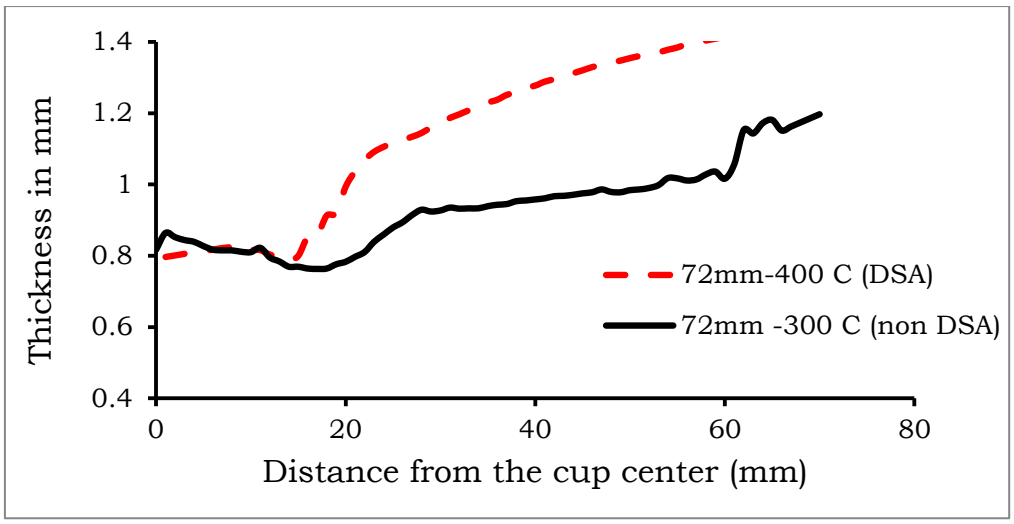

Figure 4.23: Thickness distribution of cups drawn from 72 mm blank

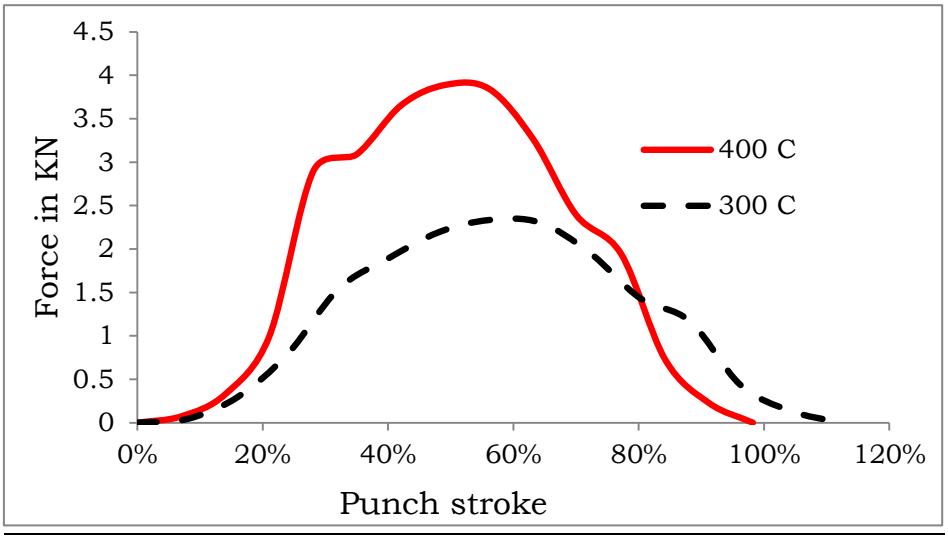

Figure 4.24: Punch force during deep drawing of 72 mm blank at different temperatures

At the higher temperatures, bigger size blanks can be deep drawn without fracture. Maximum of 70 mm diameter blank can be deep drawn safely at 150°C and with further increase in temperature to 300°C, maximum of 74 mm blank can be safely deep drawn. The LDR of 2.2 at room temperature gets increased to 2.33 at the temperature of 150°C, and further increased to 2.47 at 300°C. Sheet thickness is important, particularly in

components subject to different forces and temperatures. High thickness variations result in the poor quality cup. In warm forming at higher temperatures, although the cup thickness reduces more, but it becomes more uniform. With these experiments, it has been observed that as the temperature increases within non-DSA region, the formability of the material increases, whereas with further increase in temperature in DSA region the formability of the material significantly reduces.

Figure 4.25 shows the punch force vs displacement curve for the blanks drawn at different temperatures at LDR. It shows that the force required to draw the cup is decreased by increasing the temperature in non-DSA region. At room temperature 4.2 KN was applied to draw the cup at LDR, whereas it was decreased to 3.6 KN at 150°C and 2.7 KN at 300°C for the respective LDR. At 400˚C force was increased to 3.8 KN due to the DSA phenomena. Strength of the material decreases at the higher temperatures, but as the temperature enters in to DSA region, the material becomes stronger. It has also been observed that punch stroke length was increased by increase in the LDR and results in deeper cups. In DSA region LDR has been decreased and stroke length, depth of cup also decreased. Material becomes more formable at higher temperature in non-DSA region, while the formability decreases in DSA region.

Figure 4.26 shows the thickness of the drawn cup at different temperatures at their corresponding LDR. It has been observed that at lower temperature, thickness reduction is less, but variation in thickness is more, but at higher temperature below DSA region thickness reduction is more, but

it is more uniform, whereas DSA has a negative effect. At higher temperature material has been stretched due to higher formability which results in more uniform thickness of the cup. All these experiments reveal that ASS 316 has highest LDR of 2.47 and cups have uniform thickness at 300°C, which results in the best quality cups.

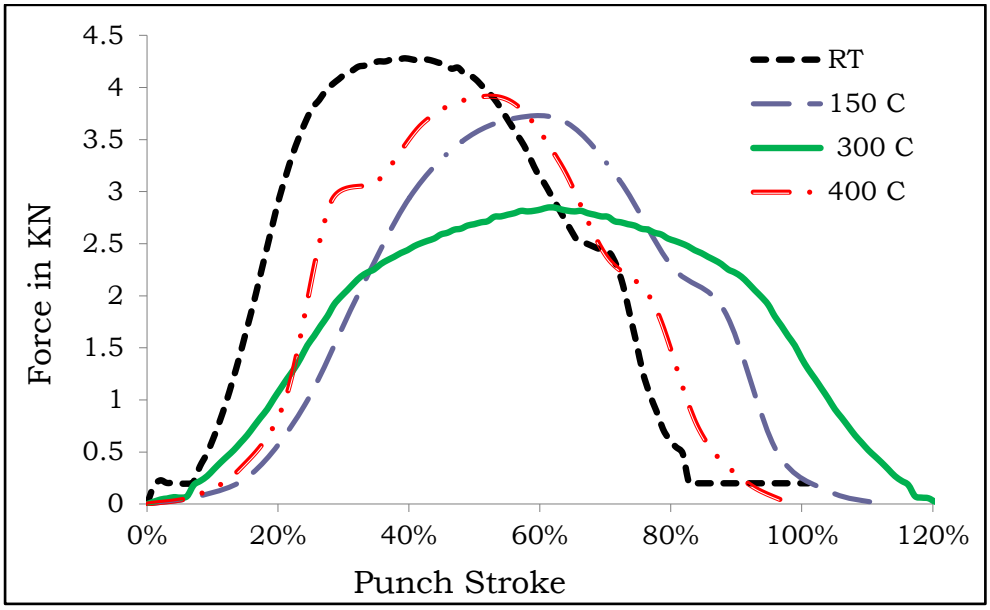

Figure 4.25: Punch force during deep drawing at the different temperature at their corresponding LDR

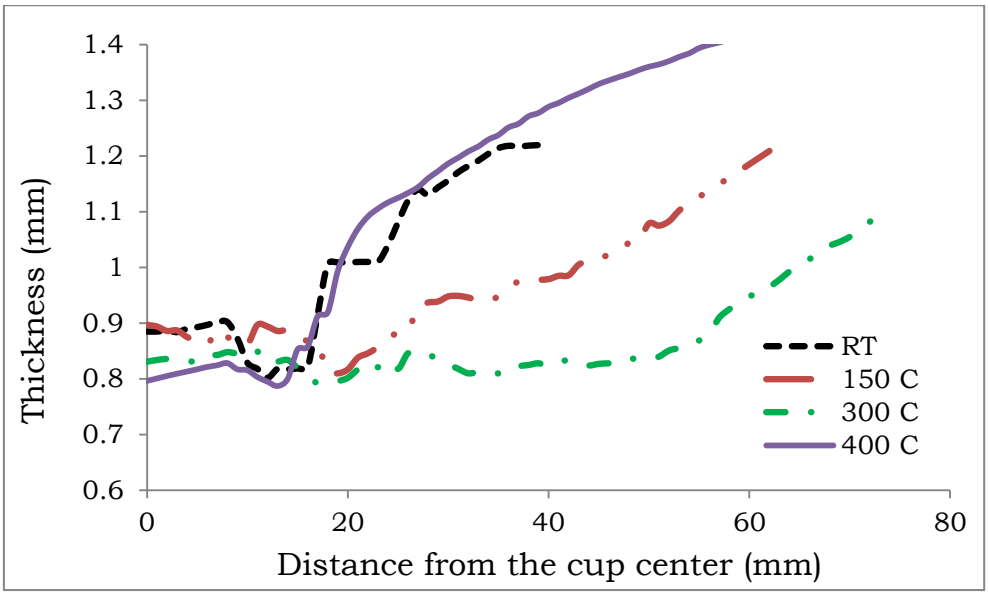

Figure 4.26: Thickness distribution of the cup at different temperature at their corresponding LDR

4.4 Effect of Process Parameters on Deep Drawing

Process parameters of deep drawing like blank holding pressure, speed of the punch, radius of curvature of the die and punch influence the drawability of the sheet besides temperature. In this research, two important parameters, Blank Holding Pressure (BHP) and speed of the punch have been studied to understand their effect on the sheet metal formability. Blank holding pressure has been controlled by the fluid flow in the hydraulic press and speed has been controlled by the electric signals to the punch.

Initially punch speed has been maintained constant and BHP has been varied. In deep drawing, BHP is taken up to 2% of the yield stress. The material in the investigation, ASS 316, has yield strength of 1820 bar. So different values of BHP have been taken as 10 bar, 15 bar, 20 bar and 25 bar at constant speed of 10 mm/min. All the drawn cups at this different BHP are shown in Figure 4.27.

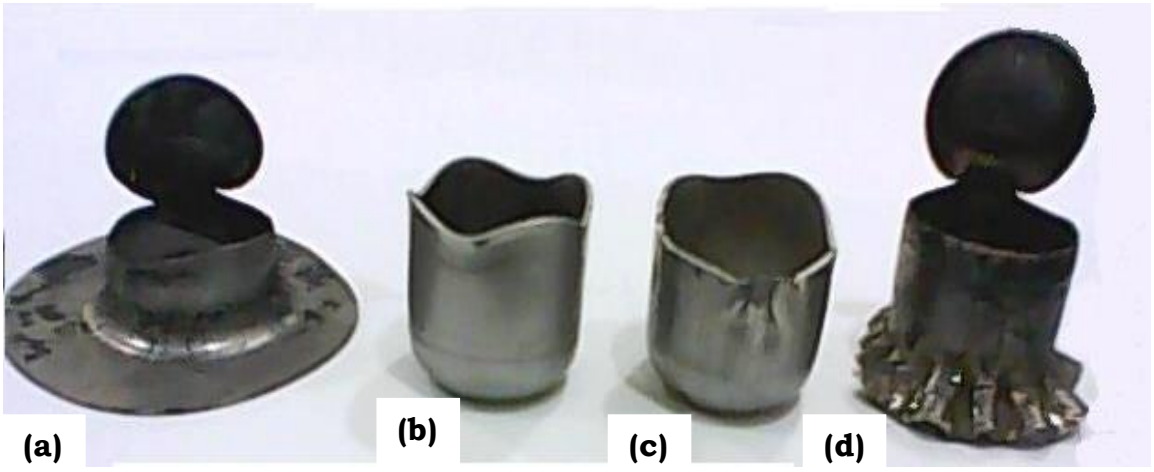

Figure 4.27: Drawn cups at different BHP in bar (a) 25 (b) 20 (c) 15 (d) 10

Blanks have been drawn well under 15, 20 bar blank holding pressure, but these have been fractured at 10, 25 bar pressure. Very low BHP of 10 bar results in the severe wrinkle in the flange portion which prevented the material from going through the die and the punch clearance and this leads to tearing in the cup bottom while passing into the die. Severe wrinkles are observed on the flange of the cup, which shows an insufficient BHP. Whereas 25 bar presser holds the blank and does not allow the material to flow into the die which results in fracture at punch corner. In this cup very flat and smooth flange is observed, which shows the BHP is higher. By application of higher or lower blank holding pressure, cup is fractured. At intermediate pressure of 15 and 20 bar, cups have been drawn. At 15 bar, the cup has been drawn safely, but the cup edges are not smooth as slight wrinkles have been observed on the cup walls. It shows that BHP is sufficient to draw the cup but not able to compensate the radial compressive hoop stresses. At 20 bar BHP cup has been drawn to a good shape without any wrinkles, which shows the pressure is sufficient to hold the compressive hoop stresses. For the ASS 316 at room temperature, 20 bar is the best blank holding pressure.

Further effect of punch speed has been investigated on the cup formability by keeping the blank holding pressure constant at 20 bar and changing the speed of the punch. Punch speed has been varied at three different speeds 18, 12, 6 mm/min. Cups have been drawn at these speeds and are shown in Figure 4.28. It has been observed that cups can draw at all speeds, but with different heights. At 18 mm/min speed, the cup height is less and it has been increased with a decrease in the punch speed, without

any wrinkles on the cup wall. Height shows the drawability of the blank. At the speed of 6 mm/min, the material has a better drawability.

Formability of ASS 316 has been studied by the experiments of deep drawing at different temperatures. It has been observed that ASS 316 has very good formability. Under warm forming, drawability of the sheet increases up to 300°C and beyond that not much improvement has been observed. In DSA region, at 400°C, the formability decreased significantly. Process parameters like speed of the punch and blank holding force also influence the deep drawing. The hydraulic press setup has a limitation to conduct experiments at further higher temperatures, so numerical analysis is performed using LS-Dyna with experimental validations. These validated models have been simulated at higher temperatures for the further formability studies.

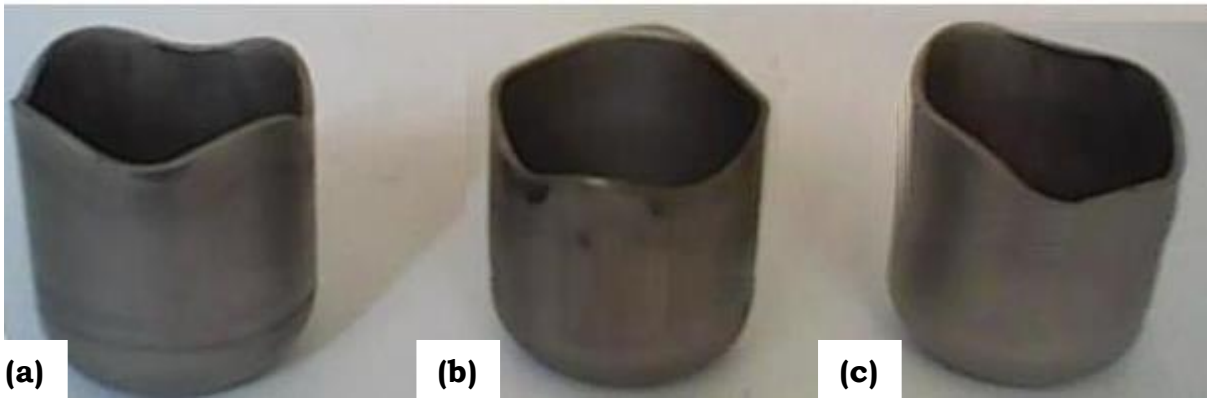

Figure 4.28: Drawn cups with various punch speeds (mm/min)
(a) 6 (b) 12 (c) 18

CHAPTER 5:

Numerical Analysis of Deep Drawing

Generally, in any operation large amount of time is consumed in trial and error method, and this trial and error method involves a lot of expenditure and loss of valuable time. Also experimentations have limitations of materials and tools at higher temperature. To overcome this problem, process modeling by computer simulation called Finite Element Methods (FEM) has been introduced, which simulates the actual process and thus saves time and money. This chapter focuses on the simulations of deep drawing process for ASS 316 at elevated temperatures. A Finite Element model has been developed for preliminary investigations. LS-Dyna has been used for simulations of deep drawing. Properties of materials which were evaluated by tensile tests have been used as input for the model. Actual conditions have been simulated and analyzed for the response of the model during deep drawing at different temperatures. Thickness and LDR of the drawn cups are predicted accurately. Simulated results have been validated with the experimental findings.

5.1 Finite Element Methods

FEM are computerized methods for predicting the reactions of real object to applied force, heat, vibration. These techniques are used to evaluate the behavior of work piece, equipment and structures for various loading conditions, and temperatures. In this method simpler interlocking finite elements are amenable to mathematical analysis. The analysis of the whole structure is obtained by simultaneous analysis of the individual elements, having due regard to their individual positions within the mesh.

FEM has been extensively used in forming operations to optimize various process variables in order to produce defect free parts. FEM of metal forming processes has now gained the industrial stage, and it has become possible to simulate the metal deformation and calculate stress and strain states for complex processes. This simulates the actual process for preliminary design and help to predict errors, suggest modification to be done at an early stage before the parts are fabricated. Therefore, FEM with sophisticated numerical simulations are gradually replacing manual trial-and-error design iterations. FEM in designing process (especially in pre-processing analysis stage) greatly enhances the efficiency and saving of time and manpower.

The Dyna-form with LS-Dyna solver with coupled thermal analysis is extensively used for simulation of metal forming at different temperatures. Various codes have been developed for different conditions and applications such as sheet metal forming, automobile crashworthiness, occupant safety and underwater explosions. It is a non-linear dynamic simulation package, which can simulate different types of sheet metal processes like deep drawing, stretching, bending, hydroforming, stamping, etc. to predict stresses, strains, thickness distribution, etc. It also studies the effects of various design parameters of tooling on the final product. Various material models have been incorporated in it to simulate the material behavior accurately in different conditions.

5.2 Material Models

Sheet metals are most susceptible to failure under different strain conditions. Several material models for finite element codes for sheet metal forming analysis have been developed in LS-Dyna software [84]. The work piece material used in deep drawing process is anisotropic, due to the directionality of plastic properties gained by rolling and other primary working processes. Hill's quadratic yield function was the first attempt to model the anisotropy of orthotropic sheets [85]. This criterion is simple to implement but possesses some drawbacks. The anomaly of this criterion is the relation between the uniaxial yield stress in the rolling direction, the yield stress in the balanced biaxial test, and the average strain rate ratio predicted from this criterion is not satisfied by some alloys. Quite a few other anisotropic yield functions have been proposed for orthotropic materials, which do not possess these drawbacks. Hill's 1979 yield function [86] is free of the anomaly, but does not contain the shear stress terms.

The yield functions proposed by Ferron et al. [87] are applicable only for the case of plane stress state. This yield function contains fourth degree terms in stress components. Ferron's yield function uses the polar coordinate representation of the yield surface in the principal stress space. Strain rate potentials have also been proposed to incorporate anisotropy in metal forming analysis. Lately, anisotropic yield functions have been developed by applying an appropriate tensor transformation to an isotropic yield function by Barlat [88]. For a general transformation, it is usually difficult to satisfy

the convexity condition. Therefore, mostly linear transformations have been used [89].

The transition from the elastic to the plastic state occurs when the stress reaches the yield point of the material. The yield point in uniaxial tension is established using the stress-strain curve of the material whereby a convention is necessary in order to define it. Plastic behavior of a material is described in a general stress state, where the elements need a yield criterion to express a relationship between the stress components at the moment when plastic 'yielding' occurs and a hardening rule to describe the material flow during the forming process.

The expression of the yield function is established on the basis of the transition from the elastic to the plastic state. The most widely used yield criteria have been proposed by von-Mises for isotropic materials. Barlat and Richmond proposed a more general form of yield criterion for anisotropic materials by expressing the properties in three mutually perpendicular directions in x, y, z of a coordinate system.

Barlat and Lian [90] applied a linear transformation to modify Hosford [91] yield function to develop an anisotropic yield function for the plane stress conditions. Later on, Barlat [92] and Karafillis and Boyce [93] extended this technique to the three dimensional state of stress. These three-dimensional anisotropic yield functions were not able to capture the full anisotropy of metal sheets. Therefore, Barlat and his coworkers introduced

two linear transformations first for the plane stress case and then later, for the three dimensional case [94].

Most of the above anisotropic yield functions have been used in finite element models to numerically simulate anisotropy in sheet metal forming processes. The deep drawing process is one such sheet forming operation on which several researchers have tried these yield functions.

Yoon et al. [95] implemented Barlat's 3-D anisotropic yield function with two linear transformations in LS-Dyna and MSC.MARC using 3-D solid elements to demonstrate its capability to simulate anisotropic profile of circular cup drawing for a fictitious material. Yoon et al. [96] also conducted experiments to measure the anisotropic profile in 2090-T3 aluminium alloy and reported good agreement between the predicted and measured results.

5.2.1 Yield Model

Barlat's material model is one of the popular yield model and available in LS-Dyna. This is used as the yield model in this research. This model was developed by Barlat and Lege [97] for modeling sheets with anisotropic materials under different stress conditions. This material model allows the use of the Lankford parameters (*R)* for the definition of the anisotropy. The effective plastic strain used in this model is defined to be plastic work equivalent. This is defined as a function of effective plastic strain in the rolling direction. In this model stresses and the relative volume change are used as the functions of strain in uniaxial tension in the rolling direction. Load curve is given as a function of strain in the rolling direction and Young's modulus.

Curves are also defined as the function of plastic strain in 45° and 90° directions to rolling. The hardening curves are defined from the measured stress as a function of measured plastic strain in uniaxial tension in the corresponding direction, i.e., as determined from experimental test using a standard procedure. Moreover, the curves define the *R* values as the function of the measured plastic strain in uniaxial tension in the direction of interest. These curves are transformed internally to use with effective stress and strain properties in the actual model. The effective plastic strain does not coincide with the plastic strain components in other directions than the rolling direction.

The anisotropic yield criterion Φ for plane stress is defined as [84]:

$$\Phi = a|K_1 + K_2|^m + a|K_1 - K_2|^m + c|2K_2|^m \tag{5.1}$$

where

$$K_1 = \frac{\sigma_x + h\sigma_y}{2}; \qquad K_2 = \sqrt{\left(\frac{\sigma_x - h\sigma_y}{2}\right) + p^2\tau_{xy}^2} \tag{5.2}$$

The anisotropic material constants *a, c,* and *h* are obtained through R_0, R_{45}, and R_{90} (*R* values in that direction to rolling):

$$a = 2 - 2\sqrt{\frac{R_{00}}{1+R_{00}}\frac{R_{90}}{1+R_{90}}}, \qquad c = 2 - a, \qquad h = \sqrt{\left(\frac{R_{00}}{1+R_{00}}\frac{1+R_{90}}{R_{90}}\right)} \tag{5.3}$$

The anisotropy parameter *p* is calculated implicitly. According to Barlat and Lian, the *R* value for any angle φ can be calculated from:

$$R_\emptyset = \frac{2m\sigma_y^m}{\left(\frac{\partial\Phi}{\partial\sigma_x} + \frac{\partial\Phi}{\partial\sigma_y}\right)\sigma_\emptyset} - 1 \tag{5.4}$$

where σ_φ is the strength in uniaxial tension, at the direction φ. This expression can be used to iteratively calculate the value. Let φ =45 and define a function *g* as

$$g\,(p) = \frac{2m\sigma_y^m}{(\frac{\partial \Phi}{\partial \sigma_x} + \frac{\partial \Phi}{\partial \sigma_y})\sigma_\emptyset} - 1 - R_{45} \tag{5.5}$$

For the face centered cubic (FCC) materials m=8 is recommended and for body centered cubic (BCC) materials m=6 may be used. The yield strength of the material can be expressed in terms of k and n.

$$\sigma_y = k\,\varepsilon^n = k\,(\varepsilon_{yp} + \bar{\varepsilon_p})^n \tag{5.6}$$

where ε_{yp} is the elastic strain to yield and $\bar{\varepsilon_p}$ is the effective plastic strain (logarithmic). If σ_Y is set to zero, the strain to yield is found by solving for the intersection of the linearly elastic loading equation with the strain hardening equation

$$\sigma = E\varepsilon \qquad \text{and} \qquad \sigma = k\,\varepsilon^n \tag{5.7}$$

which gives the elastic strain at yield as:

$$\varepsilon_{yp} = \left(\frac{E}{k}\right)^{[\frac{1}{n-1}]} \tag{5.8}$$

If yield is nonzero and greater than 0.02 then:

$$\varepsilon_{yp} = \left(\frac{\sigma_y}{k}\right)^{[\frac{1}{n}]} \tag{5.9}$$

5.2.2 Hardening model

The available hardening models with Barlat's in LS-Dyna is the Gosh equation given by

$$\sigma_y(\varepsilon_p) = k\,(\varepsilon_0 + \varepsilon_p)^n - p \tag{5.10}$$

For Gosh hardening law, the interpretation of the variable is the same, i.e., if set to zero, the strain at yield is determined implicitly from the intersection of the strain hardening equation with a linear elastic equation. It includes strain rate effects in the model, which multiply the yield stress by a factor, depending on the effective plastic strain rate. In the Cowper-Symonds' model the yield stress can be written.

$$\sigma_y\left(\varepsilon_p \dot{\varepsilon}_p\right) = \sigma_y^s\left(\varepsilon_p\right)\left\{1 + \left(\frac{\dot{\varepsilon_p}}{C}\right)^{1/p}\right\} \tag{5.11}$$

where σ_y^s denotes the static yield stress, C and p are material parameters and ε_p is the effective plastic strain rate [84].

Barlat's model with Gosh hardening law accurately predicts the material behavior during forming, but cannot simulate the DSA phenomena in the material. Among all models in LS Dyna, Mechanical Threshold Stress (MTS) model can effectively predict and simulate the dynamic strain aging behavior of the materials during forming [98]. For simplicity of implementation, MTS model can be used along with the default von-Mises yield criteria in LS Dyna.

The MTS model is one of the hardening models with LS-Dyna. It is the only model available which can simulate DSA phenomena. This model was developed by Follansbee [99]. It is a physical based model. It is considered that the flow stress at a certain temperature and strain rate do not increase above a saturation stress. MTS model has been proved effective in predicting the constitutive response of metals over a wide range of temperatures and strain rates. The model is based on dislocation dynamics and thermal activation theory. It describes a material's flow stress as a combination of

three components. The first one is rate independent interactions of dislocations with long-range barriers and an athermal stress (σ_a). Second is the rate and temperature dependent contribution due to intrinsic barriers, a thermal stress (σ_i) for the interaction of dislocations with interstitial obstacles. Third is a structure that evolves with plastic strain due to work hardening and dynamic recovery a threshold stress (σ_e) for the dislocation interaction. The parameters for the model are material specific and determined from the stress - strain response measured for a range of strain rates and temperature conditions.

The MTS model gives the following form for the flow stress 'σ':

$$\sigma_y\left(\epsilon_{p,}\dot{\epsilon},T\right) = \sigma_a + (S_i\sigma_i + S_e\sigma_e)\frac{\mu\,(p,T)}{\mu_0} \tag{5.12}$$

where σ_y is the flow stress, ε_p is the plastic strain, $\dot{\varepsilon}$ is the strain rate, T is the temperature, σ_a is the athermal component of mechanical threshold stress, μ_0 is the shear modulus at 0°K and ambient pressure, σ_i is the thermal stress due to barriers to thermally activated dislocation motion, σ_e is the threshold stress of the flow stress. The scaling factors S_i and S_e are temperature and strain rate dependent and take the Arrhenius form

$$S_i = [1 - (\frac{K_bT}{g_{0i}b^3\mu(p,T)}\,ln\frac{\dot{\epsilon_{0i}}}{\dot{\epsilon}})^{\frac{1}{q_i}}]^{\frac{1}{p_i}} \tag{5.13}$$

$$S_e = [1 - (\frac{K_bT}{g_{0e}b^3\mu(p,T)}\,ln\frac{\dot{\epsilon_{0e}}}{\dot{\epsilon}})^{\frac{1}{q_e}}]^{\frac{1}{p_e}} \tag{5.14}$$

where k_b is the Boltzmann constant, b is the magnitude of the Burgers' vector, (g_{0i}, g_{0e}) are normalized activation energies, ($\dot{\varepsilon}_{0i}$, $\dot{\varepsilon}_{0e}$) are constant reference strain rates, and (q_i, p_i, q_e, p_e) are the material constants. The strain

hardening component of the mechanical threshold stress (σ_e) is given by a modified Voce law.

$$\frac{d\sigma_e}{d\epsilon_p} = \theta(\sigma_e) \tag{5.15}$$

The experimental data which is used to determine the MTS model parameters are in the form of true stress versus true strain curve. These curves have been digitized manually with care and corrected for distortion. The elastic portion of the strain has been subtracted from the total strain by considering Young's modulus and true stress versus true plastic strain curves have been constructed. The first step in the determination of the parameters for the MTS models is the estimation of the athermal component of the stress (σ_a). This parameter is dependent on the Hall-Petch effect and hence on the characteristic of the phase and independent of the temperature.

$$\sigma_a = (\sigma_0 + C_1\epsilon_p^n + kd^{-1/2}) \tag{5.16}$$

From Equation 5.12, it can be seen that σ_i can be found if σ_y and σ_a are known and σ_e is zero. It has been assumed that σ_e is zero when the plastic strain is zero at yield point, and MTS equation can write the relation.

$$\left(\frac{\sigma_y - \sigma_a}{\mu}\right) = \left(\frac{\sigma_i}{\mu_0}\right)^{p_i} \left[1 - \left(\frac{1}{g_{0i}}\right)^{\frac{1}{q_i}} \left[\frac{k_b T}{\mu b^3} ln\left(\frac{\dot{\epsilon_{0i}}}{\dot{\epsilon}}\right)\right]^{1/q_i}\right. \tag{5.17}$$

Modified Arrhenius (Fisher) plots based on Equation 5.17 have been used to determine the normalized activation energy (g_{0i}) and the intrinsic thermally activated portion of the yield stress (σ_i). The shear modulus (μ) has been calculated using the NP shear modulus model. The yield stress at zero

plastic strain (σ_y) has been computed as the intersection of the stress-plastic strain curve with the stress axis. The value of the Boltzmann constant (k_b) is 1.3806503e^{-23} J/K and the magnitude of the Burgers' vector (b) is 2.48e^{-10} m for ASS 316. The density of the material also takes into consideration as 7.9x10^3 kg / m^3 for ASS 316. All the parameters of MTS model for ASS 316 are shown in Table 5.1.

Table 5.1: MTS parameters measured from ASS 316 tensile data

σ_a	σ_i	σ_e	g_{0i},	g_{0e}	p	q	$\dot{\varepsilon}_0$
50 MPa	572 MPa	248 MPa	1.7 J	0.2 J	0.66	1	1

5.3 Results of FE Analysis

The finite element analysis in the present work has been done using a commercially available code LS-Dyna version 971 solver at different temperatures. This is a general purpose finite element code for analyzing the large deformation, static and dynamic response of structures. The main solution methodology is based on explicit time integration. In this interface, this solution methodology can be rigidly tied to admit variable zoning without the need of the mesh transition region. Adaptive re-meshing is available for shell element and is widely used in sheet metal forming applications like deep drawing, stretching. It allows draw beads in metal forming applications to be easily modelled by defining the line of nodes along the draw bead. Varieties of element formulations are available for different element types.

Specialized capabilities for airbags, sensors and seatbelts have tailored for applications in different industries.

The input models have been created in Dynaform version 5.6.1. It is a powerful pre-processor, reduces the tryout time and costs that are associated with the tooling design and development cycle. It contains numerous automated functions to aid in even the most complex tool geometry. The complete LS-Dyna interface allows a comfortable configuration and analysis of complex deep drawing simulations. After the surface has been created, meshing has been generated on the surface of the tool components and the blank. The integrated mesh generator has been optimized for the meshing of farming tools and provides a fast and reliable mesh. Fine meshing has been generated in the blank to obtain accurate results. The blank have been meshed using Belytschko-Tsay shell elements as it takes less computational time, around 30–50% less than others [100].

The tool components have been considered as rigid bodies, so they have been meshed using solid elements. Material properties of ASS 316 have been given as input to the model, which have been measured and calculated at different temperatures as presented in Chapter 3. These properties have been shown in Tables 3.2 & 3.4. Friction in deep drawing under warm conditions can be reduced by using Molykote as lubricant, which is calculated by Singh et al [101] at varying temperatures. In this study for ASS 316 friction coefficient has been found by correlating the experimental results with simulated results at different friction coefficients. The BHP and punch speed have been taken similar to those used in the experiments,

which are shown in Table 5.2. Simulations have been repeated by changing the size of the blank and keeping the other parameters constant. The complete tooling model of the pre-processor is shown in Figure 5.1.

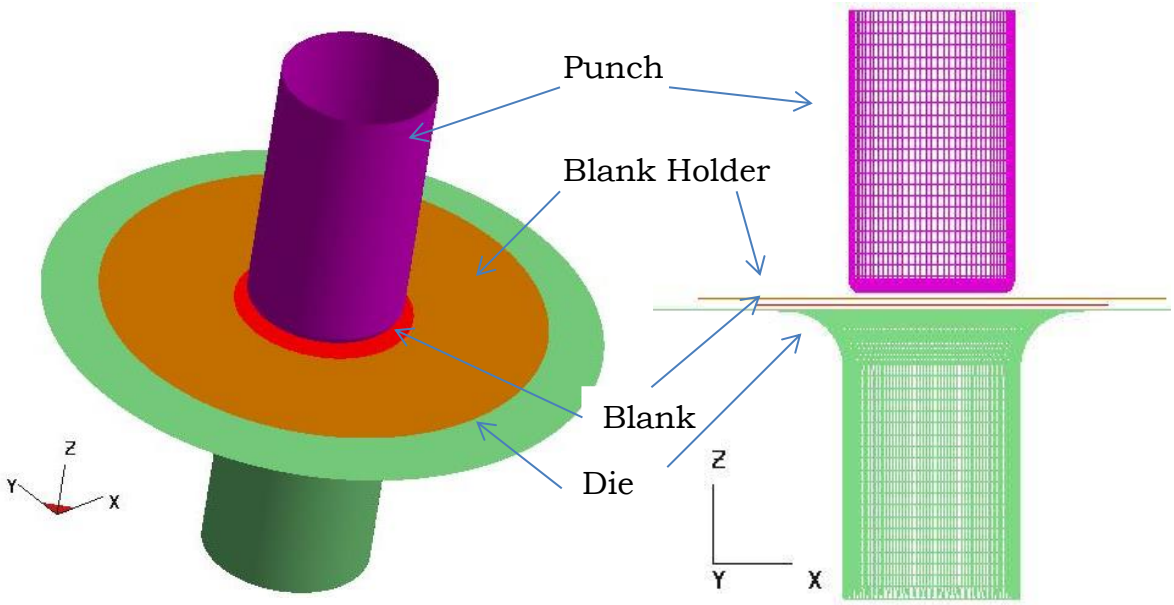

Figure 5.1: Tooling setup of deep drawing in FEM

Table 5.2: Process parameters of deep drawing at various temperatures

Temperature	Blank holding pressure	Friction coefficient	Lankford parameter		
			R_0	R_{45}	R_{90}
Room Temp	20 bar	0.15	0.878	1.004	0.810
150°C	15 bar	0.12	0.608	2.189	1.162
300°C	10 bar	0.09	0.916	1.214	0.624
400°C	8 bar	0.07	0.802	1.090	1.873
500°C	7.5 bar	0.07	0.809	1.013	1.663
600°C	7 bar	0.07	0.817	1.614	1.678

Barlat's yield criterion has been chosen as the material model in simulation at varies temperatures. At these temperatures, the material is anisotropic; this criterion incorporates the effect of both normal and planar anisotropy in the yielding behavior. Deep drawing simulations have been performed as per tooling setup, with different diameters of the blanks. Simulations have been carried out at different temperature conditions. Figure 5.2 shows the drawn cup from the blanks of different size with the thickness contours at room temperature conditions. It shows that the cups drawn have been in good form without any yielding. Thickness of the cup is not uniform, lowest thickness is observed at punch corner, where it has been reduced near to 0.9 mm for 66 mm blank. Figure 5.3 shows the FLDs of the cups. It shows that the strain of the sheet is below the FLC and does not show any indications of fracture in the cup walls. This indicates that the drawing is in the safe zone.

At room temperature when 67 mm blank has been drawn, the thickness at the punch corner has suddenly reduced to less than 0.3 mm. This indicates that drawn cup is not safe but, it leads to fracture, which is shown in Figure 5.4. In FLD it has been observed that the strain in the sheet is drastically increased. Here the strain has crossed the FLC and enter into the fracture zone.

Thicknesses of the simulated cups have been measured from the center of the cups to top of the wall and the graphs thickness vs distance have been drawn as shown in Figure 5.5. The curves of 64mm and 66 mm blanks are very close to each other with little deviation; this indicates that thickness variation is very small between these two cups. For the next higher

size of the blank 67 mm diameter thickness has been reduced to 0.3 mm which is not safe, but indicates the fracture, in the sheet at punch corner. With this it can be evident that at room temperature, maximum of 66 mm diameter blank can be deep drawn into cup of 30 mm diameter without fracture. With all these observations, it is evident that at room temperature LDR for ASS 316 is found to be 2.2.

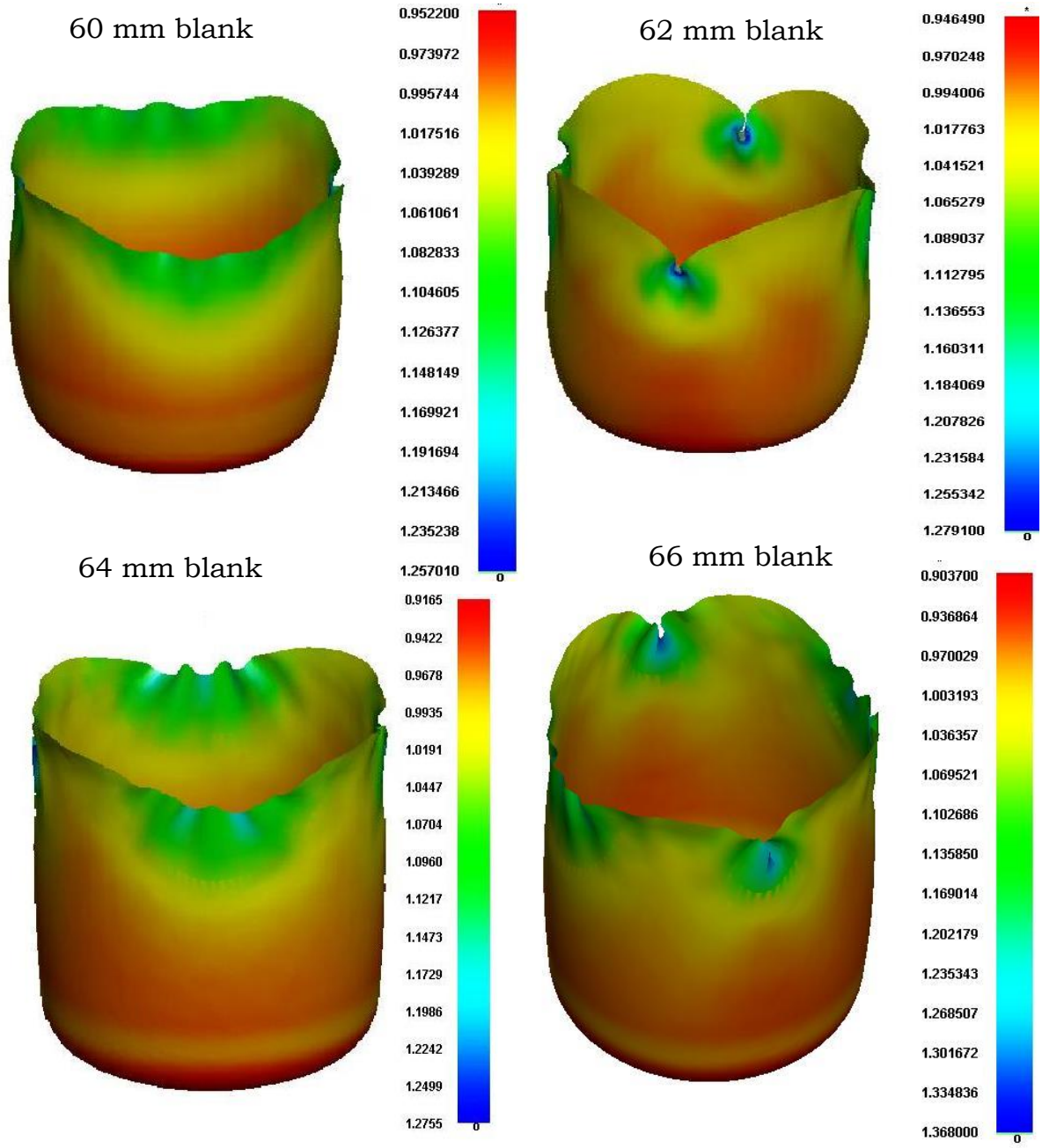

Figure 5.2: Drawn cups at room temperature from different sizes of the blank by FEM

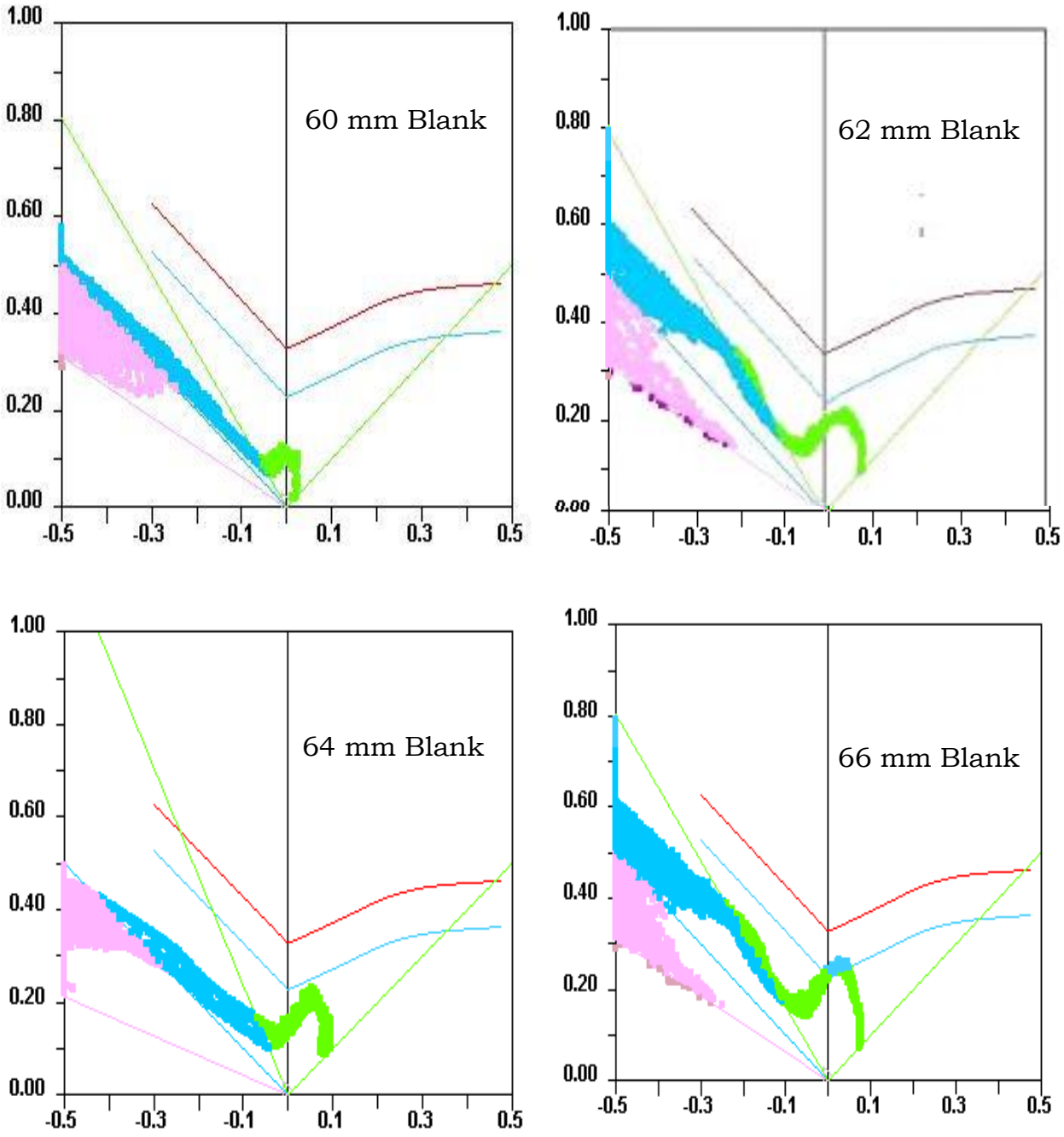

Figure 5.3: FLD of drawn cup from different sizes of blank at room temperature by FEM

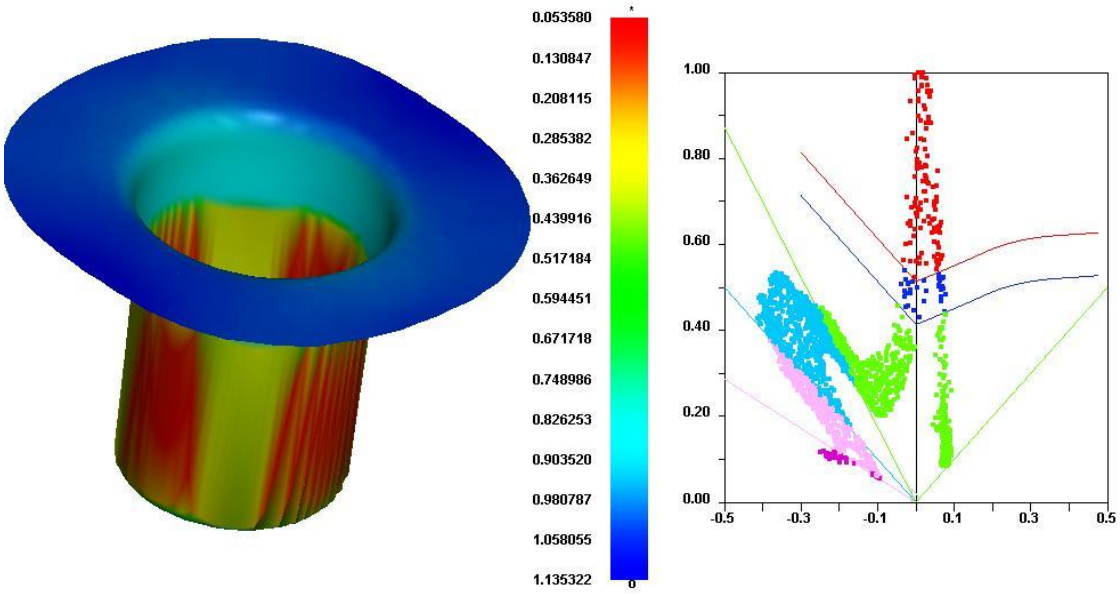

Figure 5.4: Fracture in drawn cup from Φ67 blank at room temperature, its FLD by FEM

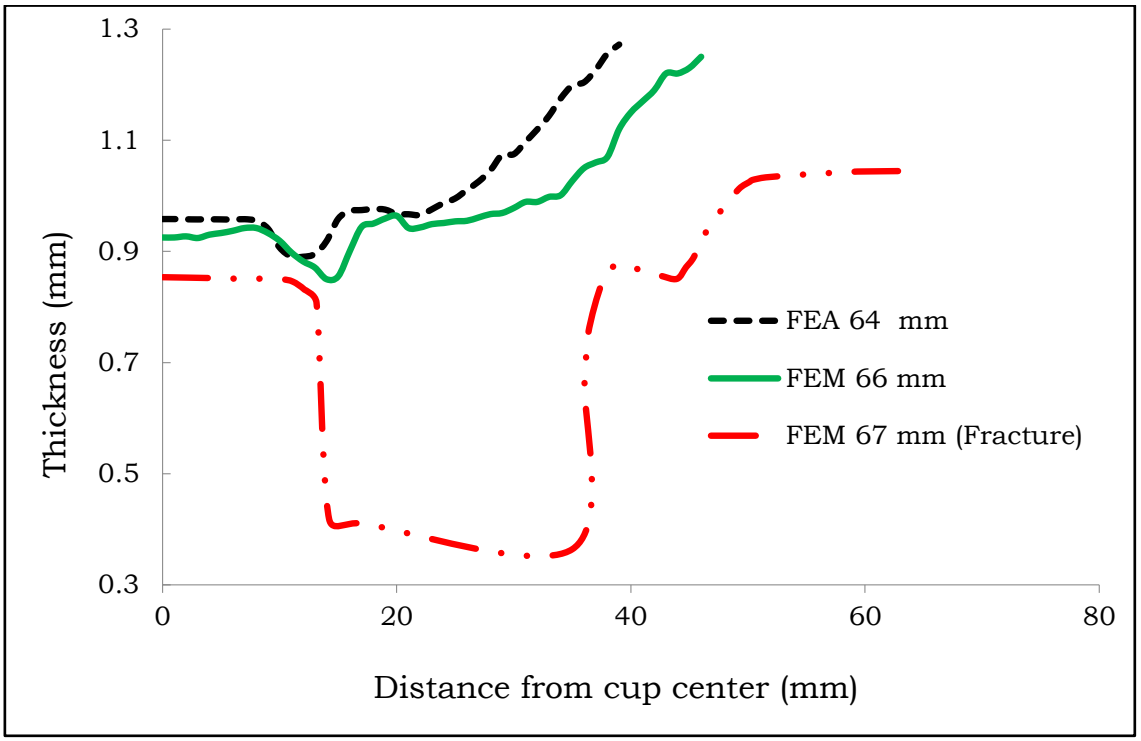

Figure 5.5: Thickness distribution of the drawn cup by FEM at room temperature

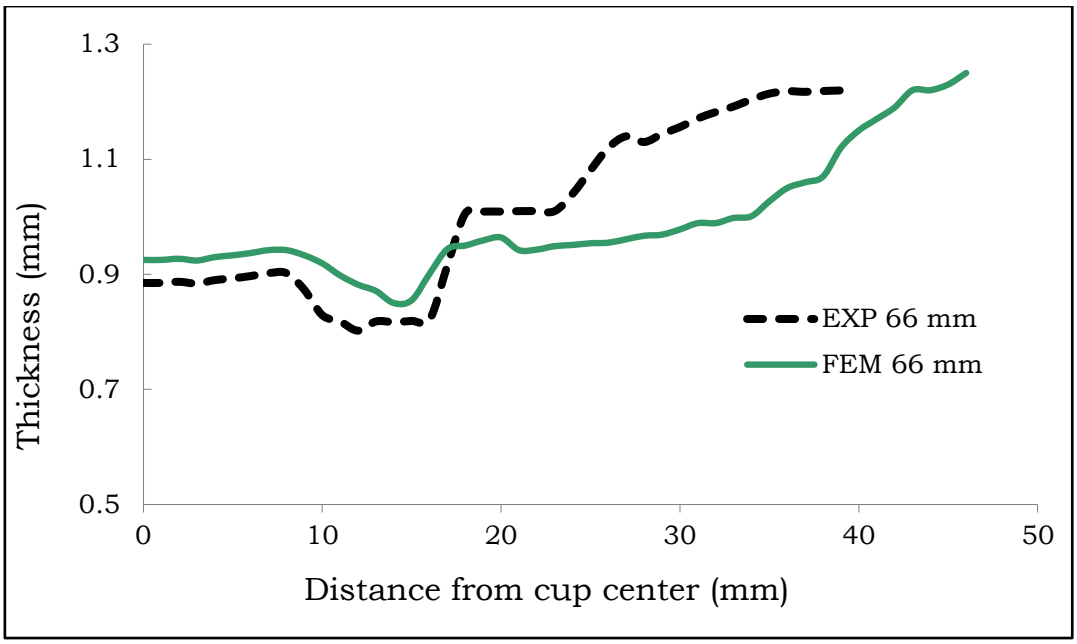

Figure 5.6: Thickness of the drawn cup at room temperature

Thickness variations of cup in simulations have been compared with the experimental drawn cups at LDR as shown in Figure 5.6. Thickness curve of the simulated cup in FEM is matched closely with that of experimental thickness at LDR. These curves are almost parallel with little deviation. Here the deviation of the thickness prediction of two processes is less than 10%. Average error is 4.9% and standard deviation is 3.9 %, this shows that the simulated thicknesses are predicted very accurately.

The von-Mises stress contour of drawn cup at LDR is shown in Figure 5.7. This indicates that stresses in the sheet are not uniform. Sheet has undergone different stresses due to metal flow under the punch force. At this state, stress appearing at punch corner radius is 244 MPa and in the wall region allowable stress is 489 MPa. At punch corner material can withstand less stress.

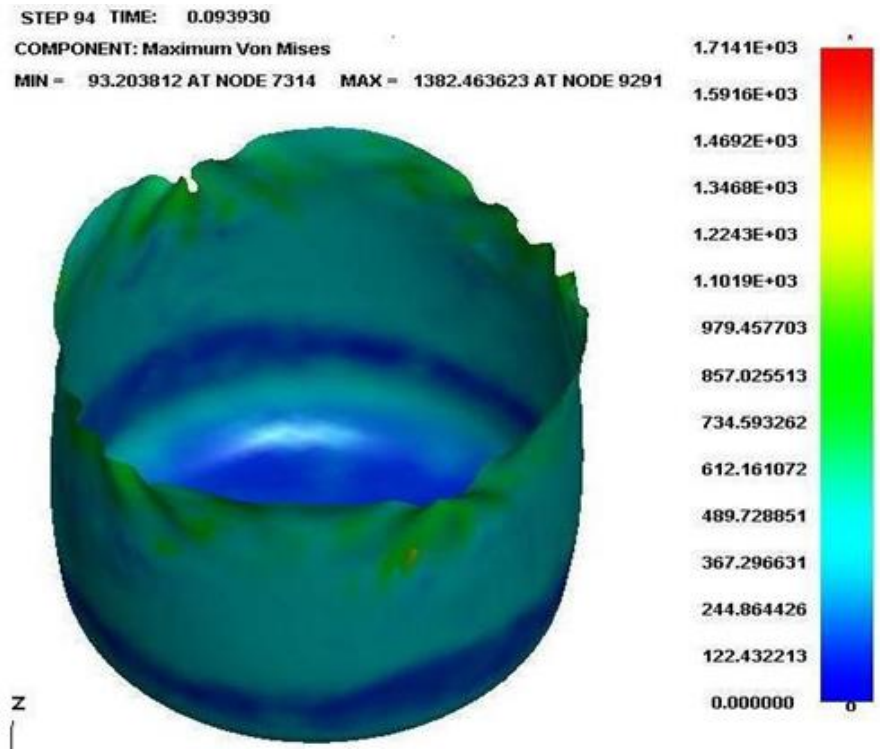

Figure 5.7: Stress contours of the drawn cup from LDR at room temperature

Figure 5.8 shows the graph of punch force applied on the blank during deep drawing vs stroke. With the advancement of the punch, the load has increased and reached to maximum in the first half of the stroke. Later it has decreased gradually and has reached to lowest at the end of the stroke. Deformation of the blank has been changed proportionately with the load. It has also been observed that the force needed to draw the blank, has increased with the size of the blank. 66 mm blank needs more force to draw the cup than other lower size blanks.

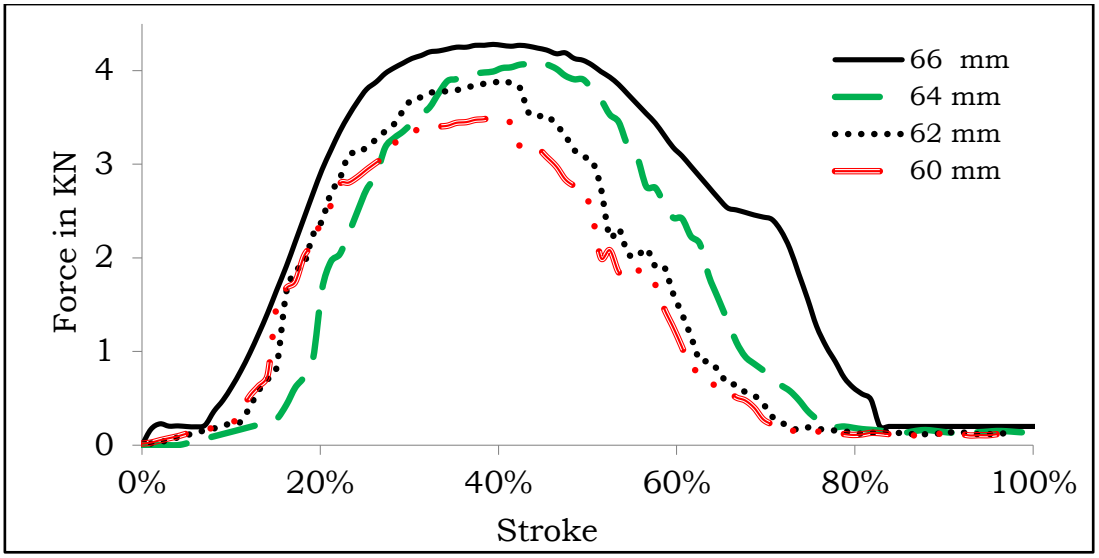

Figure 5.8: Force Vs Time step for deep drawn cup at room temperature in simulations

Simulations have been repeated at elevated temperatures with the material data available from tensile testing. At higher temperatures formability of material increases, so these simulations have been performed on the higher sizes of blanks. Here, blanks taken have the diameter more than 66 mm in the increment of 2 mm. The BHP has been taken, as per the size of the blank, and these pressures are given in Table 5.2. Barlat's yield criterion has been chosen as the material model in the simulation to incorporate the anisotropy of the material.

The drawn cups at 150°C with different blank sizes are shown in Figure 5.9 and 300°C are shown in Figure 5.10. The thickness and heights of the cups are changed with blank sizes and temperatures. With these simulated cups it has been observed that as the diameter increases thickness of the cup decreases. With increase in the size of the blank, its load carrying capacity increases so it can withstand higher forces, but with

increase in temperature, the strength of the material decreases and this make the material more ductile and leads to higher drawability.

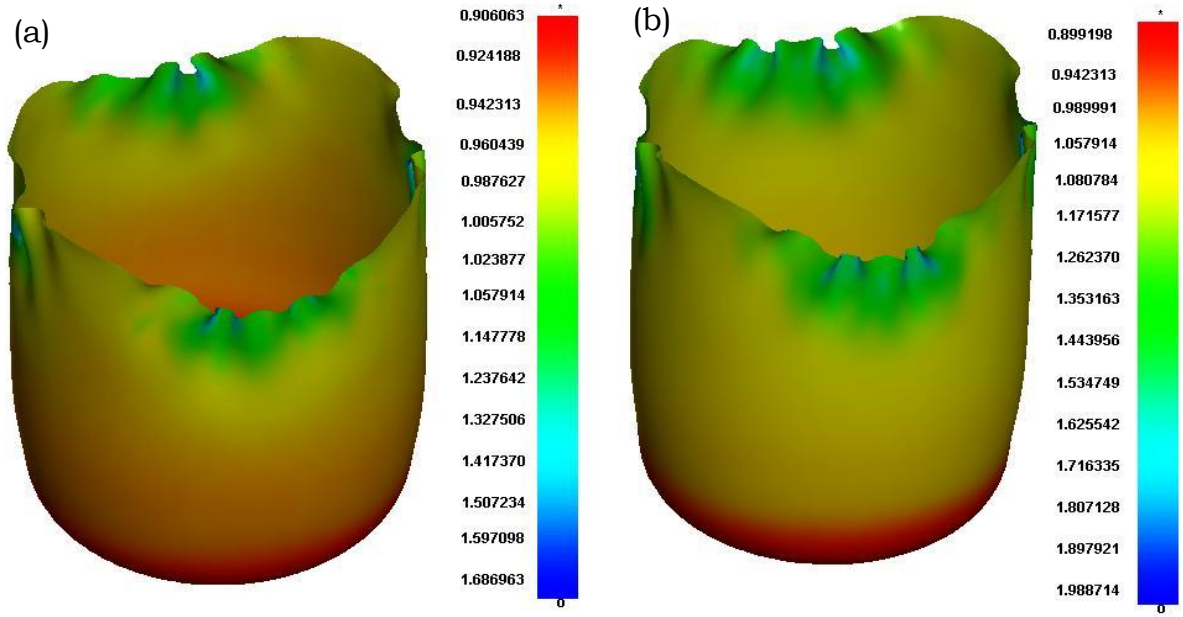

Figure 5.9: Drawn cups by FEM at 150°C from the blanks (a) Φ68 mm and (b) Φ70 mm

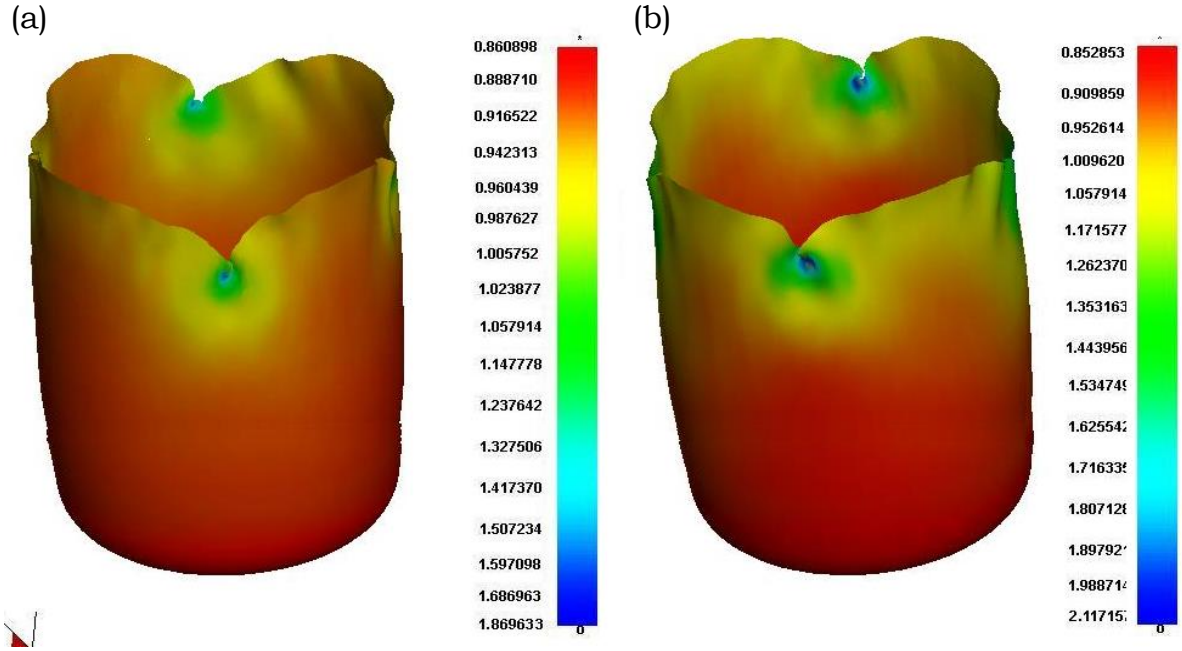

Figure 5.10: Drawn cups by FEM at 300°C from the blanks (a) Φ72mm and (b) Φ75 mm

In further study, thickness of the drawn cups at these temperatures have been measured and compared with those of experimental thickness. Figure 5.11 & 5.12 are shown the thickness distribution of the cup from the center to top of the wall at LDR. Like that of room temperature, a good correlations exists between simulated and experimental thickness of the cup here also. Barlat's material model simulates the process very well with good accuracy. Here average error is less than 6.6% and standard deviation is 5.2%, which indicates the very good correlation between experimental and simulated results even at higher temperatures.

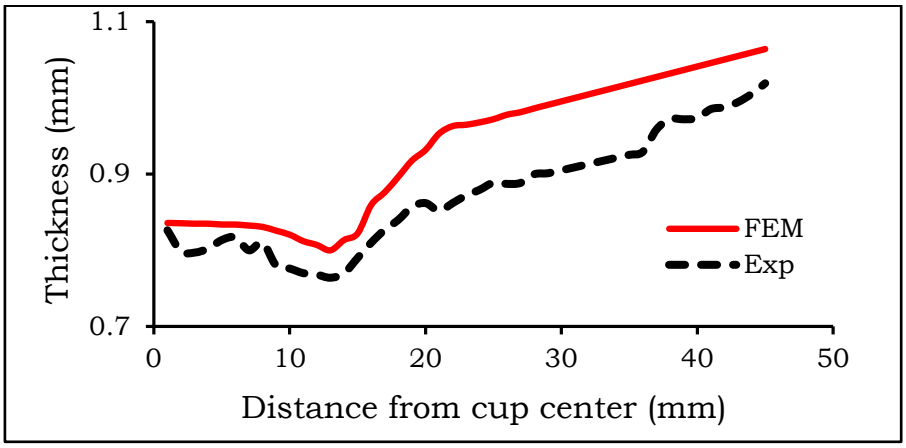

Figure 5.11: Thickness distribution of drawn cup from 70 mm blank at 150°C

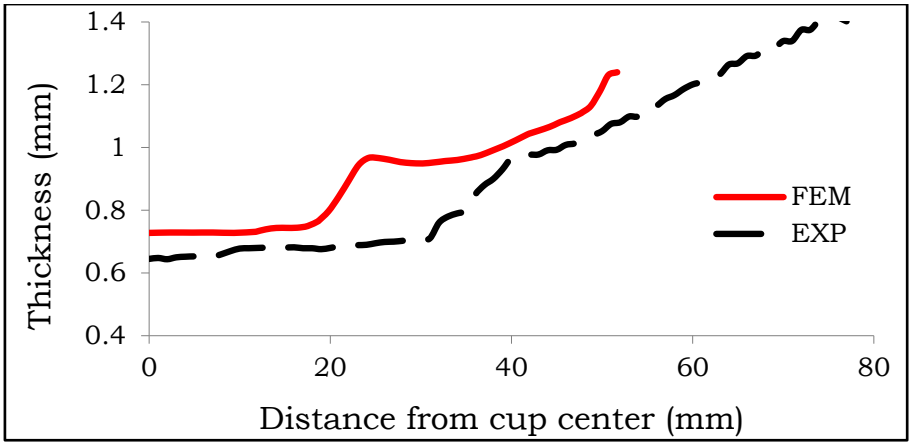

Figure 5.12: Thickness distribution of drawn cup from 74 mm blank at 300°C

At the elevated temperature higher sizes of the blanks can be deep drawn without fracture. Maximum of 70 mm diameter blank can be deep drawn safely at 150°C. Further increase in the temperature to 300°C, maximum of 75 mm blank can be deep drawn safely. At the temperature of 150°C the LDR of ASS 316 is 2.33 and it is increased to 2.5 at 300°C. There is a decrease in mean flow stress by the increase in temperature. This can be seen in the von-Mises counter at drawn cup at elevated temperatures as shown in Figure 5.13. At 150°C stresses at the punch corner have been reduced to 122 MPa and the average stress is 367MPa and at 300°C the average stress in the cup wall is 228 MPa. With increase in temperature average stress in the sheet is decreased which results in the increase of the sheet LDR. These simulations are in good agreement with the experimental results. Table 5.3 shows the LDR found by FEM simulations and by practical experimentations.

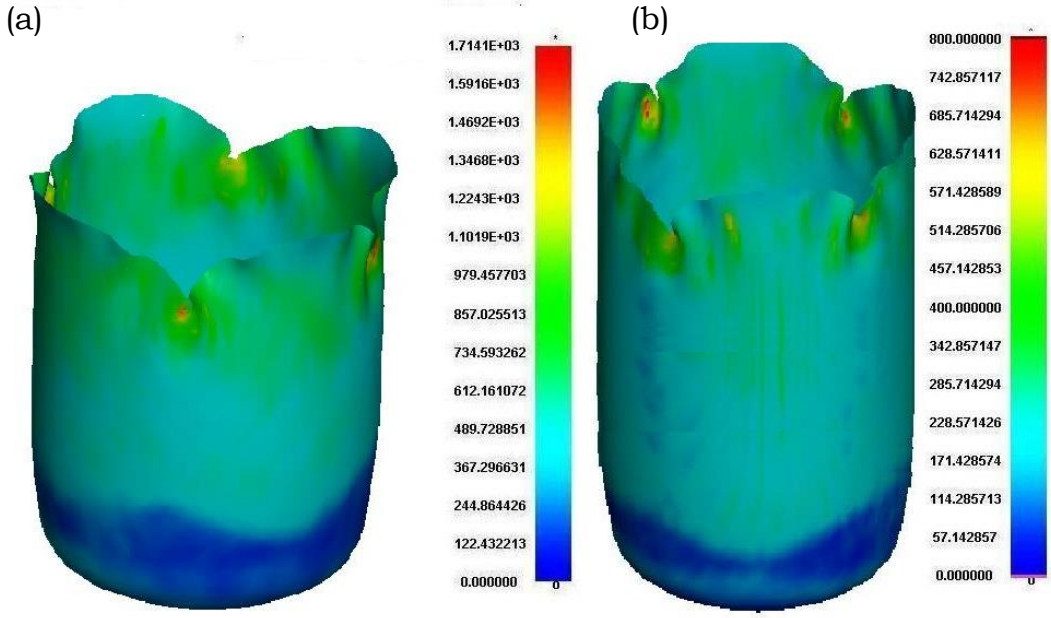

Figure 5.13: Stress contours of the drawn cup at (a) 150°C and (b) 300°C

Table 5.3: Experimental and simulated LDR

	LDR by	
Temperature	FEM Simulations	Practical Experiments
Room Temperature	2.20	2.20
150˚C	2.33	2.33
300˚C	2.50	2.47

Simulation study has been extended beyond 300°C to study the further increase in LDR of ASS 316. It has been observed that, at higher temperature LDR of the sheet metal has not increased, but the thickness of the cup has decreased. At 350°C thickness has been decreased to 0.75 mm and the thickness variations in the cup have been observed to be high, which results in poor quality cup.

5.4 Results of FE Analysis in DSA Region

In the experimental studies, it has been investigated that drawability of sheet decreases at 400°C due to the DSA phenomena. DSA occurs for ASS 316 in the temperate range of 400 to 600°C. Barlat's model cannot predict DSA phenomenon, but MTS model can predict DSA very well, so simulations have been performed using the MTS material model in LS Dyna with von-Mises yield criteria. Figure 5.13 shows the cup drawn by FEM using the MTS material model. It is shown safe in FLD but thickness is decreased to 0.45 mm, which is an indication of poor quality cup. Here, the drawn cup does not contain any earrings, which have been observed on the experimentally drawn cup in Figure 4.22. Also FLD is shown as a discontinued curve with MTS

model. This shows that the results are inappropriate. With MTS model, LDR has been predicted well, but thickness is not predicted accurately.

Simulations have been repeated with Barlat's material model with the material properties measure at 400°C. Simulated results are shown in Figure. 5.15. The cups simulated using Barlat's model resemble the experimental cups. In this, thickness of the cup has been reduced to nearly 0.8 mm. Figure 5.16 shows the thickness distribution curve of Barlat's model and MTS model. These have been compared with experimental cup thickness. Barlat's material model has predicted thickness more closely to experimental thickness than the MTS model. The MTS model with von-Mises yield criteria considers DSA phenomena, but it does not consider the anisotropic nature of the blank material. Whereas Barlat's model does not consider the DSA phenomena, but it takes the material properties measured at 400°C. These properties are influenced by DSA phenomena.

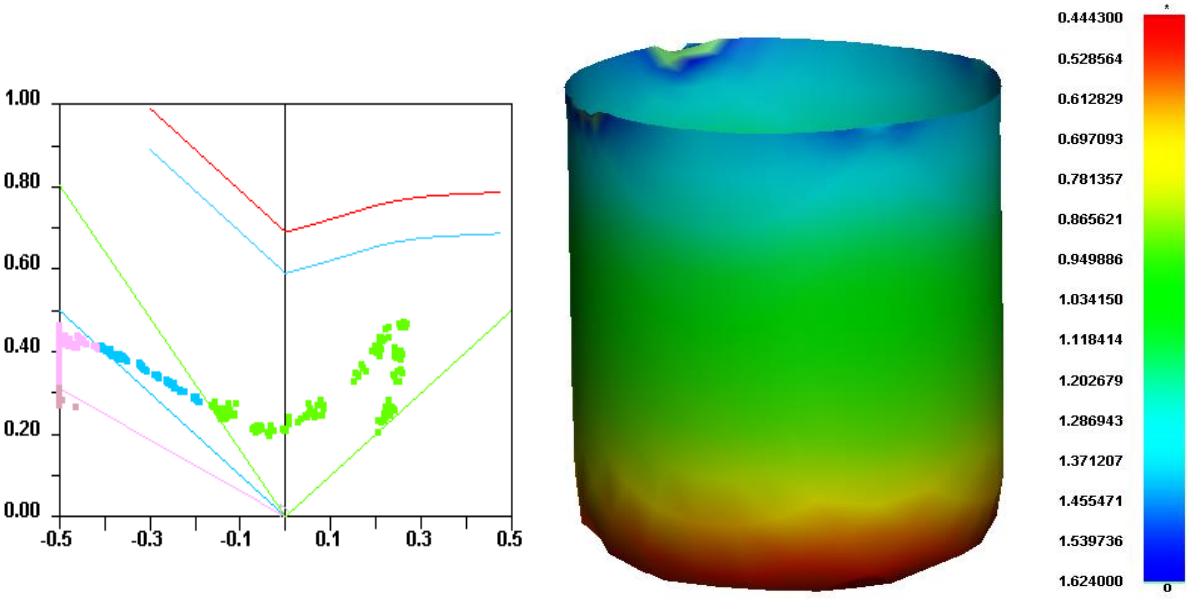

Figure 5.14: FLD and Simulated cup at 400°C in DSA region by MTS model

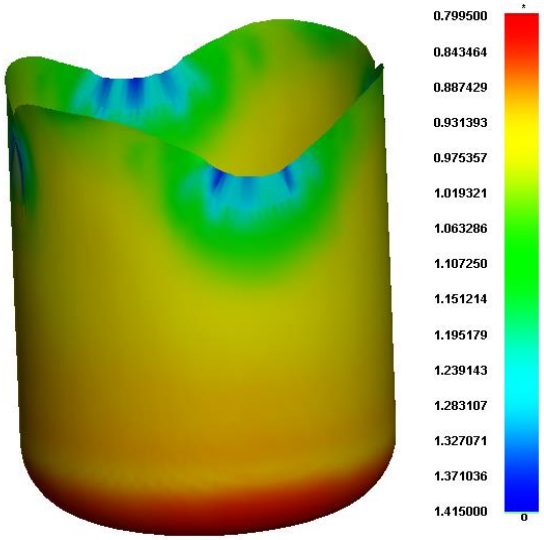

Figure 5.15: Simulated cup at 400°C in DSA region by Barlat's model

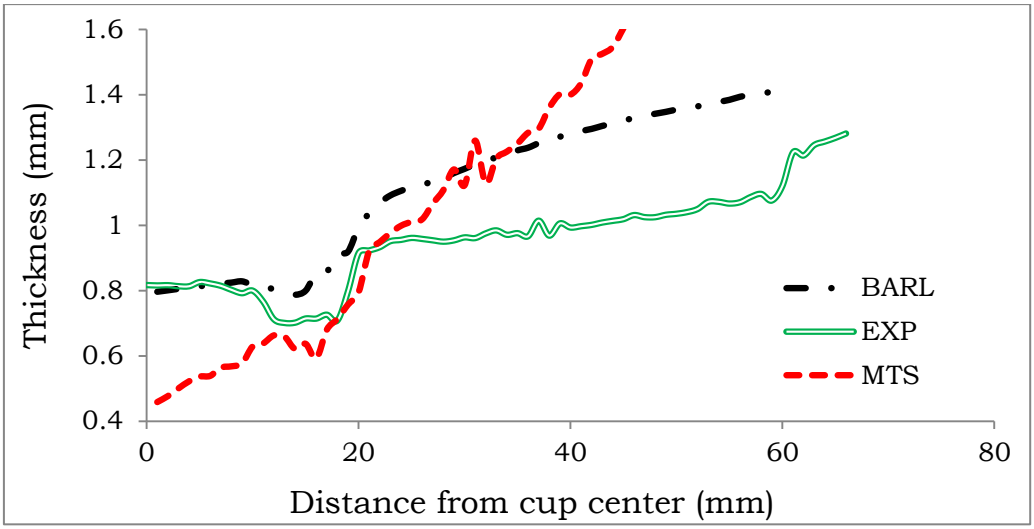

Figure 5.16: Thickness distribution of drawn cup in DSA region

Barlat's model has predicted the drawn cup parameters more accurately than the MTS model. MTS model along with von-Mises yield criteria considers the material as isotropic and so when the force is applied on the material, it undergoes deformation in all the directions uniformly. Thus, it is not capable of predicting earring and also it leads to higher strains in the thickness directions because of which thickness of the cup has reduced more at the base and increased at the top of the cup wall. It results

in more thickness variation in the drawn cup and thus the poor quality of cup.

Further investigations of formability have been performed in the DSA region at 500°C and 600°C using Barlat's model. At these temperatures maximum of 72 mm diameter blanks can be safely deep drawn and LDR of the material has observed same as that of 400°C. The next higher size of the blank has fractured at punch corner. Figure 5.17 shows the drawn cups with thickness contours. Here, it shows that the thickness of the cup has decreased due to increase in temperature. FLD of these cups are shown in Figure. 5.18. Its shows that drawn cups are safe without any fracture.

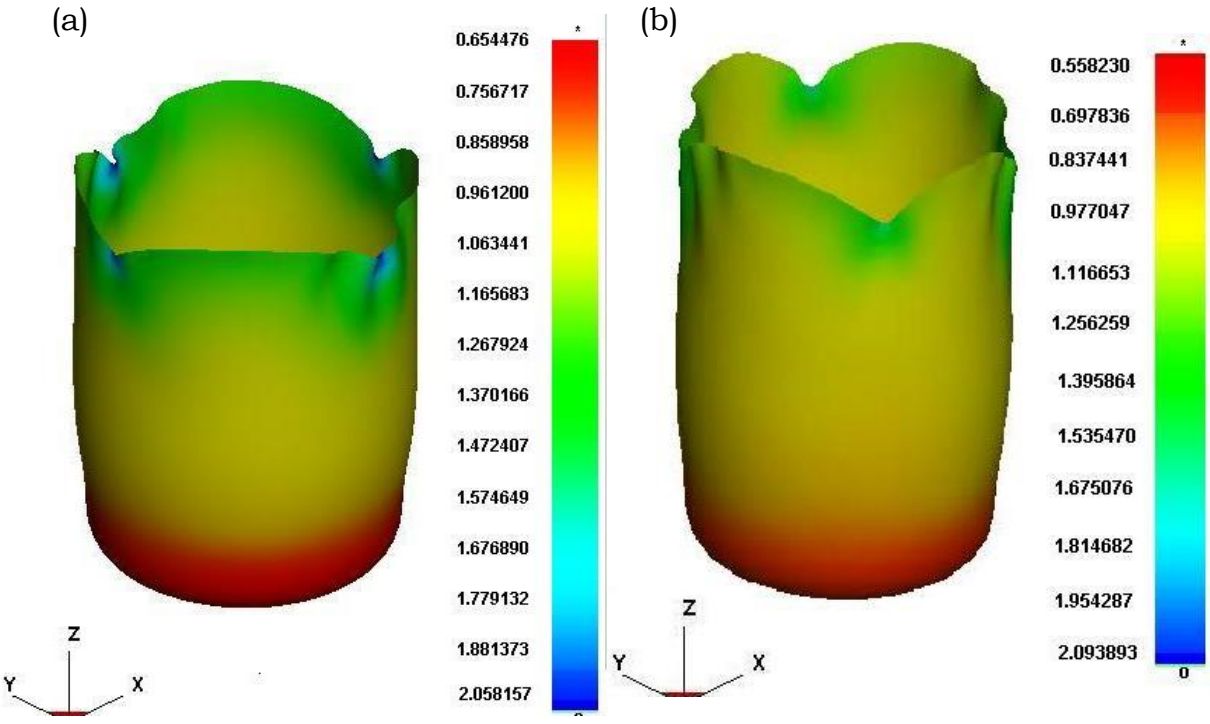

Figure 5.17: Drawn cups at 500°C and 600°C in DSA region by Barlat model

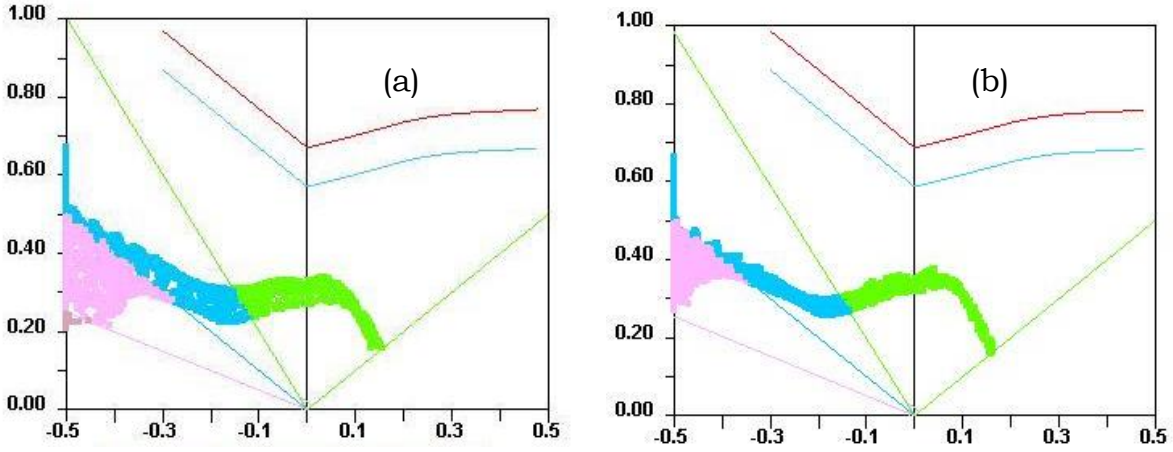

Figure 5.18: FLD of Drawn cups in DSA region at (a) 500°C and (b) 600°C

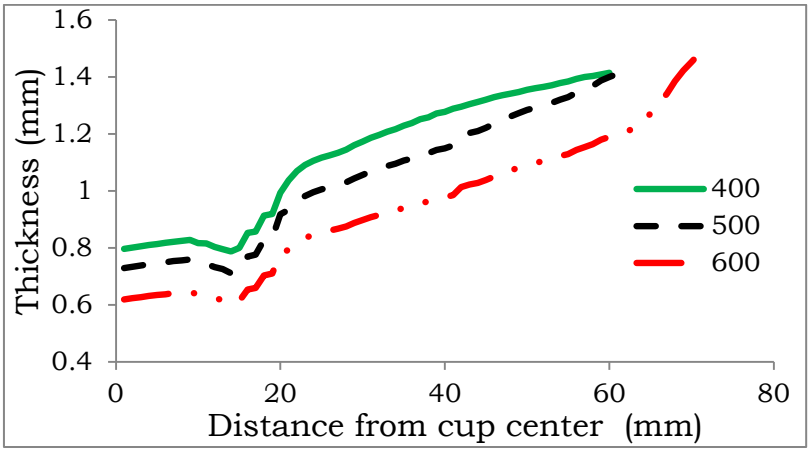

Figure 5.19: Thickness distribution of drawn cup at different temperatures in DSA region by FEM

Thickness of the cups have been measured from center to top of the wall and the graph has been drawn between thickness and distance from the center of the cup as shown in Figure 5.19. Thickness distribution of all the three cups drawn in DSA region is shown here. As the temperature is increased the thickness of the drawn cup has decreased. In the 500°C thickness of the cup has been decreased to 0.7 mm at punch corner and it further decreased to 0.55 mm at 600°C. At higher temperatures, the quality of the cups gets decreased, so it's not advisable to deep draw at these temperatures.

These simulation results reveal that the formability of ASS 316 has increased with the increase in temperature up to 300°C. Beyond this temperature, there is not much improvement in the LDR. Thickness reduction is more at 350°C, which leads to poor quality cups. Beyond 400°C LDR has decreased significantly because of the presence of DSA phenomenon.

Thickness prediction of the drawn cup at elevated temperature is a time consuming process. It requires a lot of time to conduct simulations or experiments at higher temperatures and measure the thickness. Artificial neural network (ANN) model is one of the techniques which can predict the thickness at any unknown temperature. ANN model is used to predict the parameters with very good accuracy, high correlation coefficient and less error. In the next section an ANN model has been developed to predict the thickness of the drawn cup with very good accuracy. This can facilitate to predict the quality of the cup.

5.5 Thickness Prediction by ANN Model

Artificial neural network (ANN) is a powerful data information treatment system which tries to simulate the neural network structure of the human brain. It can form complex non-linear relationships between inputs and outputs. Each neural network is composed of an input layer, an output layer and one or more hidden layers, which are connected by the processing units called neurons. Each neuron works as an independent processing element, and has an associated transfer function, which describes how the

weighted sum of its inputs is converted to the results into an output value. Currently, there are diverse training algorithms available. Among the various kinds of ANN approaches that have existed, the back propagation (BP) learning algorithm has become the most popular in engineering applications. BP algorithm is based on minimization of the quadratic cost function by tuning the network parameters. The mean square error (MSE) is considered as a measurement criterion for the training set. Especially, BP neural network is the most suitable tool for treating non-linear systems.

BP algorithms are applied to train a feed forward neural network, which are reliable and most commonly utilized. In this investigation, the input variables of ANN are temperature, LDR and distance from the center of the cup while the output variable is thickness. A feed forward network has been developed and trained with the back propagation algorithm, as shown in Figure 5.20. Before training the network, the input and output datasets have been normalized within the range of 0.05 – 0.95 to prevent a specific factor from dominating the learning for the ANN model. The main reason for normalizing the data matrix is that the variables have been measured in different units. These are recast into the dimensionless units to remove the arbitrary effect of similarity between the objects. Thus, using Equation 5.7, the experimental data has been normalized to make the neural network training more efficient prior to the use of the datasets. Once the best trained network has been found, all the transformed data returns to their original value using the equation 5.8.

$$X_n = 0.05 + 0.90\,(X - X_{min})/\,(X_{max} - X_{min}) \tag{5.7}$$

$$X = X_{min} + (X_n - 0.05)\,(X_{max} - X_{min})\,/\,0.9 \tag{5.8}$$

where X_{min} and X_{max} are the minimum and maximum values of X and X_n is the normalized data of the corresponding X.

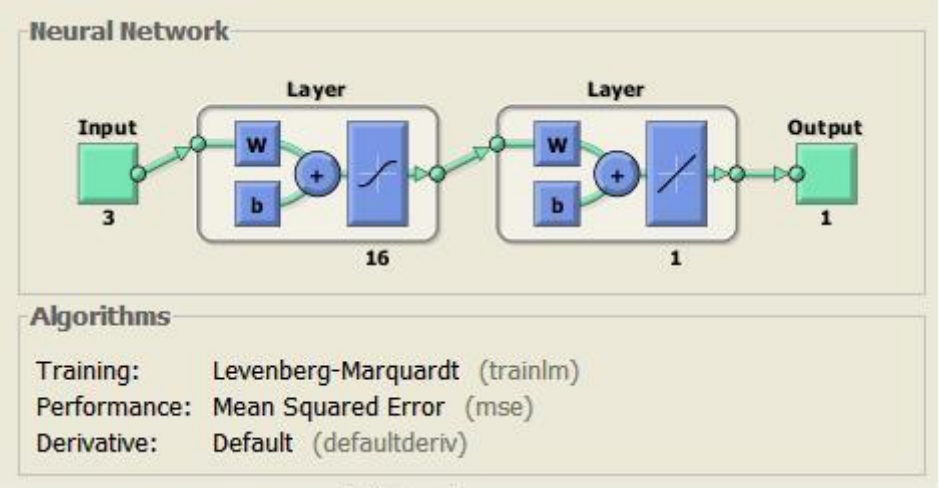

Figure 5.20: Schematic illustration of the neural network architecture

The architecture of ANN selection requires choosing both the appropriate number of hidden units and the connections there of. The desirable network architecture contains as minimal as possible hidden units and connections necessary for a good approximation of the true function. In most of the applications of ANN, this selection is done using a trial-and-error procedure. The number of hidden layers determines the complexity of neural network and precision of predicted values.

If the architecture is too complex, it may not converge during training or the trained data may be over fitted. In other words, the trained network might not have sufficient ability to learn the process correctly. Therefore, various network structures with varying number of neurons in the hidden layer have been examined. Figure 5.21 shows the influence of the number of neurons in the hidden layer on the network performance. The value of mean

square error (MSE) has been used to check the ability of a particular architecture. It has been observed that, the mean square error of the network decreases to the minimum value when the number of neurons was 15. This indicates that a network with 15 neurons in the hidden layer can exhibit the best performance.

The ANN model has been developed to predict thickness at any unknown temperature. For the thickness prediction by ANN three temperatures (50°C, 150°C and 300°C), LDR at these temperatures and the thickness at an interval of 1 mm from the center have been taken. Thus, total data points are 113, from which 90% data points (102) have been randomly selected as a training data set and the remaining 10% data points (11) have been taken as testing data set. The correlation coefficient *(R)* is a commonly used statistic and provides information on the strength of the linear relationship between experimental and predicted values. For perfect prediction, all the data points should lie on the line inclined at 45° from horizontal.

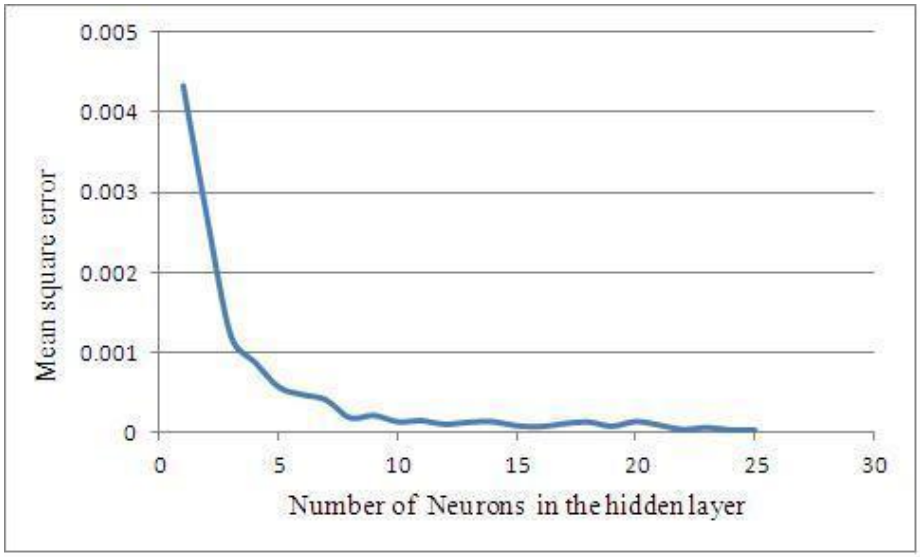

Figure 5.21: Influence of hidden neurons on the network performance

5.6 Comparison of ANN Model with Experiments

Figures 5.22 and 5.23 represent the predicted versus experimental thickness values for the training and testing data sets respectively. The correlation coefficient has been found to be 0.9976 for the training data set and 0.9954 for the testing dataset. This indicates a very good correlation between experimental and predicted thickness values. The results imply that the developed ANN model for ASS 316 is consistent with what is expected from the fundamental theory of hot deformation. Thus, the ANN model can be used to predict the thickness distribution of the drawn cup at any unknown temperature to a very close accuracy.

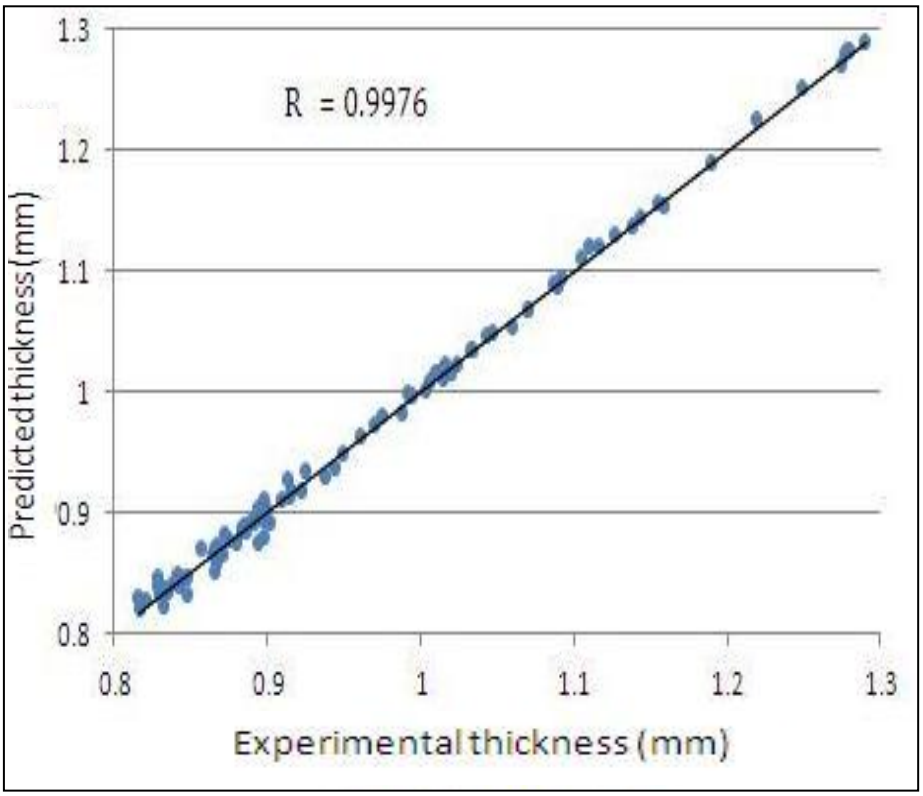

Figure 5.22: Comparison between experimental and predicted thickness values for the training data set.

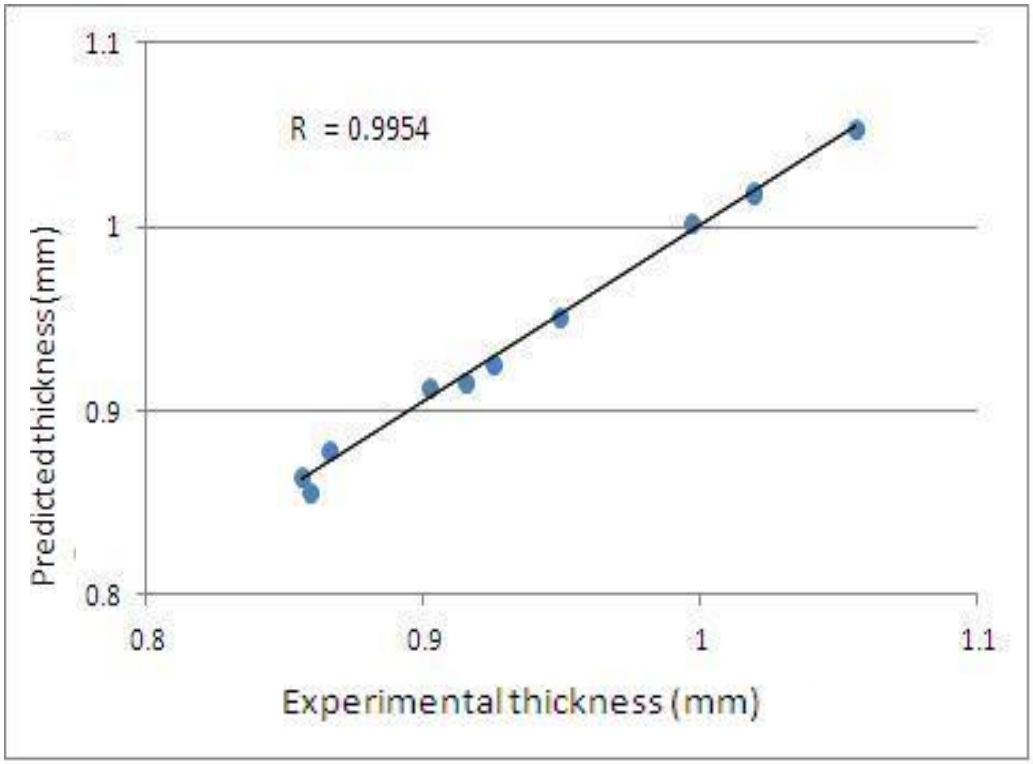

Figure 5.23: Comparison between experimental and predicted thickness values for the testing dataset.

Table 5.4 shows the experimental and the ANN model predicted thickness along with the associated absolute and percentage errors for randomly selected unseen testing dataset. The maximum percentage error is found to be 1.1%, which has been considered very less. As the temperature of the material increases, there is a decrease in the cup thickness due to decrease in flow stress and work hardening coefficient. In general, the performance of any function fitting technique will be better, if more numbers of data are taken near the domain boundaries. This ANN model predicts the thickness to very high accuracy.

Table 5.4: Comparison of ANN predicted vs. experimental thickness for the testing dataset

S.No	Temp	LDR	Distance	Exp	Predicted	Error	% Error
1	50	66	7	0.902	0.913	0.011	1.1
2	50	66	20	0.997	1.002	0.005	0.5
3	50	66	23	1.019	1.017	0.002	0.2
4	50	66	24	1.019	1.019	0	0
5	50	66	30	1.056	1.054	0.002	0.2
6	150	70	6	0.915	0.915	0	0
7	150	70	19	0.925	0.926	0.001	0.1
8	300	74	11	0.859	0.856	0.003	0.3
9	300	74	17	0.856	0.865	0.009	0.9
10	300	74	18	0.866	0.868	0.002	0.2
11	300	74	25	0.949	0.951	0.002	0.2

FE analyses at different temperatures have studied the forming behavior of ASS 316. Simulations of deep drawing have been performed in LS Dyna with the material properties measured by tensile testing at different temperatures. These simulations have revealed that the formability of ASS 316 is increased with the increase in temperature. At higher temperature, LDR of sheet metal has increased and the thickness decreased due to decrease in flow stresses. LDR is highest at 300°C with less thickness variations and it has been found as the most suitable temperature to deep draw ASS 316 for achieving high LDR. These simulations have very good correlation with experimentations. Next chapter focuses on the study of FLD for ASS 316 at 300˚C by theoretical models and experimentations for validation.

CHAPTER 6:

Study of Forming Limit Diagram

The development of the production of new parts, by forming of an operation or several progressive operations, demands good knowledge of the attainable forming limits. In sheet metal forming operations formability is limited by the onset of localized necking [102]. It is necessary to know the limit up to which the material can be formed. FLD offers a convenient and useful tool to predict the forming behavior in sheet metal forming. FLD attempts to provide a graphical description of material failure during sheet metal forming processes like deep drawing. These show the critical combinations of major strain and minor strain in the sheet surface at the onset of necking failure. FLD consists of forming limit curve (FLC), which indicates the limit of strain before fracture as shown in Figure 6.1. Above FLC, the localized necking and fracture appear and so this is called as fracture zone. A parallel curve to FLC, which is 10% offset below FLC, is referred as yield curve. Strains below this yield curve show safe zone. The region in between FLC and yield curve is considered to be marginal.

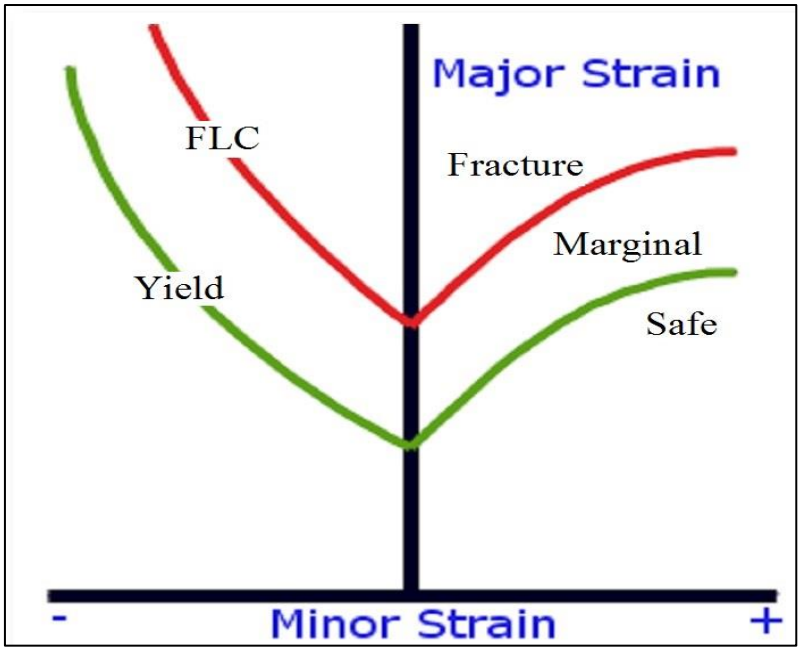

Figure 6.1: Different zones in FLD

With the help of FLD, it is possible to evaluate different strain conditions in the same diagram and determine the fracture limit for the particular strain combination. Figure 6.2 shows the different strain conditions in FLD. Possible different strain conditions in the drawn cups are represented in the same diagram. Figure 6.3 shows the fracture limits in formed cups for the particular combinations of strains [103, 104].

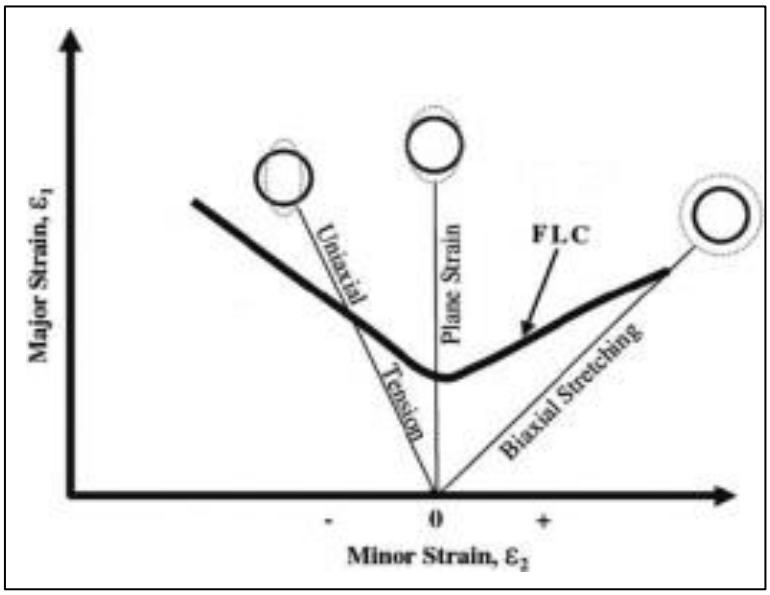

Figure 6.2: Different strain paths in FLD [103]

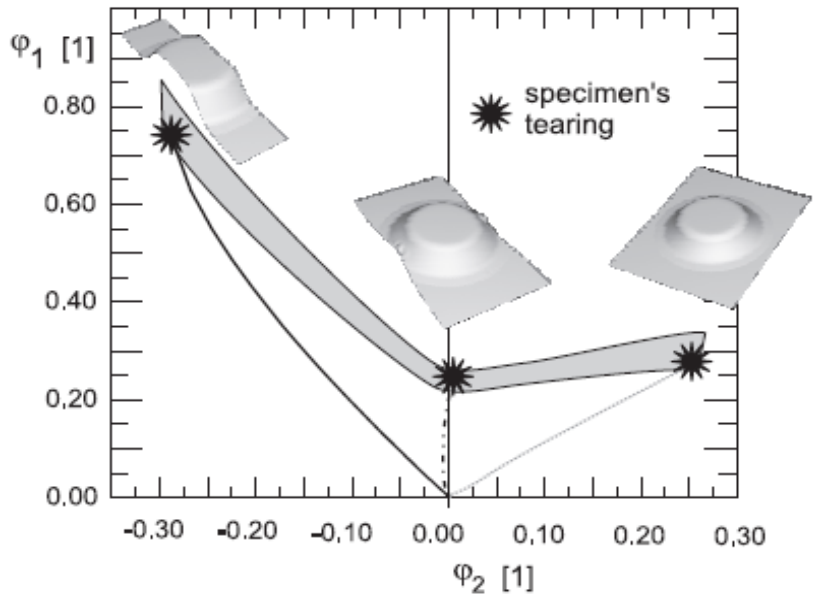

Figure 6.3: Different strain conditions in cups during deep drawing [104]

6.1 Theoretical Measurement of FLD

The Marciniak–Kuczynski (MK) analysis has been one of the most commonly used approaches for numerical determination of FLC. In MK analysis, a thickness imperfection is introduced far away from the sheet metal boundary to simulate pre-existing defects in the sheet material. It has been shown that the presence of even slight intrinsic inhomogeneity in load bearing capacity throughout a deforming sheet can lead to unstable growth of strain in weaker regions, causing localized necking and failure. Necking is considered to occur when the ratio of the effective total strain in the groove region to that in the nominal region of the sheet is above a critical value.

The MK analysis has been used extensively in numerical analyses based on constitutive models at two different length scales; micro scale and macro scale. The micro scale models incorporate crystal plasticity theories into the MK model and thus account for the microstructure of the material. The macro scale models are based on phenomenological yield functions to predict the material response. In order to model the inherent anisotropy in the ASS 316 sheet metal, i.e., the variation in the yield stress and *R*-values with orientation (with respect to rolling direction), two anisotropic, Hill's and Barlat's, yield functions have been considered. Barlat's yield function has already been presented in Section 5.2.1. Herein, Hill's yield function is being briefly presented as follows.

6.1.1. Hill's Yield Criterion

Hill (1948) proposed an anisotropic yield criterion as a generalization of the Huber-Mises-Hencky criterion with anisotropy in three orthogonal

symmetry planes [105]. The yield criterion is expressed by a quadratic function of the following type:

$$2f(\sigma_{ij}) \equiv F(\sigma_{22}-\sigma_{33})^2 + G(\sigma_{33}-\sigma_{11})^2 + H(\sigma_{11}-\sigma_{22})^2 + 2L\sigma_{23}^2 + 2M\sigma_{31}^2 + 2N\sigma_{12}^2 = 0 \quad (6.1)$$

where *f* is the yield function; *F, G, H, L, M* and *N* are constants specific to the anisotropy state of the material, and *x, y, z* are the principal anisotropic axes. Axis *1* is usually parallel to the rolling direction, Axis *2* is parallel to the transverse direction and Axis *3* is collinear with the normal direction. The relations between the anisotropy coefficients, the yield stresses and the coefficients may be easily obtained from the flow rule associated to the yield function.

$$r_0 = \frac{H}{G};\ r_{90} = \frac{H}{F};\ r_{45} = \frac{N}{F+G} - \frac{1}{2}; \quad (6.2)$$

$$\frac{\sigma_0}{\sigma_{90}} = \sqrt{\frac{r_0(1+r_{90})}{r_{90}(1+r_0)}} \quad (6.3)$$

In case, for plane stress condition, principal directions of the stress tensor are coincident with the anisotropic axes ($\sigma_{11} = \sigma_1; \sigma_{22} = \sigma_2;\ \sigma_{12} = 0$), the Hill 1948 yield criterion can be written as a dependence of the principal stress in the form. (Using the anisotropy coefficient and σ_0)

$$\sigma_1^2 - \frac{2r_0}{1+r_0}\sigma_1\sigma_2 + \frac{r_0(1+r_{90})}{r_{90}(1+r_0)}\sigma_2^2 = \sigma_0^2 \quad (6.4)$$

Hill'48 yield criterion can also be expressed in a different way. This is done by using r_0, σ_0 and σ_{90}as:

$$\frac{{\sigma_1}^2}{{\sigma_0}^2} - \frac{2r_0}{(1+r_0){\sigma_0}^2}\sigma_1\sigma_2 + \frac{{\sigma_2}^2}{{\sigma_{90}}^2} = 1 \quad (6.5)$$

6.1.2. Marciniak Kuczynski Model

To predict the theoretical forming limit curves, the MK model assumes an initial thickness imperfection in the geometry of the sheet in the form of a groove across the width of the sheet. The zone outside the groove is referred to as zone A and the groove is referred to as zone B, as shown in Figure 6.4. A Cartesian coordinate system is aligned with the symmetry axes: the x-axis is along the rolling direction (RD), and the y-axis is along the transverse direction (TD).

This initial imperfection can be defined by a thickness ratio:

$$f_0 = \frac{h_0^B}{h_0^A} < 1 \tag{6.6}$$

where h_0^A, h_0^B are the initial thicknesses of zone *A* and zone *B*, respectively. f_0 is a parameter of the MK model. The boundary of the sheet (assumed to be far away from the groove) is subjected to monotonic proportional straining parallel with the symmetry axes.

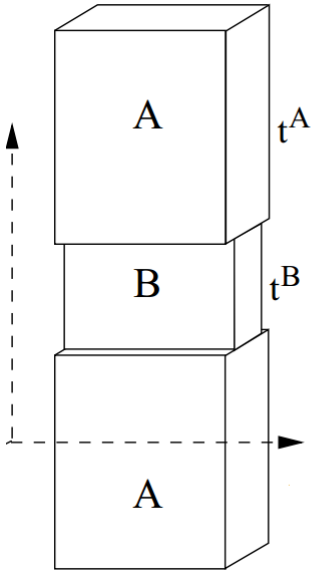

Figure 6.4: Geometry of the sheet in MK model

$$\rho = \frac{\epsilon_y^A}{\epsilon_x^A} \tag{6.7}$$

where ϵ_x ϵ_y, are components of strain along the coordinate axes. The ϵ_x component of the strain is usually referred to as the major strain, whereas ϵ_y is called the minor strain (the case when the major strain is along the transverse direction is treated similarly).

The value of f_0 is varied until the theoretically predicted FLC curve agrees best with the experimental curve at the plane strain point, i.e., for ρ = 0. For the present analysis, the value of f_0 chosen is 0.99.

As the straining at the boundary increases, the thickness of zone B reduces continuously and faster than that of region A. Hence it has to bear increasingly higher stresses than those in zone A. There will be a point when the region B has deformed substantially more than region A, signaling the start of necking. The failure criterion is thus:

$$\frac{d\overline{\epsilon_A}}{d\overline{\epsilon_B}} < N \tag{6.8}$$

$d\overline{\epsilon_A}$, $d\overline{\epsilon_B}$ denote the equivalent plastic strains in the respective regions. From a computational point of view, the constant N should be a small number so as to ensure that region B has deformed sufficiently more than region A. Then it can be said with certainty that necking would have occurred. N = 0.15 was used for this analysis.

As presented by Li Xiaoqiang *et al.* [106] and Siguang and Weinmann [107], the general stress state of the material is described by the power law equation:

$$\bar{\sigma} = K\overline{\epsilon^n}\dot{\epsilon^m} \tag{6.9}$$

where n is the strain hardening coefficient, m is the strain rate sensitivity coefficient.

The ratio of principal stresses and strains is defined as:

$$\alpha = \frac{\sigma_y}{\sigma_x}, \rho = \frac{\epsilon_y}{\epsilon_x} = \frac{d\epsilon_y}{d\epsilon_x} \tag{6.10}$$

The effective stress and strain are defined as:

$$\bar{\sigma}\bar{\epsilon} = \sigma_x\epsilon_x + \sigma_y\epsilon_y = \sigma_x\epsilon_x(1 + \alpha\rho) \tag{6.11}$$

The associative flow rule is given by:

$$d\epsilon_{ij} = d\lambda \frac{\partial \bar{\sigma}}{\partial \sigma_{ij}} \tag{6.12}$$

From the associative flow rule and the constant volume condition

$$d\epsilon_x + d\epsilon_y + d\epsilon_z = 0 , \tag{6.13}$$

The MK model incorporates a compatibility condition

$$d\epsilon_y^A = d\epsilon_y^B \tag{6.14}$$

Furthermore, the sheet metal being deformed will always be in equilibrium. This is represented by the force balance equation:

$$\varphi_A\left(\overline{\epsilon^A} + \overline{d\epsilon^A}\right)\dot{\epsilon^m}_A = f\varphi_B\left(\overline{\epsilon^B} + \overline{d\epsilon^B}\right)\dot{\epsilon^m}_B \tag{6.15}$$

where $\varphi = \frac{\sigma_x}{\bar{\sigma}}$ and $f = \frac{t_A}{t_B}$., t_A, t_B denote the instantaneous thicknesses of regions A and B. This ratio can be found by using the equation:

$$f = f_0 exp(\epsilon_z^A - \epsilon_z^B) \tag{6.16}$$

Initially values of f_0 and ρ are assumed. Small strain increments of $d\epsilon_x^B$ are imposed in the groove region. The values of $d\epsilon_y^B, d\epsilon_x^b$ are found using the

corresponding equations described above. Assuming a value for $d\epsilon_x^A$, the values of $d\epsilon_y^A$, $d\epsilon_x^A$ are computed. The equality of the force balance equation is checked. If the equality is satisfied, then the necking criterion is checked. If the necking criterion is also satisfied, then that particular strain state of region A corresponds to a point on the FLC. If the assumed value of $d\epsilon_x^A$ does not correspond to equal values of left and right hand sides of the force balance equation, the assumed value is changed and the process is repeated. This procedure is done for different values of f_0 and ρ to plot the full FLC.

6.2 Experimental FLD

The experimental FLC curves have been plotted by conducting hemispherical dome punch test as per ASTM E2218 standards. This is a step-by-step exercise used to construct forming limit curves. These give us useful information about the combinations of major and minor strains are likely to result in failure for a material of a given blank. The hemispherical punch test is a simple experimental test which strains the sheet material in both directions. The shape of the punch is hemispherical and set-up has been selected for a straight-forward stretching of the sheet. This test is much simpler to perform than the other experimental techniques for FLD. The test set-up is made of a hemispherical punch, a die, a blank-holder and a draw-bead to prevent any material flow, as shown Figure 6.5. Grids are etched on the blank and allowed to deform under load. Strain distributions in both the directions have been determined by measuring the grid dimensions post deformation.

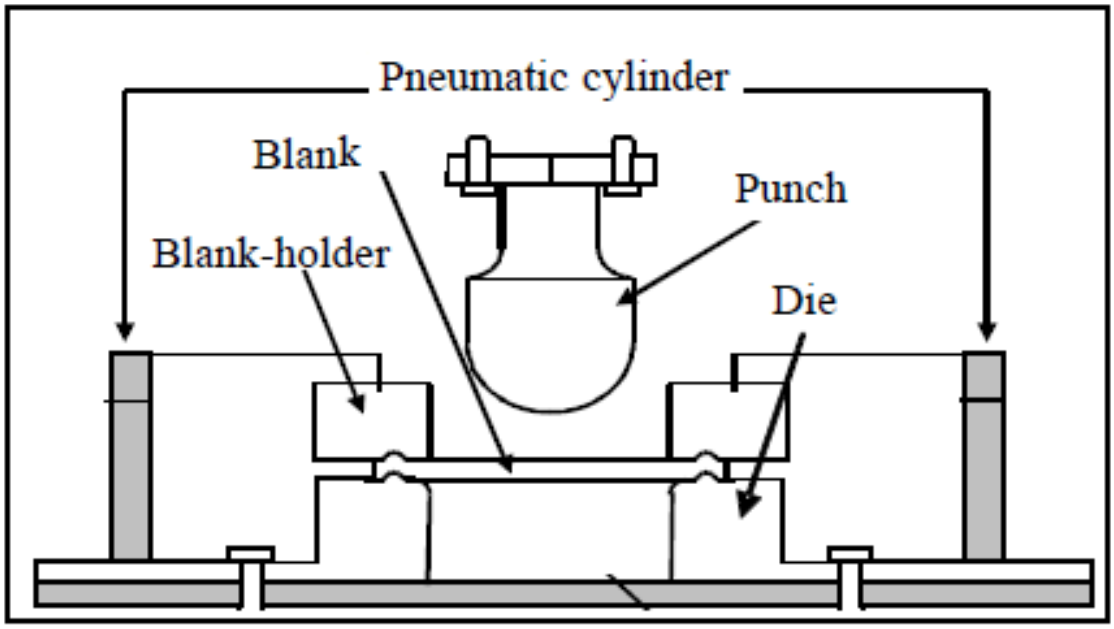

Figure 6.5: Test setup for FLD as per ASTM E2218

Experimental tests are suitable for the evaluation of the entire range of the FLD with a simple tooling and an experimental procedure. Determination of the FLD with a punch tool test consists of the stretching die, and hemispherical punch similar to the Nakazima test. The experimental determination of the FLD has been done by stretching rectangular specimens with different widths. Various strain conditions are achieved by different widths of the specimens which enable the determination of the entire range of the FLD with one tool geometry. During the testing procedure the punch and blank causes the different strain conditions to analyze the specimen.

The test has been performed on the experimental test rig as shown in Figure 6.6. This setup is similar to deep drawing setup, but the blank holder and punch have different shape to make the sheet blank to stretch under the load. Blank holder has a groove bead to hold the blank without slip and punch has a hemispherical bottom to stretch the sheet blank, and diameter of the punch is 50 mm. Specimens used in this study are of 110 mm length

with different widths. The test rig comprises of a 20 ton hydraulic press as used in the deep drawing setup. Grids have been marked on the blanks using electrolytic etching before the test. After the hemispherical dome tests, the deformed grids have been measured using a travelling electron microscope as shown in Figure 6.7.

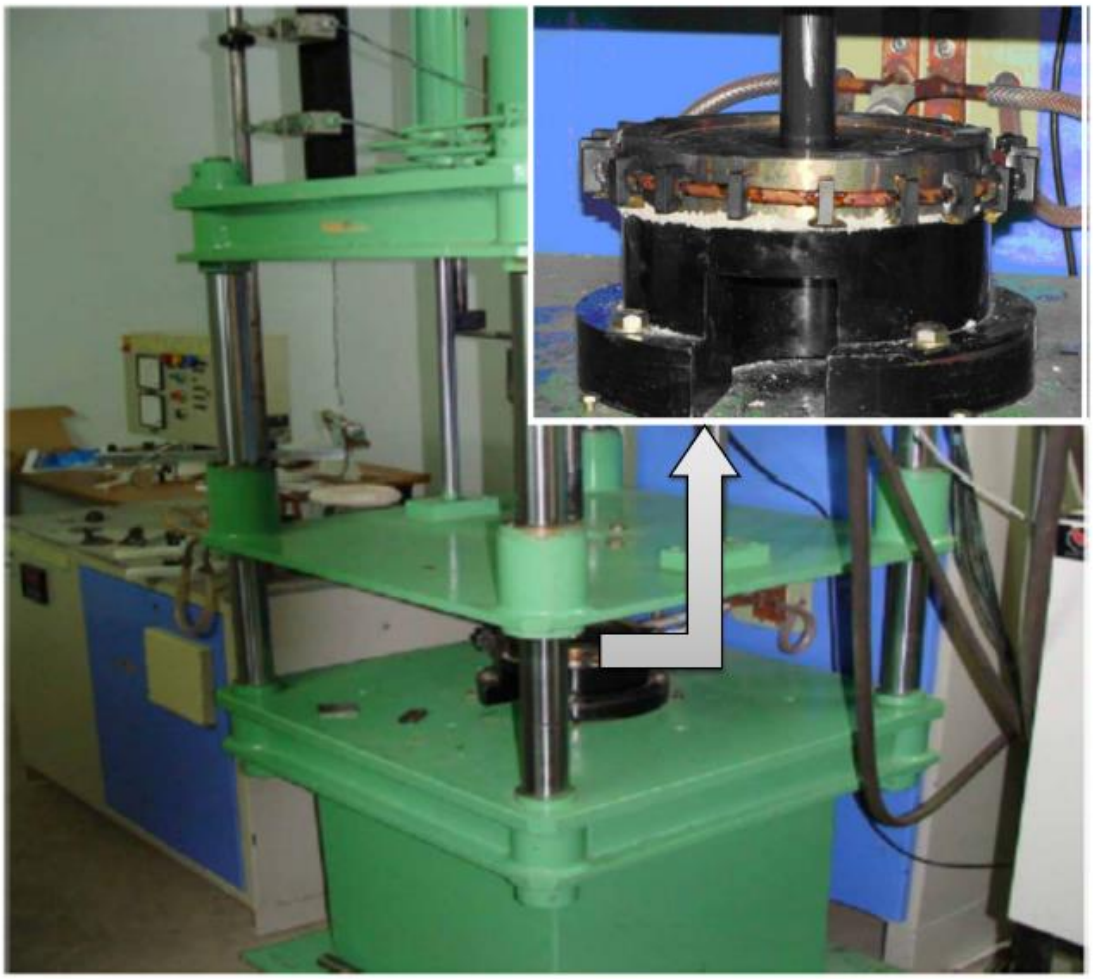

Figure 6.6: Experimental test rig for FLD

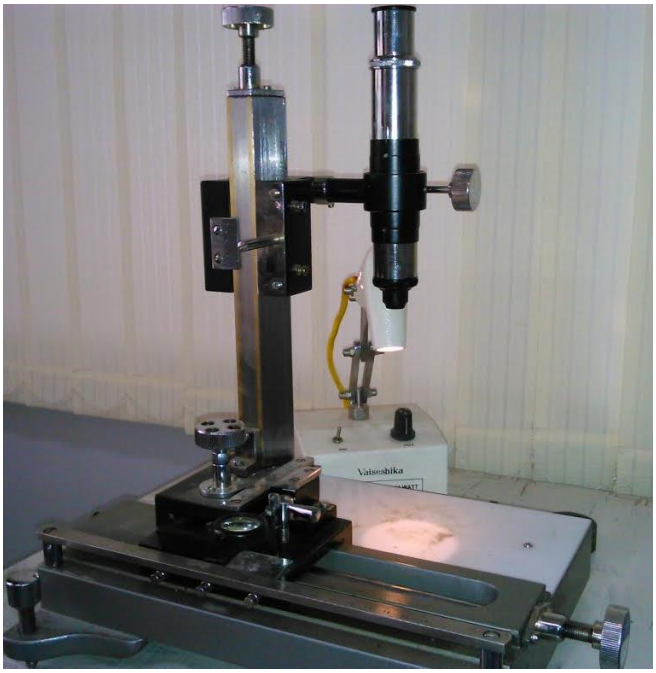

Figure 6.7: Traveling microscope for strain measurements

The experimental FLC curves were plotted after conducting hemispherical dome tests on different width specimens made of ASS 316 as shown in Figure 6.8. Experiments are conducted by placing the sheet specimens in such a way that circular etched marks prior to deformation are below the sheet. A series of blanks of different widths are deformed to hemispherical dome until fracture. After forming these domes, etching marks are stretched at outside of the dome and circles become ellipses of different sizes based on the deformation conditions as shown in Figure 6.9. Dimensions of etched grids are measured near to the fracture and major and minor strains are calculated. The axes of the ellipse formed on the domes are measured to find relative strain in two primary directions, known as the major and minor, which correspond to the major and minor axes of the ellipse.

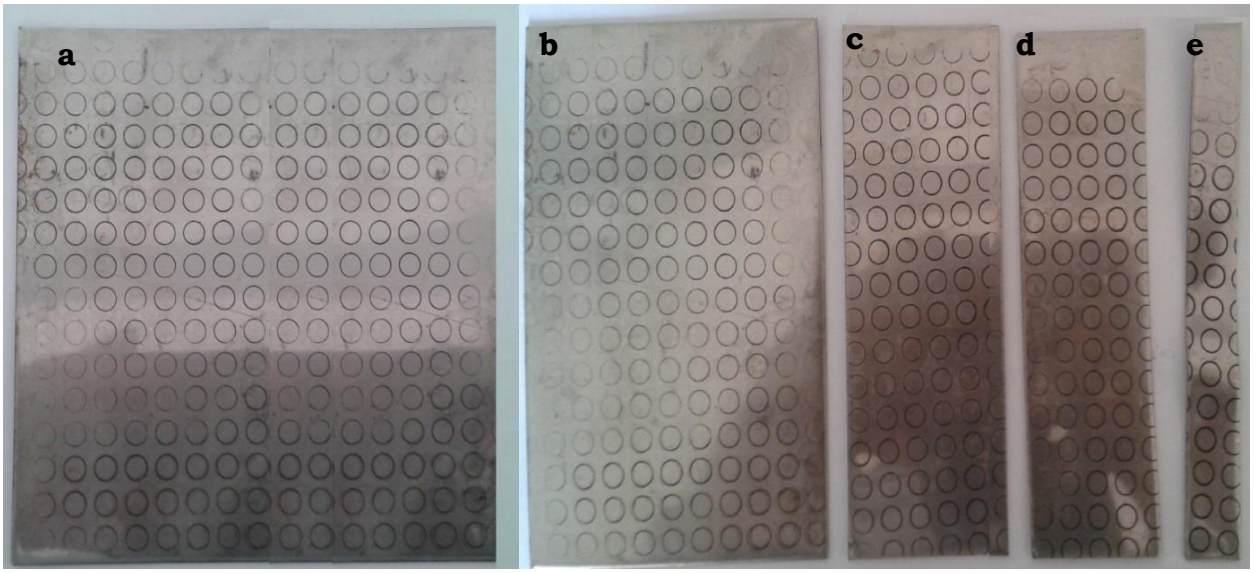

Figure 6.8: Different width specimens for dome test (a) 110x110 (b) 110x70 (c) 110X50 (d) 110x40 (e) 110X10 mm2

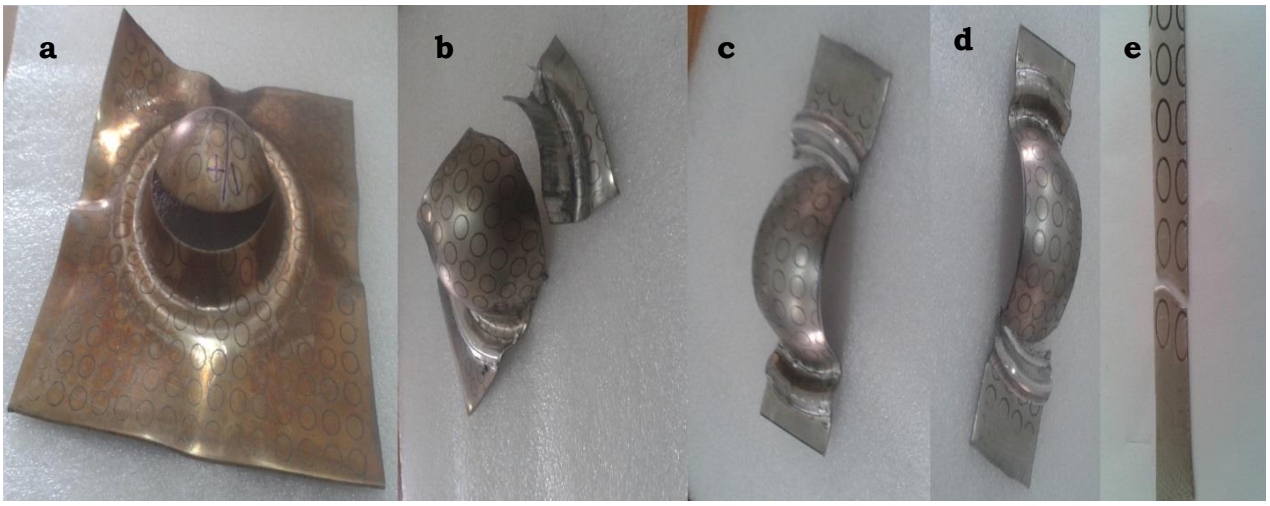

Figure 6.9: Fractured specimens after test (a) 110x110 (b) 110x70 (c) 110X50 (d) 110x40 (e) 110X10

These dome tests have been repeated to generate a range of strain conditions in the post deformation ellipses. Through repeated experimental measurements, the shape of the curve can be obtained experimentally. The FLC can be generated by mapping the shape of a failure criterion into the formability limit domain [108]. The FLD for ASS 316 is obtained at 300˚C and

shown in Figure 6.10. Here, in plotting FLC, the strains are measured very near to the fracture so that the curve is referred as the fracture curve.

As expected FLC intersects the major strain line approximately at 0.3, which is very close to the work hardening exponent of the material at 300^0C. So, the necking region extends between the major strains of 0.27 to 0.3. Although formability of the material at elevated temperature depends upon many factors, as discussed previously in this thesis; especially the onset of dynamic strain regime in ASS 316 when the fracture mode is primarily quasi brittle that is probably the reason for slight deviation in the intersection point from the work hardening exponent. As it can be seen in the diagram (Fig 6.10) that in the bi-axial strain region, slope of FLC is very small, in other words major strain is very predominant. ASS-316 is anisotropic material and this anisotropy increases further at 300^0C because the material is progressing to the DSA regime when compared to room temperature, yield strength of material at this temperature is less. So due to lower mean flow stress combining with anisotropy, there is unidirectional elongation in the material in this region.

The resultant diagram provides a tool for the determination as to whether a given forming process will result in failure. Such information is critical in the design of sheet metal forming processes. Friction is almost zero by using the lubrications with aluminum foils between sheets and tool. Using the highest value for several cross-section evaluations and 3 test samples for the same geometry at different locations to a strain pair (one point in the forming limit diagram) as forming limit is drawn. It is recognized that the nature of fracture and formability is intrinsically non-deterministic, since

little variations might be observed within a single experimental campaign [109].

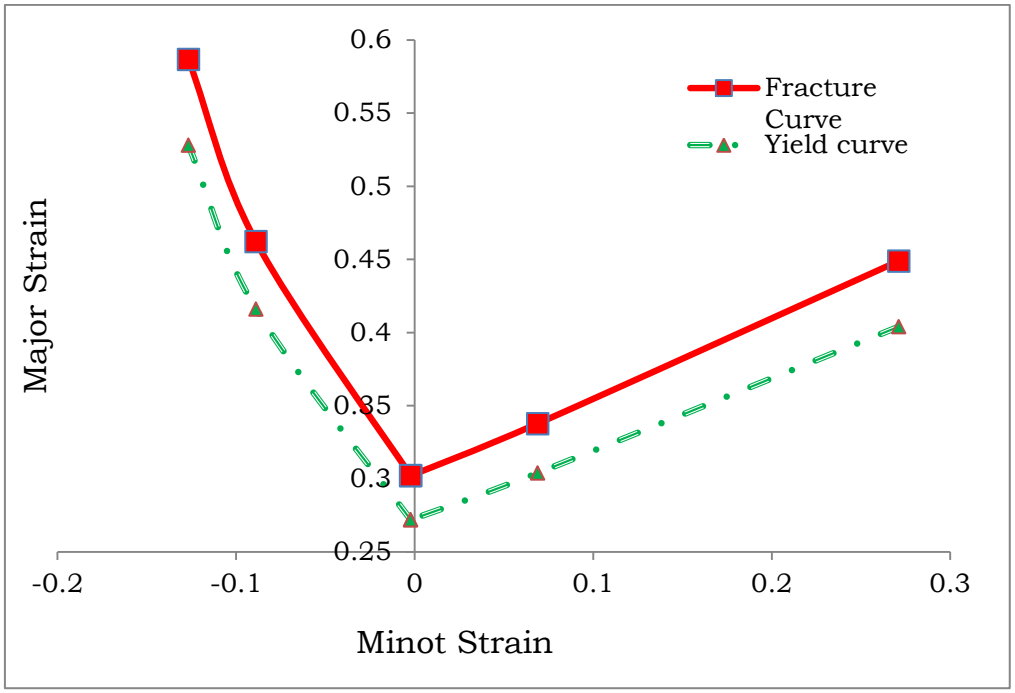

Figure 6.10: Experimental FLD for ASS 316 at 300˚C

6.3. Comparison of Experimental with Theoretical FLD

The experimental as well as the theoretical FLC's are plotted in Figure 6.11. The point on the FLC corresponding to the plain strain condition approximately has the value of *n*, the strain hardening coefficient. The plotted numerical FLC's intersect the major strain axis at almost the same point. This confirms that the value of *n*, considered for the numerical FLC is correct.

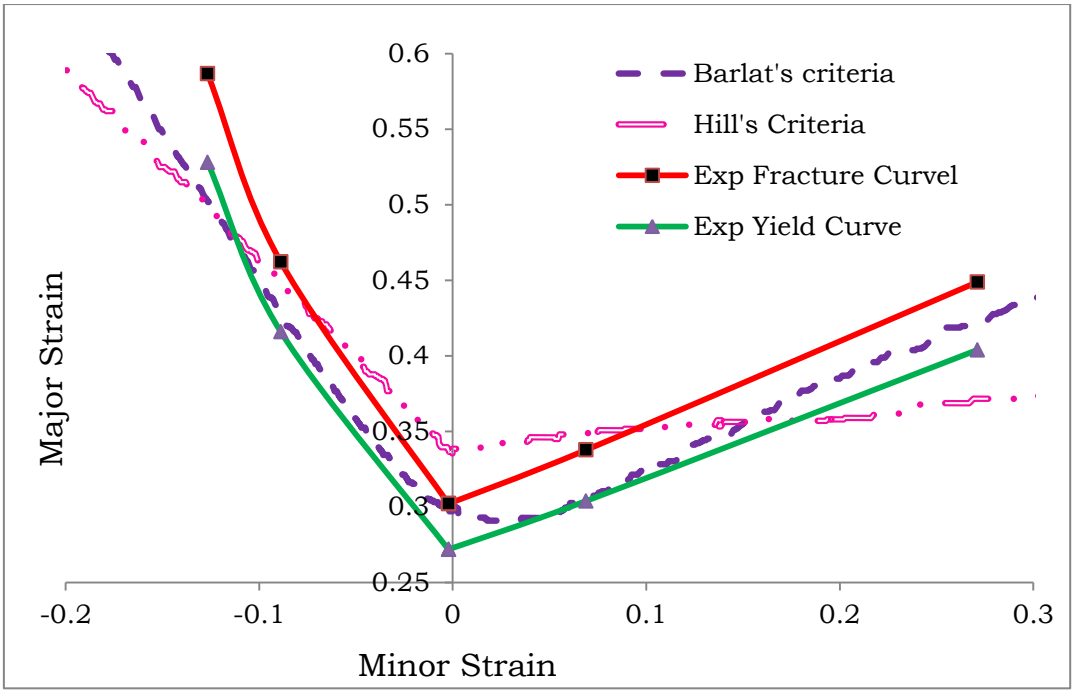

Figure 6.11: Experimental and Theoretical FLD

It can be observed from this figure that the Barlat's criterion is better able to follow the trend of the experimentally obtained FLC. It is because Barlat's criterion includes the anisotropy of the material and ASS-316 is highly anisotropic at 300^0C. This is especially true for the biaxial tension-tension region. Even in the tension-compression region of the FLC, the Barlat's criterion has a similar trend to that of the experimental FLC. However, FLC modeled using Barlat's criteria under-predicts the safe region in second quadrant. In fact, all the yield criteria under-predict the safe region in the FLC for negative minor strains.

To ascertain the accuracy of these numerical FLC plots, a correlation factor *R* is found by comparing the experimental data with the numerical prediction. Since it has already been ascertained that the numerical plots have sufficient accuracy, the correlation factors are found for the prediction. The *R* values obtained for the numerical FLC's along with the FLC plots. The

R value for the Barlat's prediction (0.887) is higher than the Hill's (0.713) as shown in Figure 6.12. This confirms that Barlat model is a better suited model among the considered yield functions in predicting theoretical FLD.

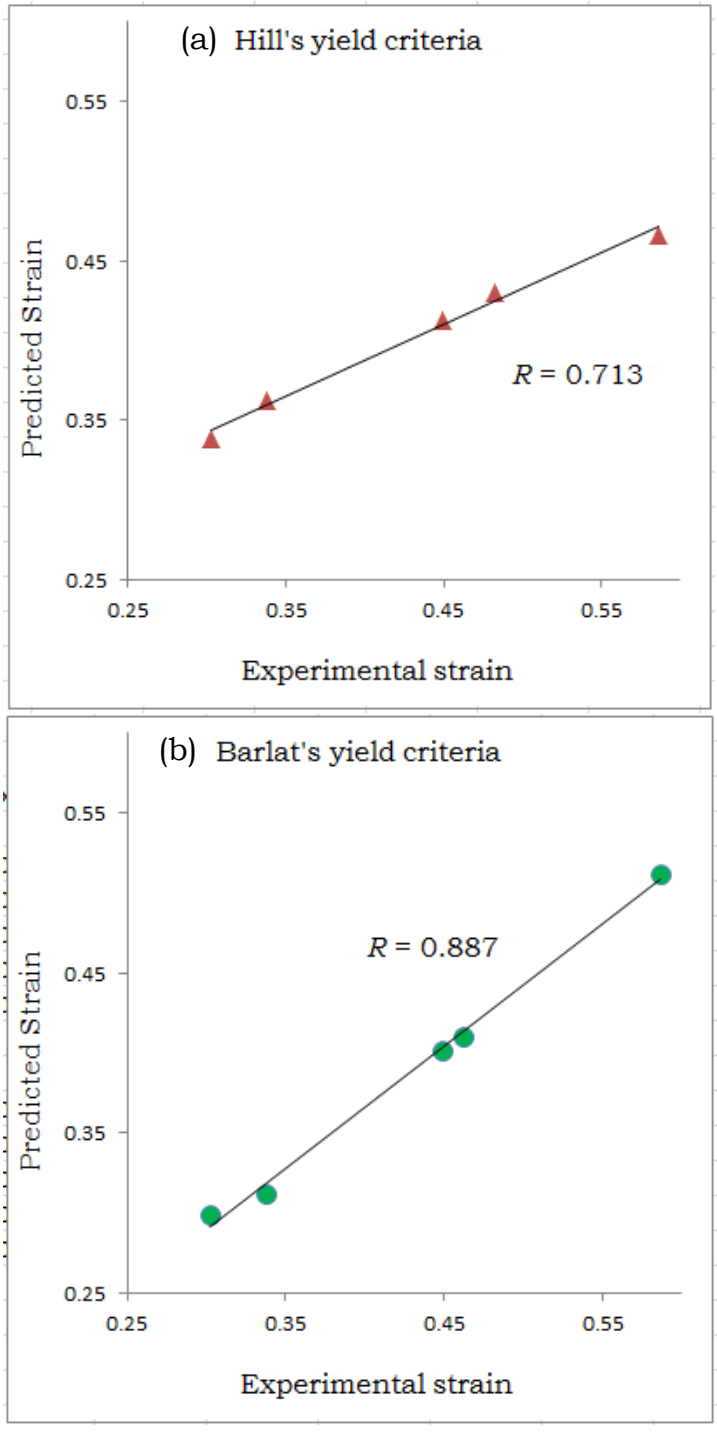

Figure 6.12: Comparison between experimental and predicted strains using (a) Hill's and (b) Barlat's yield criteria. .

CHAPTER 7:

Conclusions and Future Work

7.1 Salient Conclusions

This research focused on studying the formability behavior of ASS 316 at elevated temperatures. In this investigation, tensile tests have been conducted at elevated temperatures for evaluating the mechanical properties of the material. Deep drawing experiments have been carried out on the test setup for studying the formability of ASS 316. Numerical analyses have been done using FE models in LS-Dyna. FLD has been developed for ASS 316 at 300˚C by theoretical models, which has been validated with the experimental findings. These investigations bring out the following outcomes:

- From the tensile tests at various elevated temperatures and different strain rates, serrations have been observed in true stress vs. true strain curves in the temperature range of 400°C to 600°C and for strain rates lower than $1x10^{-2}$ /s. In addition, SRS index is found to have negative values in this regime. This confirms the presence of DSA region in ASS 316 in the temperature range of 400°C to 600°C and for strain rates lower than $1x10^{-2}$ /s.
- Fracture study of the tensile test specimens in non-DSA and DSA regions reveals that there is a significant difference in the fracture surface of the specimens in these two regions. In non-DSA region, the presence of dimples on the fracture surface shows a significant plastic deformation, indicating a ductile fracture. Whereas in DSA region, the fracture surface has cleavages in addition to dimples, which signifies a mixed-mode fracture representing less ductile nature of material in this region.

- In deep drawing experiments at elevated temperatures, LDR of ASS 316 sheets is found to have increased form 2.2 at room temperature to 2.33 at 150°C and to 2.47 at 300°C. However, with further increase in temperature, LDR is found to have decreased to 2.40 at 400°C. This decrease in drawability is caused by the DSA influence in this temperature region. Therefore, in warm forming of ASS 316, the drawability of the sheet increases with the increase in temperature up to 300°C, but beyond that it has a reverse effect on the drawability. Thus, within the practical experimental limits, LDR can be considered highest at 300°C with less thickness variations in deep drawing ASS 316 sheets.
- For FE simulation study of warm forming in ASS 316 using LS-Dyna, Barlat's yield criteria and Gosh's hardening law are used for accurate predictions of LDR and proper formation of cup. These simulation results show very good correlation with the experimental results. In addition, ANN model has been built to predict the thickness distribution of the drawn cup at any temperature to a very close accuracy.
- For FLD study, MK analysis has been used to theoretically construct the FLD at 300°C for warm forming behavior of ASS 316. These results have been validated by the experimentally developed FLD using hemispherical punch test. These FLDs can be used for designing warm manufacturing processes on ASS 316.

7.2 Limitations of the Present Work

A few limitations of the present research work are as follows:

- The formability study has been carried out only up to 400˚C due to the limitations in the experimental setup. In the deep drawing experimental setup, the punch, the die and the blank holder are made of Inconel material, which has stable properties only up to 400˚C. Therefore, this experimental setup can be used only up to a maximum temperature of 400˚C.
- Also, in FE simulation study using LS-Dyna, the available MTS model is capable of representing DSA phenomenon, but only for isotropic materials. At present, there is no suitable model available in LS-Dyna software to simulate DSA phenomenon in anisotropic materials such as ASS 316.

7.3 Scope of Future Work

The future research scope has the following directions:

- With appropriate experimental setup, the formability study can be extended to more than 400˚C temperature in search of higher LDR values.
- In LS-Dyna simulation modeling, anisotropic yield criteria can be incorporated in MTS model with proper customization for more

accurate predictions of forming behavior of anisotropic materials in DSA region.

- As ANN models are highly capable of providing very accurate predictions for mechanical properties and flow stresses, the software interoperability between ANN and LS-Dyna can help in achieving very highly accurate simulation results.
- For further increase in LDR, redrawing processes on ASS 316 sheets can also be investigated.

BIBLIOGRAPHY

[1] John G Lenard, "Metal forming science and practice", 1st ed. Elsevier Science, Kidlington, Oxford, UK, 2002, 9-18.

[2] Marciniak Z., Duncan J. L., Hu S. J., "Mechanics of Sheet Metal Forming", 2nd ed, Butterworth-Heinemann publ., London, 2002, 7-21.

[3] Stachowicz F., Trzepiecinski T, Pieja T., "Warm forming of stainless steel sheet", Archives civil and mech. Engg. 2010, 10: 86-94.

[4] Taylanaltan, Erman Tekkaya A., "Sheet Metal Forming: Fundamentals", ASM, US, 2012, 5-23.

[5] Gronostajski J., Matuszak A., Niechajowicz A., Zimniak Z., "The system for sheet metal forming design of complex parts", J. of Materials Processing Tech., 2004, 157: 502–507.

[6] Vukota Boljanovic, "Sheet Metal Forming Processes and Die Design", Industrial Press Inc., U, 2005, 70 – 77.

[7] George E Dieter, "Mechanical Metallurgy", 3rd ed, McGraw-Hill Higher Education, Student metric,1988, 666 – 673.

[8] Keeler S. P., "Plastic instability and fracture in sheet stretched over rigid punches", ASM Trans. 1964, 56: 25-48.

[9] Banabic D, Dannenmann E., "Prediction of the influence of yield locus on the limit strains in sheet metals", J. of Materials Processing Tech., 2001, 109: 9–12.

[10] Marciniak Z., Kuczinski K., Pokora T., "Influence of the Plastic Properties of the Material on the Forming Limit Diagram for Sheet Metal Tension", Int. J. Mech. Sci., 1973, 15: 789-805.

[11] Geiger M., Merklein M., “Determination of Forming Limit Diagrams – A New Analysis Method for Characterization of Materials Formability”, Annals of the CIRP, 2003, 52: 1-6.

[12] Keeler S. P., "Determination of Forming Limits in Automotive Stampings." SAE Mid-Year Meeting, Chicago, 1995.

[13] Dorel Banabic, “Sheet Metal Forming Processes Constitutive Modelling and Numerical Simulation”, Springer- Verlag Berlin Heidelberg, 2010.

[14] Xi Wang, Jian Cao., “On the prediction of side wall wrinkling in sheet metal forming processes”, Int J of Mech Sci., 2000, 42: 2369-2394.

[15] Aderibigbe. D. A, Oluwole. O. O, Olorunniwo. O. E, Atanda, P.O and Ogundare. O, “Earing Characteristics of Cold-Rolled and Temper – Annealed Al 1200”, J of Applied Sci, 2006, 6: 3103-3109.

[16] Gantar G., Kuzman K., Filipic B., “Increasing the stability of deep drawing process by simulation based optimization”, J. of Materials Processing Tech., 2005, 164: 1343–1350.

[17] Karbasian, H., Tekkaya A. E.,“A review on hot stamping”, J. of Materials Processing Tech., 2010, 210: 2103-2118.

[18] Pardo A., Merino M.C., Coy A.E., Viejo F., Arrabal R., Matykina E., “Pitting corrosion behavior of austenitic stainless steels combining effects of Mn and Mo additions”, Corrosion Sci., 2008, 50:1796-1806.

[19] Barat P., Raj B., Bhatracharya D.K., “A standardized procedure for eddy-current testing of stainless steel, thin-walled nuclear fuel element cladding tubes”, NDT International, 1982, 15: 251-255.

[20] Benallala A., Berstadb T., Borvikb T., Clausenb A.H and. Hopperstadb O.S. “Dynamic strain aging and related instabilities: experimental,

theoretical and numerical aspects". European J of Mechanics - A/Solids, 2006, 25, 397-424.

[21] Ling C.P., McCormick P.G., Estrin Y., "A technique to probe dynamic strain aging", Advances in Engg. Plast and its Appl., 1993, 455-460.

[22] Tebbe P. A., Kridli G. T., "Warm Forming of Aluminum Alloys: An Overview and Future Directions", Int. J. Mater. Prod. Tech., 2004, 21:24–40.

[23] Frechard S., Redjaimia A., Lach E., Lichtenberger A., "Mechanical behaviour of nitrogen alloyed austenitic stainless steel hardened by warm rolling", Materials Science and Engineering, 2006, A415: 219–224.

[24] Lange K. "Handbook of metal forming", McGraw-Hill Book Co., NY, 1985.

[25] Takuda H., Mori K., Masachika W., Watanabe Y. "Finite element analysis of the formability of an austenitic stainless steel sheet in warm deep drawing", J of Materials Processing Tech., 2003, 143: 242–248.

[26] Smallman, Bishop, "Metals and Materials: science, process, applications", Butterworth - Heinemann, 1995.

[27] Shehata, F., Painter, M. J., and Pearce, R., "Warm Forming of Aluminum/Magnesium Alloy Sheet", J. Mech. Work. Tech., 1978, 2: 279–291.

[28] Wilson, D. V., "Aluminum versus Steel in the Family Car-The Formability Factor", J. Mech. Work. Technol., 1988, 16, 257–277.

[29] Schmoeckel D, Metal Forming (Warm): Comparison with Hot and Cold Forming, Encyclopedia of Materials: Science and Technology, 2001, 5437–5438.

[30] Li D., Ghosh A., “Tensile Deformation Behavior of Aluminum Alloys at Warm Forming Temperatures”, Mater. Sci. Engg.- A, 2003, 352: 279–286.

[31] Van Den Boogaard A. H., Huetink, J. “Simulation of Aluminum Sheet Forming at Elevated Temperatures”, Comput. Methods Appl. Mech. Eng., 2006, 195: 6691–6709.

[32] Mckinley J., Abedrabbo N., Worswick M. J., Kozards, M., “Effect of Independent Die and Punch Temperature Control on the Formability of 3003 Aluminum Alloy in Warm Deep Drawing”, Proceedings of the 7th International Conference, Numisheet, Interlaken, Switzerland, 2008.

[33] Tyng Bin Huanga, Yung-An Tsaia, Fuh-Kuo Chenb, “Finite element analysis and formability of non-isothermal deep drawing of AZ31B sheets”, J of Materials Processing Tech., 2006, 177: 142–145.

[34] Kim H. S., KocM., Ni J., Ghosh, A., “Finite Element Modeling and Analysis of Warm Forming of Aluminum Alloys-Validation Through Comparisons With Experiments and Determination of a Failure Criterion,” ASMEJ. Manuf. Sci. Eng., 2006, 128: 613–621.

[35] Abedrabbo N., Pourboghrat F., Carsley J., “Forming of AA5182-O and AA5754-O at Elevated Temperatures Using Coupled Thermo-Mechanical Finite Element Models”, Int. J. Plast., 2007, 23, 841–875.

[36] Tugcu, P., Wu, P. D., and Neale, K. W., On the Predictive Capabilities of Anisotropic Yield Criteria for Metals Undergoing Shearing Deformations,” Int. J. Plast., 2002, 18: 1219–1236.

[37] Paquet D., Dondeti P., and Gosh S., “Dual-Stage Nested Homogenization for Rate-Dependent Anisotropic Elasto-Plasticity Model of Dendritic Cast Aluminum Alloys”, Int. J. Plast., 2011, 27: 1677–1701.

[38] Desmorat R., and Marukk R., “Non-Quadratic Kelvin Modes Based Plasticity for Anisotropic Materials”, Int. J. Plast., 2011, 27: 328–351.

[39] Thomson W. K., Lord Kelvin, “Elements of a Mathematical Theory of Elasticity”, Philos. Trans. R. Soc., London, 1856, 166: 481–498.

[40] Segurado, J., Lebensohn, R. A., Lorca, J., Tome, C. N., “Multi scale Modeling of Plasticity Based on Embedding the Viscoplastic Self-Consistent Formulation in Implicit Finite Elements”, Int. J. Plast., 2012, 28: 124–140.

[41] Fourmeau M., Borvki T., BenallalA., Lademo O. G., Hopperstad, O. S., “On the Plastic Anisotropy of an Aluminum Alloy and Its Influence on Constrained Multi axial Flow”, Int. J. Plast., 2011, 27: 2005–2025.

[42] Barlat F., AretzH., Yoon J. W., Karabin M. E., Brem J. C., Dick, R. E., “Linear Transformation-Based Anisotropic Yield Functions”, Int. J. Plast., 2005, 21: 1009–1039.

[43] Yoon J. W., Dick R. E., Barlat F., “A New Analytical Theory for Earing Generated From Anisotropic Plasticity”, Int. J. Plast., 2011, 27: 1165–1184.

[44] Soarea M.A. and Curtin W.A., “Single-mechanism rate theory for dynamic strain aging in FCC metal”, Acta Materialia, 2008, 56: 4091-4101.

[45] Sinisa Dj. Mesarovic, “Dynamic strain aging and plastic instabilities”, J of the Mechanics and Physics of Solids, 1995, 43: 671–700.

[46] Butler J.F., "Lüders front propagation in low carbon steels", J of the Mechanics and Physics of Solids, 1962, 10: 313-318.

[47] Cottrell, A.H. & Bilby, B.A. "Dislocation theory of yielding and strain aging of Iron", Proceedings of Physical Society A. 1949, 62: 49-62.

[48] Egidio Rizzia, Peter Hähnerb, "On the Portevin–Le Chatelier effect theoretical modeling and numerical results", Int. J. of Plast, 2004, 20: 121-165.

[49] McCormick, P.G. "A model for the Portevin LeChatelier effect in substitutional alloys". Acta Metallurgica.1972, 20: 351 – 354.

[50] Friedel J. "Dislocations". Oxford, United Kingdom: Pergamon Press, 1964, 491-497.

[51] Penning, P. "Mathematics of the Portevin LeChatelier effect". Acta Metallurgica.1972, 20: 1169-1175.

[52] A. Van Den Beukel, "On the mechanism of serrated yielding and dynamic strain aging", Acta Metallurgica, 1980, 28: 965-969.

[53] McCormick, P.G. "Theory of flow localization due to dynamic strain aging", Acta Metallurgica, 1988, 36: 3061-3067.

[54] Rose, K.S.B., Glover S.G. "A study of strain aging in austenite". Acta Metallurgica, 1966, 14: 1505-1516.

[55] S. Venugopal, S.L. Mannan, Y.V.R.K. Prasad, "Instability map for cold and warm working of as-cast 304 stainless steel", J of Materials Processing Tech., 1997, 65: 107-115.

[56] T.S Byun, N Hashimoto, K Farrell, "Temperature dependence of strain hardening and plastic instability behaviors in austenitic stainless steels", Acta Materialia, 2004, 52: 3889-3899.

[57] L.H. de Almeida, P.R.O. Emygdio, I. Le May, “Activation energy calculation and dynamic strain aging in austenitic stainless steel”, Scripta Metallurgica et Materialia, 1994,31: 505-510.

[58] L. Shi, D.O. Northwood, “The mechanical behavior of an AISI type 310 stainless steel”, Acta Metallurgica et Materialia, 1995: 43,453-460.

[59] Dae Whan, Kim, Woo Gon, Kim, Woo-Seog Ryu, “Role of dynamic strain aging on low cycle fatigue and crack propagation of type 316L(N) stainless steel”, Int. J. of Fatigue, 2003, 25: 1203-1207.

[60] B.P. Kashyap, K. Tangri, “Hall-Petch relationship and substructural evolution in boron containing type 316L stainless steel”, Acta Materialia, 1997, 45: 2383-2395.

[61] J.G. Morris, “Dynamic strain aging in aluminum alloys”, Materials Science and Engineering, 1974, 13: 101-108.

[62] M. Nani Babu, G. Sasikala, B. Shashank Dutt, S. Venugopal, S.K. Albert, A.K. Bhaduri, T. Jayakumar, “Investigation on influence of dynamic strain ageing on fatigue crack growth behaviour of modified 9Cr–1Mo steel”, Int J of Fatigue, 2012, 43: 242–245

[63] Aritra Sarkara, A. Nageshaa, P. Parameswaranb, R. Sandhyaa, M.D. Mathew, “ Influence of dynamic strain aging on the deformation behavior during ratcheting of a 316LN stainless steel” Materials Science and Engineering A, 2013, 564: 359–368.

[64] M. Srinivasa, S.V. Kamata, P. Rama Rao, “Influence of dynamic strain ageing on mixed mode I/III fracture toughness of Armco iron” Materials Science and Engineering A, 2007, 443:132–141.

[65] H. S. Khatak, Baldev Raj, “Corrosion of Austenitic Stainless Steels: Mechanism, Mitigation”, Wood head Publishing Ltd, 2002.

[66] P. Marshall, “Austenitic Stainless Steels: Microstructure and Mechanical Properties”, Elsevier Applied Science Publishers Ltd, 1984.

[67] Volker B. E. Thomson, “Modern Spectrochemical Analysis of Metals: An Introduction for Users of Arc / spark instrumentation”, ASM International, 1996.

[68] Hedworth, J., Stowell, M. J., “The measurement of strain-rate sensitivity in superplastic alloys” J of Material Science, 1971, 6: 1061–1069.

[69] McCormick PG, “Strain rate sensitivity prior to the onset of serrated yielding in a pressurized low carbon steel”, Scripta Metal, 1978: 197-200.

[70] McCormick PG, “Theory of flow localization due to dynamic strain aging”, Acta Metall, 1988, 36: 3061–3067.

[71] R.A. Mulford, U.F. Kocks, “New observations on the mechanisms of dynamic strain aging and of jerky flow”, Acta Metall, 1979 27: 1125 – 1134.

[72] L. J. Cuddy, W.C. Leslie, “Some aspects of serrated yielding in substitutional solid solutions of iron”, Acta Metall, 1972, 20: 1157-1167.

[73] Derek Hull, “Fractography: Observing, Measuring and Interpreting Fracture Surface Topography”, Cambridge University Press, 1999.

[74] R M Lynden-Bell, “A simulation study of induced disorder, failure and fracture of perfect metal crystals under uniaxial tension”, J. Phys. Condens Matter, 1995, 7: 4603.

[75] Callister, W. D. “Materials Science and Engineering: An Introduction”, 4th Edition, John Wiley & Sons, Inc, New York, 1997.

[76] Hosford, W. F., Caddell, R. M. “Metal Forming: Mechanics and Metallurgy”, 2nd Edition, PTR Prentice-Hall, Englewood Cliffs, New Jersey, 1993.

[77] Banabic D., Bunge H.J, Pöhlandt, K., Tekkaya A. E., “Formability of Metallic Materials”, Springer-Verlag: Berlin/Heidelberg/New York/Tokyo, 2000.

[78] Jump up Lankford, W. T., Snyder, S. C., Bausher, J. A., “New criteria for predicting the press performance of deep drawing sheets”. Trans. ASM, 1950, 42: 1197–1205.

[79] Weilong, H., Wang, Z.R., “Anisotropic Characteristics of Material and basic Selecting Rules with Different Sheet Metal Forming Processes”, J of Materials Processing Tech, 2002, 127: 374-381.

[80] Marciniak, Z., Duncan J.L., HuS. J., “Mechanics of Sheet Metal Forming”, 2nd ed, Butterworth-Heinemann, Oxford, 2002.

[81] A. Erman Tekkaya, “Sheet Metal Forming: Fundamentals”, Taylan Altan, 2012, 105-125.

[82] D. K. Leu, “Prediction of maximum drawing load in the cup-drawing process of sheet metals”, J of Materials Processing Tech. 1997, 72:256–61.

[83] Serkan Toros, Fahrettin Ozturk, Ilyas Kacar, “Review of warm forming of aluminum–magnesium alloys”. J of Mater Process Tech, 2008, 207: 1-12.

[84] LS-Dyna user's manual, Livermore software technology corporation, California, 2007, Vol-1.

[85] Hill R,"A theory of the yielding and plastic flow of anisotropic metals".Proc R Soc Lond 1948, 193: 281–297.

[86] Hill R, "Theoretical plasticity of textured aggregates", Math Proc Camb Philos Soc, 1979, 85: 179–191.

[87] Ferron G, Makkouk R, Morreale J, "A parametric description of orthotropic plasticity in metal sheets", Int J Plast, 1994: 10, 431–449.

[88] Barlat F, Chung K, Richmond O, "Strain rate potential for metals and its application to minimum plastic work path calculations", Int J Plast, 1993, 9: 51–63.

[89] Barlat F, Aretz H, Yoon JW, Karabin ME, Brem JC, Dick RE, "Linear transformation-based anisotropic yield functions". Int J Plast, 2005, 21: 1009–1039.

[90] Barlat F, Lian J, "Plastic behavior and stretchability of sheet metals, part-I: a yield function for orthotropic sheet under plane stress conditions". Int J Plast, 1989, 5: 51–66.

[91] Hosford WF,"A generalized isotropic yield function". Trans ASME J Appl Mech, 1972, 39: 607–609.

[92] Barlat F, Lege DJ, Brem JC, "A six-component yield function for anisotropic materials".Int J Plast, 1991, 7: 693–712.

[93] Karafillis AP, Boyce MC, "A general anisotropic yield criterion using bounds and a transformation weighting tensor". J Mech Phys Solids, 1993, 41: 1859–1886.

[94] Barlat F, Brem J C, Yoon J W, Chung K, Dick R E, Lege D J, Pourboghrat F, Choi SH, Chu E, “Plane stress yield function for aluminum alloy sheets-part 1: theory”,Int J Plast, 2003, 19: 1297–1319.

[95] Yoon JW, Hong SH, “Modeling of aluminum alloy sheets based on new anisotropic yield functions”. J of Materials Processing Tech, 2006, 177: 134–137.

[96] Yoon JW, Barlat F, Dick RE, Karabin ME, “Prediction of six or eight ears in a drawn cup based on a new anisotropic yield function”,Int J Plast, 2006, 22: 174–193.

[97] Barlat, DL Lege, J. C. Bream, “A six component yield function for anisotropic materials”, Int J Of plasticity, 1991, 7: 693-712.

[98] Follansbee P. S, Kocks U F, “A constitutive description of the deformation of copper based on the use of the mechanical threshold stress as an internal state variable”, Acta Metall., 1988, 36: 81-93.

[99] Goto DM, Bingert JF, Chen SR, Gray GT, Garrett RK, “The mechanical threshold stress constitutive-strength model description of HY- 100 steel”, Metallurgical and Materials Transactions A, 2000, 31A: 1985-1996.

[100] Singh Swadesh Kumar, D. Ravi Kumar, “Effect of process parameters on product surface finish and thickness variation in hydro-mechanical deep drawing” J of Materials Processing Tech., 2008, 204: 169–78.

[101] Swadesh Kumar Singh, K. Mahesh, Apurv Kumar, M. Swathi, “Understanding formability of extra-deep drawing steel at elevated temperature using finite element simulation”, Materials & Design, 2010, 31: 4478-4484.

[102] Mitsutoshi Kuroda, Viggo Tvergaard, “Forming limit diagrams for anisotropic metal sheets with different yield criteria” Int J of solids and structures, 2000, 37: 5037-5059.

[103] Raed Z. Hasan, Brad L. Kinsey, Igor Tsukrov , “Effect of Element Types on Failure Prediction Using a Stress-Based Forming Limit Curve”, J of Manufacturing Science and Engineering, 2011, 133: 0610021-8.

[104] T. Pepelnjak, K. Kuzman, “Numerical determination of the forming limit diagrams” J of Achievements in Materials and Manufacturing Engineering, 2007, 20: 375-378.

[105] R. Hill, “A Theory of the Yielding and Plastic Flow of Anisotropic Metals” Proc. R. Soc. Lond, 1948, 193: 281-297.

[106] Xiaoqiang Li, Nan Song, Guiqiang Guo, Zhonggang Sun, “Prediction of forming limit curve (FLC) for Al–Li alloy 2198-T3 sheet using different yield functions” Chinese J of Aeronautics, 2013, 26:1317-1323.

[107] Siguang Xu, Klaus J., Weinmann, “Effect of deformation-dependent material parameters on forming limits of thin sheets”, Intl J of Mech. Sci., 2000, 42: 677-692.

[108] Pearce R. “Sheet Metal Forming”, Adam Hilger, 1991, ISBN 0-7503-0101-5.

[109] Strano M., Colosimo, B.M., "Logistic regression analysis for experimental determination of forming limit diagrams". International Journal of Machine Tools and Manufacture, 2006, 46: 673–682.

LIST OF PUBLICATIONS AND PRESENTATIONS

International Journals

Accepted:

1. Syed Mujahed Hussaini, Swadesh Kumar Singh, Amit Kumar Gupta, “Experimental and Numerical Investigation of Formability for Austenitic Stainless Steel 316 at Elevated Temperatures” Journal of Materials Research and Technology, 2014, 3: 17-27.
2. Syed Mujahed Hussaini, Swadesh Kumar Singh, Amit Kumar Gupta, “Formability of Austenitic Stainless Steel 316 sheet in Dynamic Strain Aging Regime”, Acta Metallurgica Slovaca, 2014, 20: 71-81.
3. Syed Mujahed Hussaini, Swadesh Kumar Singh, Amit Kumar Gupta, “Formability and fracture studies of austenitic stainless steel 316 at different temperatures”, Journal of King Saud University – Engineering Sciences, 2014, 25: 184-190.
4. SM Hussaini, SK. Singh, and AK Gupta. "Experimental investigation of Dynamic strain aging regime in Austenitic Stainless Steel 316", International Journal of Engineering Research & Technology, 2013, 1691-1694.

Under Review:

5. Syed Mujahed Hussaini, Swadesh Kumar Singh, Amit Kumar Gupta, “Finite Element Investigation of Formability for Austenitic Stainless Steel at Elevated Temperatures and Experimental Validation”, International Journal of Advanced Manufacturing Technology, (under review)

In Preparation:

6. Syed Mujahed Hussaini, Geetha Krishna, Amit Kumar Gupta, Swadesh Kumar Singh, “Development of Forming Limit Diagram for ASS 316 at elevated temperatures” (in preparation)

International conferences

Presented and Published

1. Hussaini SM, Gupta AK, Singh SK "Determination of the Limiting Drawing Ratio in Deep Drawing Process at Different Temperatures for Austenitic Stainless steel" 4th International & 25th AIMTDR – 2012, JU-Kolkata, 14-16 Dec-2012.
2. SM Hussaini, AK Gupta "Mechanical Threshold Stress model for prediction of Flow stress" ICMPC – 2012, GRIT – Hyderabad, 08– 10 March 2012.
3. SM Hussaini, Arun K, AK Gupta "Study of Stresses and Deformation during Deep Drawing Process" ICAMMP-2011, IIT –Kharagpur, 9-11 December 2011.
4. SM Hussaini SK Singh, M L Kranti Raj, AK Gupta "Characterization and formability of aluminum IS 737 40800 grade material at elevated temperature", International Conference on Production and Industrial Engineering CPIE-2010, 03-05 December, 2010.
5. Hussaini SM, Gupta AK, Singh SK "Investigation of Material Model for Simulations of Deep Drawing in Dynamic Strain Aging Region" 3rd International Conference on Materials Processing and Characterisation (ICMPC 2014), GRIT, Hyderabad, 08-09 March-2014.

Accepted

6. Syed Mujahed Hussaini, Gupta AK, Singh SK "Experimental investigation of Blank holding force and Punch speed effect on deep drawing of austenitic stainless steel" 15th International Conference Metal Forming 2014, University of Plermo, Palermo, Italy, 21 - 24 September, 2014

BRIEF BIOGRAPHY OF THE SUPERVISOR

Name of the supervisor	**Dr. Amit Kumar Gupta**
Qualifications	**PhD**
Designation and Address	**Associate Professor ,** **Mech. Engg. Dept.** **BITS-Pilani, Hyderabad Campus**
Experience (years)	**8**
Number of Publications Journal/Book/Other	**35**
No. of Ph.D. students supervised	**0**

BRIEF BIOGRAPHY OF THE CANDIDATE

Name of the candidate	**Syed Mujahed Hussaini**
ID No	**2009PHXF451P**
Designation and Address	**Lecturer,** **Mech. Engg. Dept.** **BITS-Pilani, Hyderabad Campus**
Number of Publications Journal/Book/Other	**5**